# Experimental and Numerical Investigation of Performance and Emissions in Compression Ignition Engines with Alternative Fuels


**Shahid Imran**

School of Engineering and Material Sciences

Queen Mary University of London

**Supervisor: Prof. Theodosios Korakianitis**

(a.k.a. Theodosios Alexander)

A thesis submitted in conformity with the requirements

for the degree of Doctor of Philosophy

University of London

**DISSERTATION APPROVAL**

Experimental and Numerical Investigation of Performance and Emissions in Compression Ignition Engines with Alternative Fuels

By

Shahid Imran

A Dissertation Submitted in Partial

Fulfillment of the Requirements

for the Degree of

Doctor of Philosophy

in the field of Mechanical Engineering

Approved by:

Prof. Hua Zhao

Brunel University London, United Kingdom

Prof. Nicos Ladommatos

University College London, United Kingdom

## ABSTRACT

The experimental investigation in this work concerns the compression-ignition (CI) engine combustion process both in normal operation and dual-fuel operation. There is a bulk of literature reporting thermal efficiencies, brake specific fuel consumption (BSFC) and emissions under single and dual fueling conditions in CI engines. Most of the studies lack the full implications of changing load (power output) and speed on these performance indicators. The studies are either restricted to various loads/powers at one engine speed (neglecting the effect of engine speed) or one or two load/power conditions at various speeds (neglecting load variations). There is a scarcity of full engine maps in the open literature (these are the full contours of thermal efficiency or BSFC plotted throughout the power versus speed range of the engine, or the torque versus speed range of the engine). This thesis provides performance and emissions maps for a CI engine using two different fuels (diesel and rapeseed methyl ester used as single fuels) and two gaseous fuels (natural gas and hydrogen) used with two different pilot fuels (diesel and rapeseed methyl ester ) under what is termed dual fueling mode. A novel approach is used to present the performance and emissions over the entire engines operational range. The results are presented as iso-contours of thermal efficiency, volumetric efficiency and brake specific $NO_X$, specific HC and specific $CO_2$ on a power-speed graph throughout the operating range of the engine.

Many studies conclude that the emissions, particularly $NO_X$ during dual fueling are expected to form in the spatial region around the pilot spray. This region is expected to be subjected to high localised temperatures as the equivalence ratio is close to stoichiometric, thus maximising heat release from combustion. The effect of changing the pilot fuel quantity on performance and emissions is rarely reported. This study addresses this scarcity in the literature and investigates the effect of changing the pilot fuel quantity and type on various combustion and emission parameters. Diesel and rapeseed methyl ester (RME) have been used as pilot fuels for both the natural gas as well as hydrogen and three different pilot fuel

settings have been employed for each of the gaseous fuels. The effect of using a different pilot fuel quantity to achieve the same brake mean effective pressure (BMEP) for the two gaseous fuels has been analysed and compared.

This thesis also includes a chapter on the computational modeling of the engine esmissions. This study uses combinations of different spray and combustion models to predict in-cylinder pressure, rate of heat release and emissions. The approach employs two combustion models: Unsteady Flamelet Model (UFM) with PDF method and Finite Rate Chemistry (FRC) with stiff chemistry solver implemented through In-Situ Adaptive Tabulation (ISAT) algorithm. Two spray models used include WAVE and Kelvin Helmohltz Rayleigh Taylor (KHRT) spray models. The UFM coupled with KHRT spray model has been used to predict $NO_X$, CO and $CO_2$ emissions. The model captures the emissions trends well. In-cylinder contours of $O_2$, NO and mass average temperature have also been presented. A chemical mechanism of n-heptane with 29 species and 52 reactions has been used.

# Dedications

I would like to dedicate this thesis to my loving and caring wife; Mrs. Uzma Imran

# Acknowledgements

First and foremost I thank my parents; Mr. Muhammad Rafique and Mrs. Bhag Bhari for their constant love, efforts and guidance. I also thank my wife; Mrs. Uzma Imran for her continuous support, care and love and my son; Mr.Ali Imran for being a source of joy and happiness. I thank my brother Adv. Abu Bakr for looking after my family and interests in my absence. I thank my supervisors, Professor Theodosios Alexander and Professor Roy Crookes for their instruction and understanding during this project. I thank the many people in the QMUL support staff; in particular Mr. Mick Etheridge, Mr. Vince Ford, Ms. Jun Ma, and Mr. Chris Straw for their expertise, professionalism and patience. Finally, I thank all my friends and colleagues I have made over the course of this work for the useful discussions. Special thanks go to Mr. Amin Rezaienia for sharing some hard times during last four years and Mr. Dave Emberson for his encouragement and helping me to correct the thesis as well as my work submitted for publications.

## NOMENCLATURE

Latin

| | |
|---|---|
| $A$ | pre-exponential |
| $D$ | diffusion coefficient |
| $E$ | activation energy |
| $\mathbf{J}$ | heat flux vector |
| $k$ | turbulence kinetic energy |
| $k_b$,$k_f$ | reaction coefficients |
| $K_c$ | equilibrium constant |
| $K_p$ | equilibrium constant |
| $R$ | universal gas constant |
| $S$ | entropy |
| $T$ | temperature (K) |
| $t$ | time |
| $W$ | molecular weight |
| $Y$ | mass fraction |

Greek

| | |
|---|---|
| $\mu$ | first viscosity coefficient |
| $\nabla$ | difference operator |
| $\rho$ | density |
| $\Sigma$ | viscous stress tensor |
| $\phi$ | equivalence ratio |

$\chi$ chemical species

$\gamma$ specific heat ratio

Abbreviations

ATDC after top dead centre

BP British Petroleum

BSFC brake specific fuel consumption

CA crank angle

CFD computational fluid dynamics

CI compression ignition

CO carbon mono oxide

$CO_2$ carbon dioxide

CR compression ratio

DICI direct injection compression ignition

DME dimethyl ether

FRC finite rate chemistry

HC hydro carbons

IC internal combustion

ISAT in-situ adaptive tabulation

KHRT Kelvin Helmohltz Rayleigh Taylor

$NO_X$ oxides of nitrogen

ODE ordinary differential equation

OECD Organisation for Economic Co-operation and Development

| | |
|---|---|
| PDF | probability density function |
| RME | rape methyl ester |
| SFC | specific fuel consumption |
| SI | spark ignition |
| UFM | unsteady flamelet model |

## TABLE OF CONTENTS

## LIST OF TABLES

## LIST OF FIGURES

# CHAPTER 1

# INTRODUCTION

## 1.1 BACKGROUND

The reciprocating internal combustion engines is the most common form of engine or prime prime mover. These are open circuit and quasi-steady flow work producing devices [1]. The modern generation of internal combustion engines is the most efficient but still there is room for improvement. Rising consumption and fast depletion of the fossil fuels are major reasons for the improvement in efficiencies. The rise in fuel consumption is related to population growth across the globe. World population was estimated to be 2.5 billion in 1950 and is projected to be approximately 9 billion in 2050 [2].

Particularly influence of population growth on energy usage patterns is the large increase in urban population compared to the growth in rural population. Coupled with the emergence of new economic players such as China and India has resulted in a massive increase in primary energy consumption. The data presented in BP Statistical Review 2012 [3] suggests that growth in global $CO_2$ emissions due to energy usage continued in 2011, but at a slower rate than in 2010.

The oil production and consumption trends from 1986 to 2011 have been shown in Figure 1.1. At the end of 2011, the world's proven oil reserves stand at 1652.6 billion barrels. These reserves are sufficient to meet current world production for 54.2 years. Figure 1.2 shows the current reserves over production ratio as well as its historical trends for different regions in the world.

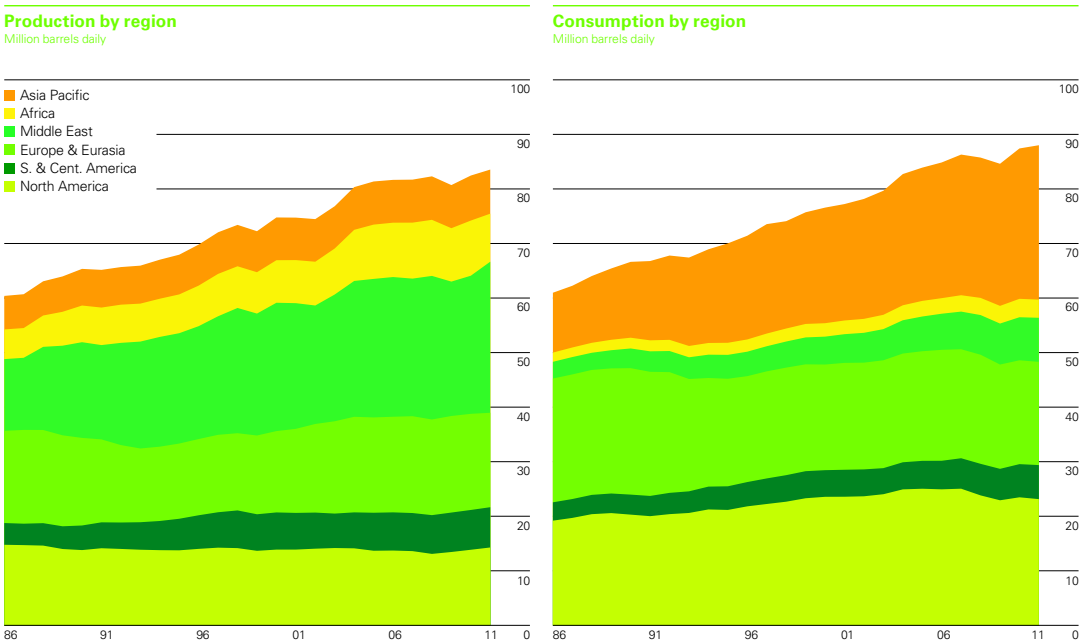


Figure 1.1. Oil production and consumption trends from 1986 to 2011 [3]

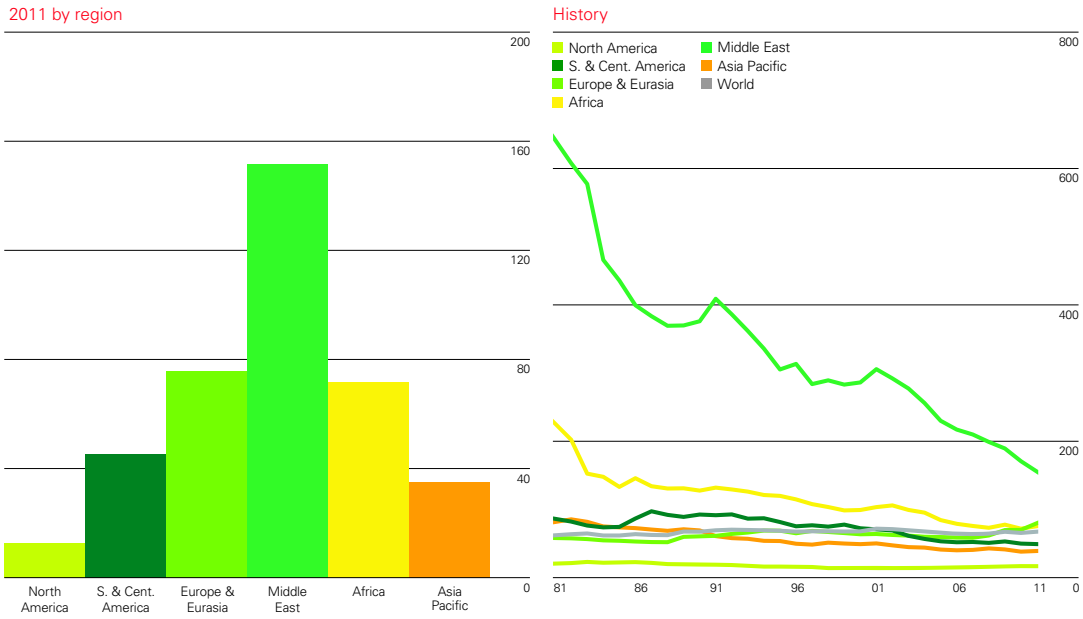


Figure 1.2. Current reserves over production ratio of crude oil and its historical trends for different regions in the world [3]

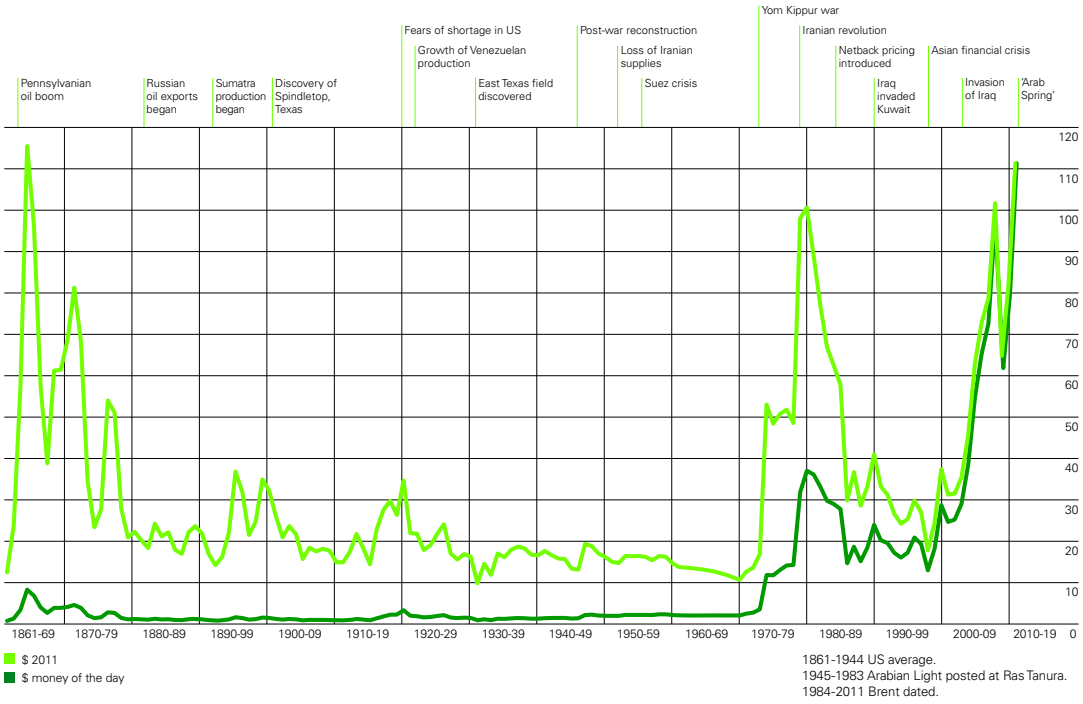


Figure 1.3. Historical trends in oil prices along with major events affecting the prices during a period of 1860 to 2010 [3]

The fluctuations in the crude oil prices have resulted in great public concern from an energy security perspective. Figure 1.3 depicts historical trends in oil prices along with major events affecting the prices during a period of 1860 to 2010. Crude oil prices exceeded $100 per barrel for the first time ever. A number of political developments in oil producing nations such as Libya have had major influences on the oil price. The growth in world energy consumption was recorded as 2.5% with 33.1% of the global energy consumption fueled by crude oil which remains the major contributor, although it continued to lose market share for the twelfth consecutive year. As IC engines are going to continue as the major prime mover, their fueling mechanism must be secure, sustainable and cost effective.

### 1.1.1 Emissions Standards

Apart from ensuring the fuel supplies to operate these IC engines, clean burning of these fuels is a another major challenge. The standards regulating different emissions from

| Standard | Year | CO | HC | $NO_X$ | PM |
|---|---|---|---|---|---|
| Euro I | 1992 | 4.5 | 1.1 | 8.0 | 0.612 |
| Euro II | 1996 | 4.0 | 1.1 | 8.0 | 0.36 |
| Euro III | 2000 | 2.1 | 0.66 | 8.0 | 0.15 |
| Euro IV | 2005 | 1.5 | 0.46 | 3.5 | 0.02 |
| Euro V | 2008 | 1.5 | 0.46 | 2.0 | 0.02 |
| Euro VI | 2015 | 1.5 | 0.13 | 0.4 | 0.01 |

Table 1.1. European emissions standards for heavy duty diesel engines - steady state testing g/kWh [5]

IC engines are getting stricter every year. These emissions include oxides of nitrogen such as NO and $NO_2$ (collectively known as $NO_X$), oxides of carbon such as $CO_2$ and CO, unburnt hydrocarbons (HCs) and soot. A parallel rise in $CO_2$ levels and the global temperature

| Standard | Year | CO | NMHC | $NO_X$ | PM |
|---|---|---|---|---|---|
| Euro III | 2000 | 5.45 | 0.78 | 5.0 | 0.16 |
| Euro IV | 2005 | 4.0 | 0.55 | 3.5 | 0.03 |
| Euro V | 2008 | 4.0 | 0.55 | 2.0 | 0.03 |
| Euro VI | 2015 | 4.0 | 0.16 | 0.46 | 0.01 |

Table 1.2. European emissions standards for heavy duty diesel engines - Transient testing g/kWh [5]

suggests that the $CO_2$ added into the atmosphere due to different human activities is causing global warming. It has also been established that the emissions from fossil fuel combustion contain some carcinogenic compounds, smog causing compounds and acid rain causing compounds which lead to respiratory problems in humans and general degradation to the environment. To counter these emissions governments and various agencies have introduced a range of standards to cap these emissions [4]. The implementation of Euro I in 1992 to the enforcement Euro VI in 2015 is an example of such an emissions cap placed on manufactures.

As reflected in the Table 1.1, the standards for different emissions have become progressively stricter with every new release. Euro I came into force in 1992 and Euro VI shall be promulgated in 2015 with the standards for various emissions getting tighter and tighter. For instance, 5.0 g of $NO_X$ were allowed per kWh in Euro III for the transient conditions this is reduced to 0.46 g/kWh in Euro VI.

### 1.1.2 Realistic Efficiencies

A new generation of power plants is required to achieve the higher thermal efficiencies and reduced emissions levels. Innovations ranging from improvements in fuel injection techniques, such as introduction of common rail fuel injection system, to the electronic control

of different events such variable valve timing are just two examples of the developments made to meet these standards [4]. Low speed marine diesel engines are the largest and the most advanced reciprocating engines with maximum efficiency between 50% and 55% [6]. Room for any further improvement in these engines can be evaluated by comparing their current thermal efficiency values against their Carnot coefficients. The Carnot coefficient provides the maximum efficiency of a heat engine operating between two reservoirs at different temperatures. These reservoirs are generally referred as a hot reservoir and a cold reservoir. The Carnot coefficient for these engines can be evaluated as follows

$$\eta = 1 - \frac{T_C}{T_H} \tag{1.1}$$

When the Carnot coefficients is calculated between the adiabatic flame temperature (around 2500K) and the room temperature, it comes out to be 88%. The adiabatic flame temperature is not a true representation of a hot reservoir for IC engines as this occurs over a very small fraction of the overall cycle time [7, 8]. Also the cold reservoir is generally at much higher temperature when compared to the environmental temperature. This is because the temperature of the charge through out the exhaust process is higher than the environmental temperature [9]. A realistic estimate would be to take the metal temperature (for example piston top) as representative of the hot reservoir and the cooling water temperature as a cold reservoir temperature. Taking the temperature of the piston top to be around 900K and that of cooling water to be 340K, the Carnot coefficient is estimated to be 62% [6, 4].

Internal combustion engines do not follow a thermodynamic cycle, they follow a mechanical cycle. However the similarity between the indicator diagrams of the IC engines and the air standard cycles makes it possible to compare the two thermal efficiencies. The engine's indicator diagram is a record of pressure versus instantaneous volume of the cylinder. Simple air standard cycles are very useful and it is convenient to compare IC engines with standard air cycles. One of the reason for this comparison is that one of the main constituent of the working fluid is nitrogen which remain virtually unchanged in both the IC

engines as well as in these standard air cycles. Non ideal behavior of air/fuel mixture in IC engines presents one of the limitations of the standard air cycles to explain the former [1].

$$\eta_{Diesel} = 1 - \frac{1}{\gamma}.\frac{\alpha^{\gamma} - 1}{\alpha r_v^{\gamma-1} - r_v^{\gamma-1}} = 1 - \frac{1}{r_v^{\gamma-1}}[\frac{\alpha^{\gamma} - 1}{\gamma(\alpha - 1)}] \tag{1.2}$$

The efficiency of diesel cycle does not depend only on compression ratio. It also depends on the load ratio as well. Comparing diesel cycle efficiency to the Otto cycle efficiency, we can observe an additional term in the formula. $[\frac{\alpha^{\gamma}-1}{\gamma(\alpha-1)}]$. The load ratio $\alpha$ lies in the range $1< \alpha > r_v$ and due to this reason the term in the square brackets is always greater than unity and hence the diesel cycle efficiency is always less than the Otto cycle if the compression ratio is the same. For a compression ratio of 16, the theoretical efficiency of an otto cycle is around 75%. On the other hand, for the same compression ratio, the theoretical efficiency of diesel cycle is around 55% if the load ratio is set at 5 and $\gamma$ is set at 1.4. Whereas if the compression ratio is set at 25 and the load ratio is set at 10, for a $\gamma$ value of 1.4, the theoretical efficiency of the diesel cycle is 65% [12]

Although the efficiency of these marine engines is reaching their theoretical maximum but they do not represent the majority of the engines. There is a significant room for improvement in smaller reciprocating engines.

Conventional IC engine fuels are finite source of energy. They have specific properties that govern IC engine operation inherently limiting the scope of IC engine operation (i.e. knock limits and $NO_X$ emissions). It has been found that various alternative fuels have been investigated to substitute the conventional liquid fuels in IC engines or at least supply a fraction of the total energy required. Contradictory claims about the improvement in thermal efficiency and especially the reduction in emissions have been reported when IC engines are fueled by these alternatives. This study focuses on the development of performance and emissions maps for three different alternate fuels across the full operating range of the engine. Different performance and emissions parameters have been mapped on the speed versus power graphs. These maps are a novel approach to present the performance

and emission data and help to explain differing trends in the literature. Literature has been reviewed and reported in the following pages covering different aspects of these fuels with special emphasis on resources, production and storage.

## 1.2 GENERAL CAUSES AND TRENDS IN ENGINE EMISSIONS

This section covers general causes and trends in various engine emissions.

### 1.2.1 $NO_X$ Emissions

The principle source of $NO_X$ is the oxidation of atmospheric nitrogen. $NO_X$ is formed in all places of higher temperature behind the flame front. Chemical reactions between molecules of oxygen and nitrogen that do not attain equilibrium are responsible for this $NO_X$ formation. Some of the most important variables that contribute to $NO_X$ formation in SI engines include equivalence ratio, burnt gas fraction and spark timing. The burned gas fraction can further be influenced by load, valve timing, speed, air/fuel ratio and compression ratio. Due to the diluting effect of the burnt gases, the flame temperature is reduced as the heat capacity of the cylinder charge per unit mass is increased. Variation in spark timing significantly affects $NO_X$. Advancing the spark timing results in burning of more fuel before TDC and hence higher peak cylinder pressure. This higher peak cylinder pressure results in higher temperature and hence the higher $NO_X$ [10].

In CI engines, the fuel distribution is inhomogeneous as the fuel is injected into the cylinder around TDC. This fuel distribution and variation in fuel distribution with respect to time strongly affects the engine emissions. Owing to the non-uniform distribution of fuel, maximum $NO_X$ occurs in those regions where fuel/air ratio is close to stoichiometric. Part of the in-cylinder mixture which burns early in the combustion process results in higher temperatures and hence plays a pivotal role in $NO_X$ formation rate. The NO chemistry is frozen once the peak pressure point in the cycle is passed as the temperature decreases after this point. This decrease in temperature is attributed to expansion as well as increased

heat transfer to the cylinder walls [10].

### 1.2.2 CO and HC Emissions

Equivalence ratio is the major factor responsible for CO emissions. As SI engines usually operate close to stoichiometric conditions, they release a significant amount of CO. On the other hand, CO emissions from diesel engine operations are negligible as they operate under lean conditions. Unburned Hydrocarbons are a result of incomplete combustion of hydrocarbon fuel. The magnitude of unburned hydrocarbons is a strong function of fuel composition. Presence of benzene groups and alkenes result in higher concentration of HC emissions. For spark ignition engines, there are four possible mechanisms that can result in the emission of unburned hydrocarbons.

- Flame quenching at the combustion chamber walls
- Filling of crevice volumes with unburned mixture
- Absorption of fuel vapor into oil layer on the cylinder wall during intake and compression processes
- Incomplete combustion in a fraction of engine's operating cycle

In addition to the reasons stated above, in a CI engine fuel may also avoid normal combustion via two additional paths: either the fuel air mixture is too lean to auto-ignite or too rich to ignite. The former condition is known as over-leaning whereas the latter is termed as under-mixing. During both of these conditions a portion of the fuel remains unconsumed and is emitted as HC.

## 1.3 FUELING CI ENGINES

A significant percentage of passenger vehicles and 100 % of goods vehicles and buses use compression ignition engines [11]. It is therefore important to assess how fuelling of CI engines may be improved with suitable alternatives to mineral diesel.

### 1.3.1 Biodiesel

Biodiesel is a generic name given to different fuels derived from non fossil resources [13]. First-generation or conventional biodiesels are made from sugar, starch, or vegetable oil. These are usually mono-alkyl esters of long chain fatty acids derived from renewable sources such as vegetable oils or animal fats. Biodeiesel can be produced from planta-

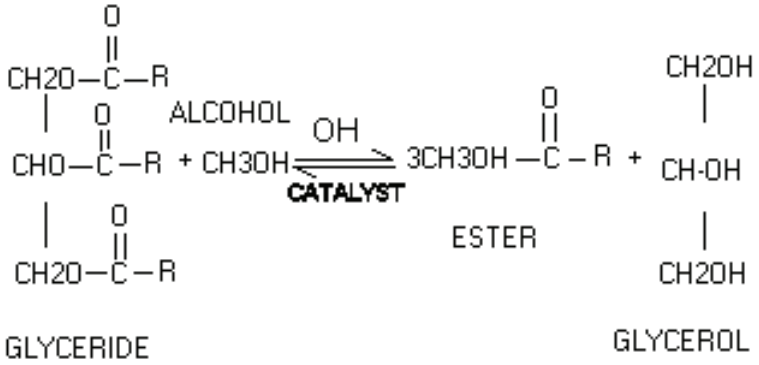


Figure 1.4. Formation of biodiesel from glycerides and alcohols

tion/vegetation, animal fats, tallow of waste cooking oil. The process through which these oil are converted into biodiesel is called transesterification [14]. Rapseed, palm and soyabeen are generally the sources from which suitable oils are extracted and then converted into biodiesel through the transesterification process. Triglycerides in the form of raw oil react with an alcohol (usually methanol) to a methyl ester (biodiesel) and glycerine [15]. Transesterification process occurs at elevated temperature ($60^0$C) and a pressure (0.2 MPa) in the presence of a catalyst (generally an alkali like NaOH or KOH). Transesterification of rapeseed oil with methanol is done to improve the cetane number and reduce the viscosity. With this transesteification , the rapeseed oil becomes a promising fuel for compression ignition engines [16].

Though oils sourced from the agriculture sector present a great potential for biodiesel production there are major challenges to source it from this route. It is expensive, both to produce the oil from the raw crops and transesterification to convert the raw oils into

biodiesel. The commulative cost of these two processes make biodiesel less cost effective than standard diesel. There is also a debate going on that biodiesel sourced through this route may interfere with the food chain. To fully appreciate the sustainability of biodiesel, a full life cycle assessment should be made. A life cycle assessment of input energy to produce soyabean based biodiesel made through transesterification compared with that of standard diesel shows that 1 MJ of conventional diesel fuel energy needs 1.2 MJ of overall input energy whereas the 1 MJ of soyabean biodiesel requires 1.24 MJ of input energy [17]. The input energy requirements vary with feedstock. For instance, if Jatropha oil is used to produce the biodeisel, the energy requirement varies between 0.68 to 1.43 MJ for every 1 MJ of biodiesel fuel energy [17]. Soil fertility, local weather and irrigation levels are some of very important factors affecting the energy requirements.

The life cycle assessment of $CO_2$ produced suggests that 1 MJ of standard diesel fuel produces 95 g of $CO_2$ compared to 41g of $CO_2$ for 1 MJ of biodiesel. The difference in $CO_2$ levels is due to some $CO_2$ being consumed during photosynthesis process while the feedstock is growing. Some other studies have placed this reduction at 80% and have attributed this to the same reason [18].

Biodiesels made from the seed crops are generally termed as first generation biofuels. 72% of Europe's cultivable land would be required to meet 10% of its primary energy requirement. The same amount of energy can be produced if 3% of Brazil's agricultural land is utilised [19]. This is one reason why the use of first generation biofuels for energy production raises the question of competition between food and fuels. It is increasingly understood that first generation biofuels (produced primarily from food crops such as grains, sugar beet and oil seeds) are limited in their ability to achieve targets for oil-product substitution, climate change mitigation, and economic growth. Their sustainable production is under review, as is the possibility of creating undue competition for land and water used for food and fibre production. A possible exception that appears to meet many of the acceptable criteria is ethanol produced from sugar cane. The cumulative impacts of these

concerns have increased the interest in developing biofuels produced from non-food biomass. Feedstocks from ligno-cellulosic materials include cereal straw, bagasse, forest residues, and purpose-grown energy crops such as vegetative grasses and short rotation forests. These 2nd-generation biofuels could avoid many of the concerns facing 1st-generation biofuels and potentially offer greater cost reduction potential in the longer term.

**Biodiesel Properties**

Biodiesel exhibit different physical properties when compared to standard diesel. Lower heating value of biodiesel is lower than diesel (38600 kJ/kg and 42000 kJ/kg respectively) [20]. Apart from lower energy content, slightly higher density as well as viscosity of the biodiesel also play their role [21, 22]. Viscosity, density and surface tension are the fuel properties that have been some of the most important physical properties that affect the atomization in a CI engine. A fuel with higher viscosity can delay atomization process which in turn affects combustion negatively. High viscosity and high density of biodiesel compared to mineral diesel fuels can cause problems in pumping and atomization of fuel [22]. Transesterification, mixing with lighter oils and heating are all effective techniques to reduce the viscosity. Owing to its chemical composition, biodiesel has extra fuel-in oxygen [21, 23, 24, 25]. Biodiesel has a higher cetane number [26, 27].

**Combustion of Biodiesel in CI Engines**

In a previous study, it has been shown that the brake specific fuel consumption (BSFC) of a DICI engine increases when rapeseed methyl ester (RME) substitutes diesel [20]. Lower energy content of biodiesel is held responsible for this trend and hence more fuel needs to be injected to overcome these power losses. This results in higher BSFC. When biodiesel-in-diesel blends are tested in CI engine, the BSFC is still higher when compared to the pure diesel based case. The BSFC have been reported to decrease with increase in engine load. This trend has been attributed to the fact that higher percentage increase in brake

power with increasing load dominates the percentage increase in specific fuel consumption. But Gumus [28] presented different view point and showed that BSFC decreases initially with increasing load until it reaches a maximum value and then it starts increasing again.

Thermal efficiency has been reported to be maintained with pure biodiesel as well as with biodiesel-in-diesel blends compared to cases when pure diesel is used [29, 15, 14]. Some studies have reported slight reduction in thermal efficiency [22] and it has been attributed to higher viscosity of the biosiesel used.

It has been reported that power outputs are comparable to pure diesel fuelling [29, 15, 14]. Some studies report a slight reduction in power at high power settings [22]. Lin et al [22] have tested 8 kind of Vegetable Oil Methyl Esters. They reported power difference ranging between -0.64% to +1.49% and believed that the higher density, higher BSFC , higher oxygen content and higher combustion rate are responsible for this power recovery despite the lower heating value of biodiesel. Similar kind of trend is observed by [30] but they have explained it differently. According to them, the fuel delivery to the engine is on volumetric basis and the higher density of biodiesel is responsible for extra supply of the fuel to compensate lower heating value. Viscosity of biodiesel is higher than diesel fuel and this fact has been used for and against the power recovery argument. Some authors believe that higher viscosity of biodiesel enhances fuel spray penetration. This greater fuel penetration improves air/fuel mixing and has been held responsible for greater power [22]. On the other hand, some other authors [31, 32] are of the view that this higher viscosity shall serve otherwise. To them, higher viscosity should decrease the combustion efficiency due to bad fuel injection/atomization and hence power should be lost.

A review article by Xue [33] have concluded that 70.4% of the 27 literatures studied agree that engine power will drop in case of biodiesel owing to its lower heating value. The same study has reported that some authors have held the opinion that the loss of power due to lower heating (when compared to the diesel fuel) value was less than expected and this has been attributed to power recovery. Yucesu et al [34] have compared the loss of heating

value to the loss of power. They suggested a 6% power decrease compared to a 5% decrease in heating value when biodiesel was used in comparison to mineral diesel. The difference is attributed to difficulties in fuel atomization instead of heating value only. Some authors have also reported that there is no significant difference in engine power between diesel and pure biodiesel. Biodiesels exhibit shorter ignition delay compared to pure mineral diesel. This is a consequence of higher cetane number of biodiesel [31, 32].

**Emissions from Biodiesel Combustion in CI Engines**

There is an inconsistency in the literature reported on $NO_X$ emissions from the combustion of biodiesels compared to pure mineral diesel. The studies which report lower $NO_X$ compared to diesel hold that this is due to higher density and viscosity of the biodiesel which result in different injection and spray characteristics [33]. Those who have reported higher $NO_X$ rely on higher bulk modulus, shorter ignition delay and higher oxygen content in the fuel all of which result in higher localised temperatures [21, 23, 24]. Nabi et al [35] reported 15% increase in $NO_X$ when pure biodiesel was used at high load conditions. The authors have attributed this increase in $NO_X$ to the 12% increase in oxygen content at that particular load conditions. In a comprehensive review article by [33], some authors have reported that the use of pure biodiesel does not make any significant difference to the production of $NO_X$ whereas some other authors (29% of the total literature reviewed) reported reduction in $NO_X$. Cetane number, injection and combustion advance and higher oxygen content are commonly reported factors that affect $NO_X$ emissions. Biodiesel has a higher cetane number leading to shorter ignition delay, advancing combustion [26, 27, 36]. The higher cetane number, higher $NO_X$ argument presented above was questioned by [37]. This work proposed that higher cetane number not only leads to early burning of the fuel but also reduces pre-mixed combustion. This reduced pre-mixed combustion results in milder changes in temperature and pressure and thus leads to lower $NO_X$. Oxygen content in biodiesel is another factor that is generally accepted to cause an increase in $NO_X$. Labeckas et al [25]

showed that there was a proportional increase in maximum $NO_X$ emission as the oxygen percentage was increased in diesel-RME blends.

Any increase in load increases overall fuel air ratio and this increased fuel air ratio results in higher $NO_X$ formation [33]. The $NO_X$ emissions are also affected by the engine speed. There are inconsistencies with the effect of engine speed on $NO_X$ emissions. One argument states that as the engine speed increases, it causes an increase in $NO_X$ due to higher combustion temperatures [27]. Other studies have found a reduction in $NO_X$ emissions with increasing engine speed [38]. Shorter residence time available for $NO_X$ formation has been held responsible for this decrease in $NO_X$ formation as the engine speed increases. The higher bulk modulus results in advanced injection timing, higher rate of pressure rise during premixed combustion phase and higher in-cylinder temperature. It has been reported that higher bulk modulus helps the sound to travel at a faster speed. The higher speed of sound transfers the pressure wave from an in-line fuel pump to the injector needle quickly, resulting in early injection of the fuel [39]. The bulk modulus and the speed of sound are related through the following Newton- Laplace equation

$$c = \sqrt{\frac{C}{\rho}} \tag{1.3}$$

where C is the bulk modulus and $\rho$ is the density of the medium. The bulk modulus of biodiesel is 10% higher when compared to that of pure mineral diesel but the density of the biodiesel is also higher. The above equation shows that the speed of sound has weak dependence on the bulk modulus if the density of the medium is also increased. It can be concluded that this bulk modulus alone can not explain the higher $NO_X$ in case of biodiesel. There are also some other factors responsible for the higher $NO_X$ with biodiesel.

Reduced PM emissions are resulted when CI engines are fuelled by biodiesel instead of diesel [32, 22, 30, 28]. The order of PM emission reduction has been reported to be 20% to 50% [29, 40, 14, 21]. The extra oxygen in the fuel is generally held responsible for the oxidation of more carbon and hence reduction of PM. Low levels of aromatic and sulphur

content as well as high cetane number of biofuels have also been reported to influence PM emission reduction [23, 41]. Biodiesel does not contain any aromatic content which is generally a PM precursor. Higher cetane number results in advance in combustion and hence prolongs the residence time of soot particles in the high temperature environment. This prolonged residence time has been reported as one of the parameters that help oxidize some further soot. Some studies including [31] have dissented from this perspective and have reported an increase in PM emission. This increase in PM emissions is explained on the grounds of higher viscosity of the biodiesel leading to poor fuel atomization reducing combustion quality.

The engine load has been reported to affect the PM emissions directly [24] as well as inversely [42]. The increase in PM emissions have been explained on the basis of decreased air fuel ratio at higher loads as larger quantities of fuel are injected in to combustion chamber. The PM emissions are lowered as the engine speed is increased. Greater turbulence at higher speeds improves the combustion efficiency and hence reduce the PM emissions. Higher fuel consumption due to lower heating value can also cause an increase in HC emissions in case of biodiesel. Reduction in CO emissions have been reported when diesel is replaced by biodiesel [31, 23, 32, 24, 30, 28]. It has widely been reported that this reduction in CO levels is due to increased oxygen content that results in complete combustion [31, 24, 30]. Higher cetane number has also been pointed out as one of the reason for this CO reduction as higher cetane number lowers the possibility of fuel rich zones [37]. Some authors observed no difference in CO levels when a CI engine was fuelled by biodiesel [27]. Some other authors [43] have observed an opposite trend i.e. increase in CO emissions when diesel is replaced by biodiesel. The authors explained this trend on the grounds of higher viscosity and poor atomisation characteristics. Changes in engine load affect CO emissions. Some authors have reported increase in CO emissions when engine load was increased. They attributed this trend to a decrease in air/fuel ratio as the load increases [28]. On the other hand, it has been reported that CO emissions reduced when the

engine load was increased. This trend was explained on the basis of higher combustion temperature that resulted in more complete combustion [44]. Increase in engine speed causes decrease in CO mainly due to better air fuel mixing at higher speeds [30]. HC emissions are reduce when biodiesel replaces diesel, is a predominant viewpoint [24, 22]. Majority of the authors explain this trend on the basis of better combustion due to excess oxygen present in case of biodiesel when compared to pure diesel. On the ohter hand, all those authors who concluded opposite to this popular trend rest their argument on realtievely poor atomization and lower volatility of biodiesel [45].

Some studies have assessed the effects of long term use of biodiesel in IC engines [29, 40]. 40% less carbon deposits have been reported when biodiesel is used to fuel the CI engines. Other studies maintain that there is no difference in terms of engine wear due to long term use of biodiesel. Some soap build up in engine's lubricating oil have been reported in such cases [29, 40].

## 1.4 NATURAL GAS AS AN AUTOMOTIVE FUEL

Natural gas has long been investigated as a possible IC engines fuel. It is the cleanest of all the crude oil derivatives. Methane is the major constituent of the natural gas (92%). Table 1.3 summarizes the composition of natural gas. Natural gas can be used in either spark ignition or compression mode. The spark ignited natural gas engines run at higher compression ratio when compared to the conventional spark ignition engines and produce higher thermal efficiency and increased $NO_X$ [46, 47, 48]. In compression ignition engines, an additional source is required to ignite the natural gas. This is generally termed as dual fuel operation where a high cetane fuel such as standard mineral diesel or RME is used to ignite the compressed mixture of air and natural gas. The liquid fuel that serves as a source of ignition is termed as pilot fuel.

Table 1.3. Composition of natural gas

| Constituent | Percentage |
|---|---|
| Methane | 92 % |
| Ethane | 3 % |
| Propane | 0.7 % |
| Butane | 0.02 % |
| Pentane | 0.10 % |
| Cabon Dioxide | 0.60 % |
| Nitrogen | 3.58 % |

### 1.4.1 Natural Gas Production and Supply

The proven natural gas resources are more than any other fossil fuel derivative. The proven reserves of world's natural gas reserves at the end of 2011 were 208.4 trillion cubic meters. Figure 1.5 presents production and consumption trends for natural gas in different regions of the world. These are sufficient to meet 63.6 years of production [3]. Some major additions in Turkmen reserves pushed the reserve to production ratio for Europe and Eurasia to 75.9 years.

Natural gas consumption grew by 2.2 % while its production increased by 3.1 %.

Natural gas can not replace the conventional fuels for the near term as there is a lack of dedicated distribution and re-fueling infrastructure for the automotive vehicles. However some countries like Brazil do have this distribution network where 2000 refueling exist to serve around a million natural gas vehicles [49].

Being a derivative of crude oil, the natural gas is not a renewable fuel. Methane can be produced through some renewable (biological) routes [50, 51]. Landfill or biogas is a product of anaerobic biological decomposition. Methane constitutes at least 50 % of

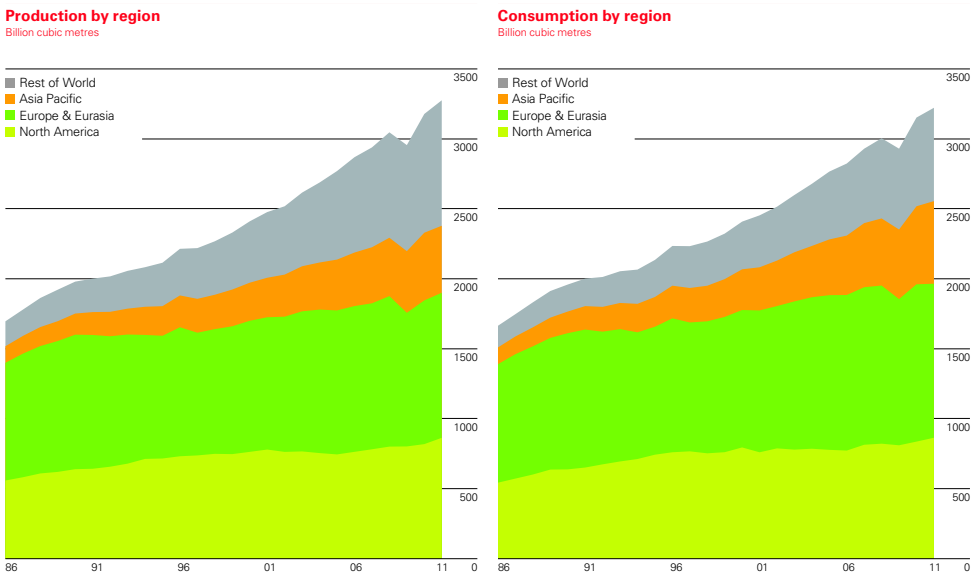


Figure 1.5. Production and consumption trends for natural gas in different regions of the world

the landfill with $CO_2$, traces of hydrogen, hydrogen sulphide and nitrogen making up the remainder [46]. The composition of the landfill suggests that it needs purification before use. This adds complexity and cost to the process. The well to wheel (WTW) life cycle assessment of fossil natural gas suggests that it produces $CO_2$ of the same orders of the liquid fossil fuels whereas the production of methane from the landfill route produces far less $CO_2$ (-250 g/Km) [52, 53, 54]. The negative value of $CO_2$ as assessed from the life cycle assessment suggests that the production of natural gas through this renewable route can help to reduce the overall $CO_2$ levels.

### 1.4.2 Use of Natural Gas in Compression Ignition Engines

Natural gas does not auto ignite in compression ignition engines. It is therefore generally utilized in a dual fuel mode where a liquid fuel pilots the combustion which then ignites the natural gas and air mixture [55]. Natural gas combustion is pre-dominantly diffusion phase combustion but higher peak pressures are measured in natural gas dual fuel operation. Some studies [56, 57] have reported double ignition delay in case of natural gas dual fueling.

The first delay is associated with the ignition of pilot fuel whereas the second delay is associated with ignition of natural gas air mixture. It has been reported that the ignition of the pilot fuel is slightly delayed when compared to the pilot fuel based single fueling operation. When operated in compression ignition dual fueling mode, the natural gas combustion produces lower $NO_X$ and higher unburned hydrocarbons [58, 59, 60, 61, 62, 63, 64, 65]. Lower $NO_X$ are generally attributed to lower combustion temperature resulting from the lower flame speed in case dual fuel mode. It has been reported that most of the $NO_X$ formed during the combustion of natural gas are resulted from the combustion of pilot fuel. Hence the quantity and type of pilot fuel can significantly affect the formation of $NO_X$. Limited literature is available to assess the affect of pilot fuel type in general and the pilot fuel quantity in particular. This thesis addresses this aspect in great detail and assesses the effect of pilot fuel quantity and type on the combustion and emissions of natural gas in dual fuel mode.

The natural gas based dual fueling results in lower smoke and particulate matter emissions and some studies have reported that these emissions are not detectable. Lower PM emissions are generally attributed to lower carbon content and higher hydrogen to carbon ratio. Induction technique of natural gas also plays its part in reducing PM emissions. If the natural gas is inducted into the intake manifold, it has more time to mix with air resulting in a near homogeneous mixture [58, 60, 62, 63, 65]. HC emissions are generally higher in case of natural gas based dual fueling when compared to the pilot fuel based single fueling. Most studies agree that HC emissions are generally higher at part load conditions when natural gas is utilized in a dual fueling mode in CI engines. CO emissions exhibit similar trends to HC emissions. Some studies have reported that CO levels of natural gas based dual fueling reach the level of diesel based single fueling at the highest load conditions [59, 61, 62, 63, 64]. Studies have been conducted to improve these carbon based emissions resulting from the combustion of natural gas dual fueling. Increased quantity of the pilot fuel and use of EGR have been reported to improve CO emissions in these

cases [59, 60, 61, 65].

## 1.5 HYDROGEN AS AN AUTOMOTIVE FUEL

Recently hydrogen has gained a lot of attention as a possible long term substitute to the conventional IC engine fuels. Production of hydrogen through renewable means is the chief reason for this attention. With fast depleting resources of fossil fuels, any renewable source of energy is much likely to be at centre stage of research community. Steam reforming of hydrocarbons (mostly methane) and electrolysis of water are the common methods of hydrogen production. Hydrogen is a promising fuel for the future due to:

- Renewability is a plus point for hydrogen [66].
- Significantly larger value of lower heating value
- Hydrogen shows wider flammability range. It shows $0.1 \leq \phi \leq 7.1$ as compared to the gasoline that shows $0.2 \leq \phi \leq 4.0$. Ultra lean mixtures can be utilized [67].
- Higher flame speed, shorter combustion duration and hence higher thermal efficiencies [68].

The life cycle assessment of hydrogen production through various routes reveals that the amount of green house gases produced varies with the production method but all of these produce less greenhouse gases compared to the conventional crude oil derivatives [4]. Hydrogen is often projected as a zero emissions fuel, however this statement depends upon the source from which it is produced. Due to its composition and physical properties hydrogen combustion produces water and $NO_X$ emissions. Although there are no immediate carbon based emissions from the combustion of hydrogen, higher $NO_X$ and abnormal combustion are serious challenges. Pre-ignition and "hydrogen knock" generally constitute abnormal combustion.

### 1.5.1 Overview of Hydrogen Gas Production

Hydrogen does not exist as a free element on as earth. It is found in the combined form in different hydrocarbons and water [58]. There are generally two routes through which hydrogen is produced [69]: steam reforming of methane and electrolysis of water. The steam reforming is completed in two steps

- Production of Water Gas
- Oxidation of CO to $CO_2$

Through an endothermic catalytic reaction, methane is converted into CO and $H_2$. This mixture of hydrogen and carbon mono-oxide is called water gas. The next step is called water shift reaction which is the oxidation of CO into $CO_2$. Electrolysis of water involves the passing of a current through pure water to split it into its constituent elements. The $CO_2$ production during electrolysis depends upon the source of the electricity [70]. Any life cycle assessment of the use of hydrogen needs to take into account the $CO_2$ produced irrespective of the method of production [70, 53].

### 1.5.2 Combustion of Hydrogen in IC Engines

It is difficult to ignite hydrogen in compression ignition engines [71]. Due to hydrogen's low cetane number, it can not ignite spontaneously under these conditions. It has been reported that hydrogen may not ignite even under extreme compression ratios ranging up to 29:1 [72]. Constant volume bomb experiments reveal that a temperature of more than 1100 K is needed to ignite hydrogen whereas diesel is ignited below 1000 K. The same study reports that the hydrogen ignition is strongly dependent on the ambient temperature. Like natural gas, the hydrogen combustion utilizes the dual fueling concept [73, 74, 75, 76, 77, 78, 16, 79, 80, 81]. A high cetane liquid fuel is used to pilot the combustion of hydrogen in CI engines.

Most of the studies utilizing hydrogen induction into the intake manifold report higher

thermal efficiencies and lower volumetric efficiencies compared to standard liquid fuel. High flame speed results in an increased rate of pressure rise and temperature. Hydrogen flames also exhibit a smaller quechning distance, meaning flame travels closer to cylinder walls, increasing fuel utilisation. Combustion efficiency is improved leading to an overall improvement in thermal efficiency. The lower volumetric efficiency is due to inducted hydrogen displacing a portion of the incoming air. The higher temperatures result in higher $NO_X$ emissions [81]. It has been reported that the $NO_X$ emissions are strongly affected by the hydrogen air mixture quality and the residence time [82, 75].

The use of hydrogen as a fuel in compression ignition engine results in lower PM and CO emissions as a consequence of: the reduction in the amount of carbon present during combustion and the higher combustion temperatures helps to oxidise PM [73, 76, 77, 80, 81].

## 1.6 FACTORS AFFECTING VOLUMETRIC EFFICIENCY

In dual fuel mode, the volumetric efficiency of the engine is reduced due to the manifold induction of the gaseous fuels like natural gas and hydrogen. Volumetric efficiency is a measure of the effectiveness of an engine's induction process . This is not used for two stroke engines as they do not have distinct induction and exhaust process [10].

$$\eta_v = \frac{m_a}{\rho_{a,i} V_d} \tag{1.4}$$

where $\rho_{a,i}$ is the inlet air density and $m_a$ is the mass of air induced. Following equations describe how some of these performance parameters are inter-related for power output

$$P = \frac{\eta_f m_a N Q_{HV} (F/A)}{n_R} \tag{1.5}$$

We can introduce volumetric efficiency for four stroke engines ($n_R$).

$$P = \frac{\eta_f \eta_v N V_d Q_{HV} \rho_{a,i} (F/A)}{2} \tag{1.6}$$

The amount of air inducted during a given cycle plays a crucial towards the performance and power output of a diesel engine.

Volumetric efficiency is reduced due to interaction between hot residual gases and the fresh in-coming mixture via heat transfer between these two fluids as a result of mixing. In an ideal induction process it is assumed that, with same specific heat and molecular weights, the contraction of the residual gas as it is cooled is equal to the expansion of incoming gases when they interact. But this theory of "No change in volume due to mixing process" does not hold very true with actual induction processes. Since the ports, inlet valves and the cylinder walls are at higher temperature as compared to the inlet gases, heat transfer does occur during the process of induction causing a decrease in volumetric efficiency. Following equation reflects general dependencies of the volumetric efficiency over different variables [83].

$$\eta_v = f(\frac{u}{a}, \frac{p_e}{p_i}, \mathbf{R}, F/A, \frac{C_p T_i)}{(F/A)Q_c}, \frac{C_p T_c)}{(F/A)Q_c}) \tag{1.7}$$

where

- $\frac{u}{a}$ - Mach index through the inlet-valve opening
- $\frac{p_e}{p_i}$ - ratio of exhaust system pressure to the inlet system pressure
- F/A - fuel air ratio
- $T_i$ - inlet temperature
- $T_c$ - coolant temperature
- **R** - inlet Reynolds index

The Mach Index can be expressed as

$$\frac{u}{a} = Z = (\frac{b}{D_i})^2 \frac{s}{aC_i} \tag{1.8}$$

where

- b - bore of the cylinder

- $D_i$ - inlet valve diameter
- s - mean piston speed
- a - inlet sonic velocity
- $C_i$ - inlet-valve average flow coefficient

The inlet Reynolds Index is defined as $\rho ba/\mu g_0$ where a is the inlet sound velocity, b is the cylinder bore, $\rho$ is the density at the inlet and $\mu$ is the velocity of the inlet gases. Fuel air ratio does affect the cylinder pressure during induction and that is why it has been included in the arguments for volumetric efficiency. The terms involving $T_i$ and $T_c$ have to do with heat transfer from the engine parts to the inlet and residual gases during induction. Eq. 1.7 can be written as

$$\eta_v = f(Z, \frac{\rho ba}{\mu g_0}, \frac{p_e}{p_i}, F/A, \frac{C_p T_i}{(F/A)Q_c}, \frac{C_p T_c}{(F/A)Q_c}) \tag{1.9}$$

The engine speed affects the volumetric efficiency through term "Z" in Eq. 1.9. Volumetric efficiency starts to fall off rapidly as Z reaches close to 0.6 [83]. Any change in air fuel ratio shall change last three terms in Eq. 1.9. As the fuel air ratio increases to 1, the temperature of the induction system parts increases and more heat is transfered to gases during the induction process. Due to this reason the volumetric efficiency tends to decrease as fuel air ratio reaches 0.8. Increasing inlet temperature shall reduce the Mach Index as temperature affects sound velocity. This increase also reduces the gap between mean inlet wall temperature and mean gas temperature which in turn reduces the heat transfer to the walls and hence increases volumetric efficiency. Any increase in coolant temperature shall result in higher temperature of the induction system and hence increase heat transfer to the incoming gases. As a result of this the incoming gases shall expand and hence the volumetric efficiency drops [83]. Apart from heat transfer effects discussed above in brief, the engine design factors also have considerable influence upon volumetric efficiency. Some of these design parameters are listed below [83]

- Inlet valve size and design
- Valve timing
- Exhaust valve size and design
- Stroke to bore ratio
- Compression ratio
- Design of exhaust system
- Cam-contour shape

## 1.7 THESIS OVERVIEW

The reciprocating internal combustion engines is the most common form of engine or prime mover [1]. Currently, the automotive community around the globe is facing two major challenges. Firstly, there is a massive drive to develop new fuels for internal combustion engines due to fast depleting global reserves of oil and gas. Political turmoil in oil producing regions and exponentially growing population of the world have put serious question marks over any kind of balance between the demand and supply of the fossils fuels in future. Secondly, the community is striving hard to control the emission coming out of the engine to match the stringent emission standards which are getting strict with each passing year. Experimental investigations used to be the only way to conduct research on internal combustion engines till as late as 1980s. The emergence of computer and successful development of multi-dimensional CFD codes have provided an effective and alternate means to investigate different fuels and simulate the engine performance and predict emissions.

The current study involves both the computational as well as experimental work. Experimental work has been done on fuels that can be used in compression ignition engines and can contribute to the part of energy which is currently being supplied by the diesel

alone. Computationally, a commercial CFD codes has been used to predict in-cylinder pressure, rate of energy release, specific emissions of $NO_X$, CO and $CO_2$.

To achieve the overall key objectives following three sub-objectives were accomplished.

1. Development of performance and emissions maps for compression ignition liquid fuels like diesel and RME

2. Development of performance and emissions maps for compression ignition gaseous fuels like natural gas and hydrogen in dual fuel operation

3. Investigation of the effect of pilot fuel quantity and type on different performance and emissions characteristics of natural gas and hydrogen based dual fueling of compression ignition engines

4. Application of different spray and combustion models to predict in-cylinder pressure, rate of energy release and specific $NO_X$, CO and $CO_2$ emissions

The thesis is structured as follows. Chapter 1 is dedicated to a background review of performance and emissions characteristics of internal combustions engines. It also includes a literature review of different spray, turbulence and combustion models used to predict different in-cylinder events computationally. Chapter 2 includes a description of the experimental rig and methodology. Experimental and computational results have been presented in chapter 3 to 5. Chapters 3, 4 and 5 present different performance and emissions characteristics in a novel way. Diesel and RME performance and emissions maps have been discussed in Chapter 3. Chapter 4 and 5 cover the performance and emissions maps of natural gas and hydrogen in dual fuel operations respectively. The performance and emissions maps presented in chapter 4 to 6 include thermal efficiency, volumetric efficiency, specific $NO_X$ specific HC, specific $CO_2$, specific $O_2$ and maps for enthalpy fraction of pilot fuel in case of dual fueling cases. Chapter 6 discusses in detail the effect of pilot fuel quantity and type and engine speed on different performance and emissions parameters. A combination

two pilot fuels and three different pilot fuel settings at two different engine speeds have been used in this study. Chapter 7 includes a parametric study of two different spray models. The effect of changing the breakup length have been assessed and discussed for WAVE and and Kelvin-Helmohltz nand Rayleigh-Taylor (KHRT) spray breakup models. In-cylinder pressure as well as rate of energy release have been predicted by applying unsteady flamelet and finite rate chemistry models. The optimized spray breakup constant has been used along with unsteady flamelet model to predict $NO_X$, CO and $CO_2$ emissions. Conclusions and future recommendations have been compiled in chapter 8.

# CHAPTER 2

# EXPERIMENTAL APPARTUS DESCRIPTION AND DATA ANALYSIS

## 2.1 INTRODUCTION

This chapter explains the experimental test rig used in the investigations and the allied apparatus used to record experimental data for all investigations. Diesel and RME were used when the engine was run in single fueling mode. Diesel and RME were used as pilot fuels when a gaseous fuel was tested in a dual fuel mode. Natural gas and hydrogen were used as gaseous fuels the in dual fueling operations.

## 2.2 THE TEST RIG

A single-cylinder CI engine was used in the study to collect experimental data. It is a 1.4 litre four-stroke Gardner 1L2 direct-injection engine. The specifications of the engine are shown in Table 2.1. Figure 2.1 shows the schematic layout of the experimental rig showing hydraulic brake, fuel supply lines, various emission analysers and instrumentation. The RME used was provided by British Petroleum.

A header tank above the lab was used to source diesel fuel during the normal CI single fueling operations. The fuel was made to flow through a fuel measuring flask before it entered into the Gardner engine fuel system. The fuel measuring flask comprised of three segments each measuring 20 ml. When the engine was fueled by neat RME, an auxiliary fuel supply was used. The auxiliary fuel supply system consisted of a fuel tank and a fuel measuring flask. This fuel measuring flask was again graduated to measure 20 ml of RME. Two ball valves were used on the inlet of the Gardner fuel system to facilitate switching between either fuel source. When natural gas was tested in dual fuel compression ignition mode, the natural gas was sourced directly from the building mains supply. It was made to flow through one solenoid valve, two ball valves and two diaphragm valves. The flow rate of the incoming natural gas was metered through a natural gas flow meter (0-100 litre/min

| | |
|---|---|
| No. of cylinders | 1 |
| Bore | 107.95 mm |
| Stroke | 152.40 mm |
| Swept volume | $1394\times10^{-6}\mathrm{m}^3$ |
| Clearance volume | $115.15\ \times10^{-6}\mathrm{m}^3$ |
| Compression ratio | 13.11:1 |
| Max. Power | 11 kW @ 1500 rev/min |
| IVO | $10^o$BTDC |
| IVC | $40^o$ABDC |
| EVO | $50^o$BBDC |
| EVC | $15^o$ATDC |
| Start of fuel injection | $-24.5^o$ATDC |
| Injection pressure | 230 bar |
| Type of fuel pump | In-line |

Table 2.1. Specifications of the Gardner 1L2 Diesel Engine

scale). After passing through the flow meter, it was inducted into the engine inlet manifold via a stainless steel tube along with the incoming air under the engine's own suction. When hydrogen was tested in dual fuel compression ignition mode, it was a gaseous hydrogen with a purity of 99.995%. It was sourced from a 20 MPa compressed hydrogen gas cylinder supplied by the British Oxygen Company (BOC). A hydrogen pressure regulator with a flame arrestor fitted to the tank fed the hydrogen fuel line at 0.15 MPa . The hydrogen flow rate was metered through a flow meter (0 - 44 litre/min scale). After passing through the flow meter, the hydrogen was fed into the intake manifold of the engine (via a ball valve)

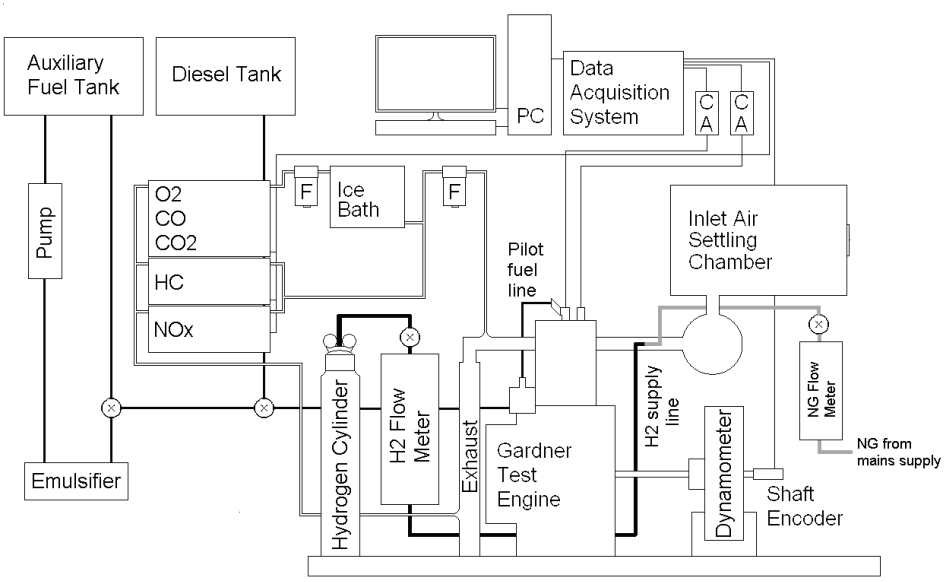


Figure 2.1. Experimental Apparatus Lay-Out

under the engine's own suction via the same stainless steel tube as natural gas. All pilot fuels were injected directly into the cylinder through the standard engine fuel system.

During natural gas dual-fuel operation the amount of pilot fuel injected is set at a flow rate providing 0.126 MPa BMEP during normal engine operation. The engine power output is then increased further by adjusting the flow rate of natural gas inducted by the engine to reach the high load regions.

During hydrogen dual-fuel operation the amount of pilot fuel injected is set at a flow rate providing 0.378 MPa BMEP during normal engine operation. The engine power output is then increased further by adjusting the flow rate of hydrogen inducted by the engine to reach the high load regions. Whilst operating at the highest load points the engine is unable to induct the required quantity of hydrogen to provide the power output. This is a result of manifold injection of the hydrogen and the low energy content of hydrogen on a volume basis. A consequence of this is that when the engine power output demand is high, a larger portion of the enthalpy must be met by the pilot fuel. As the pilot fuel quantity is to be kept constant during data collection, this led to the pilot fuel quantity being set at a level

that met the low power output demands alone, therefore hydrogen addition at the lower outputs could not be achieved, only the upper half of the standard engine load range can be achieved with hydrogen dual-fueling.

To investigate the effect of pilot fuel quantity and type on natural gas and hydrogen performance and emissions characteristics, following procedure was adopted. Three different pilot fuel settings were used for the two pilot fuels (diesel and RME) at two different speeds (1000 and 1500 rev/min ). The different test conditions can be summarized by a legend A-B-n-X-Y where A and B represent the type of emission and the type of pilot fuel respectively , n represents the BMEP setting of the pilot fuel, D and E represent the type of gaseous fuel and the engine speed respectively.

$$A = \left\{ \begin{array}{l} NO_X \\ HC \\ CO \\ CO_2 \end{array} \right\}$$

$$B = \left\{ \begin{array}{ll} D & \text{The pilot fuel is diesel} \\ RME & \text{The pilot fuel is Biodiesel (RME)} \end{array} \right\}$$

$$n = \left\{ \begin{array}{ll} 1 & \text{BMEP setting for pilot fuel is 0.125 MPa} \\ 2 & \text{BMEP setting for pilot fuel is 0.252 MPa} \\ 3 & \text{BMEP setting for pilot fuel is 0.312 MPa} \end{array} \right\}$$

$$X = \left\{ \begin{array}{ll} NG & \text{The gaseous fuel is natural gas} \\ H2 & \text{The gaseous fuel is hydrogen} \end{array} \right\}$$

$$Y = \left\{ \begin{array}{ll} 1000 & \text{Engine speed is 1000 rev/min} \\ 1500 & \text{Engine speed is 1500 rev/min} \end{array} \right\}$$

So, $NO_X$-D-1-NG-1000 shall be read as $NO_X$ emissions produced by diesel piloted natural gas combustion when the quantity of liquid fuel (diesel in this case) was fixed at a BMEP value of 0.125 MPa. When the engine was operated on natural gas based dual fueling, only higher BMEP values were considered for the three different pilot fuel settings and different emissions from the three cases were compared against each other. When the engine was run on hydrogen based dual fueling, medium and higher-medium BMEP values were considered. This is because at n=1, the pilot fuel quantity was set at minimum BMEP and maximum energy was obtained through the induction of hydrogen. At this setting (n=1), the engine was misfiring and knocking was observed with any value of BMEP beyond 0.44 MPa. When the quantity of pilot fuel was increased ( for n=2,3) it became possible to induct more hydrogen and achieve BMEP values beyond 0.44 MPa without any misfire and knocking.

The following analyzers were used to analyze the exhaust gas sampled from the test rig through steel and PTFE tubing via a heated filter (maintained at 190 degrees Celsius).

- A Signal 4000VM chemiluminescence analyser used to measure NOx emissions
- Rotork Analysis model 523 flame ionisation detector (FID) used to measure unburnt HC
- A Servomex 4210C exhaust gas analyser used to measure CO, CO2 and oxygen (O2) concentrations

Wet gas samples were fed to the $NO_X$ as well as HC analyzers via a heated line at 160° Celsius. A Servomex 4210C exhaust gas analyser measures CO, $CO_2$ and oxygen ($O_2$) concentrations on a dry-volume basis. It uses non-dispersive infrared sensors and a paramagnetic sensor. Any water content in the sample needs to be removed before it is fed to the Servomex analyzer. This is achieved through a trap and silicon oxide moisture filter. The combustion chamber pressure data (detected with a Kistler type 6123 water-cooled transducer), exhaust temperatures (detected using type-K thermocouples) were sampled to a

National Instruments data acquisition system and fed into a computer running LabVIEW program.

### 2.2.1 Experimental Data Analysis

The net energy release rate was calculated on the basis of a single-zone model based on the principle of energy conservation for a closed system [6]. Following assumptions were made

- The cylinder charge was assumed to be a single homogeneous fluid having averaged properties throughout.
- No distinction made between a burnt and unburned zones.
- The charge flowing into the crevices such as between the piston and cylinder walls is not considered.

With these above mentioned assumptions, the following equation can be written:

$$Q_{to} + W_{to} = \Delta U \tag{2.1}$$

Where $Q_{to}$ and $W_{to}$ are the heat transferred and the work done to the system by the piston. $\Delta$U is the increase in internal energy of the system going from an initial state (prior to combustion) to a final state (after combustion). The term $\Delta$U can be further subdivided into three different terms: enthalpy of the fuel (with a subscript f), internal energy of reactants (with a subscript r) and internal energy of the products (with a subscript p).

$$\Delta U = m_f u_f - m_r u_r - m_p u_p \tag{2.2}$$

where

$$m_p = m_r + m_f \tag{2.3}$$

as the mass of the products is equal to the sum of the mass of the reactants and the mass of the fuel. Eq 2.2 can be rewritten as

$$\Delta U = (m_r + m_f)u_p - m_r u_r - m_f h_f \tag{2.4}$$

Substituting enthalpy as

$$h = u + pv \tag{2.5}$$

The Eq 2.4 can be written as

$$\Delta U = m_r(u_p - u_r) + m_f(u_p - h_f) \tag{2.6}$$

$$\Delta U = m_r(u_p - u_r) + m_f[(u_p - u_f) - (P_f v_f)] \tag{2.7}$$

where the term ($u_p$ - $u_f$) can be written as

$$(u_p - u_f) = (u_p - u_p^0) + (u_p^0 - u_f^0) + (u_f^0 - u_f) \tag{2.8}$$

The terms with a superscript 0 are the standard state reference conditions. The Eq 2.7 and Eq 2.8 together can be written

$$\Delta U = m_r(u_p - u_r) + m_f(u_p^0 - u_f^0) \tag{2.9}$$

When Eq 2.9 is substitute into Eq 2.1, it results in

$$-m_f(u_p^0 - u_f^0) = -Q_{to} - W_{to} + m_r(u_p - u_r) = E_{ch} \tag{2.10}$$

where $E_{ch}$ is the gross chemical energy that results from the combustion of the fuel. The term $W_{to}$ can be replaced by -PdV in equation 2.10 and then the equation can be written as

$$E_{ch} + dQ_{to} = PdV + m_r du \tag{2.11}$$

where du = $u_p$ - $u_r$. This term du can be replaced $c_v$dT. So the equation 2.11 can be re-written as

$$E_{ch} + dQ_{to} = PdV + m_r c_v dT \tag{2.12}$$

where $c_v$ is specific heat capacity at constant volume dT is the temperature change. Substituting the value of dT from the gas equation, the equation 2.12 can be written as

$$E_{ch} + dQ_{to} = PdV + m_r c_v (\frac{VdP + PdV}{m_r R}) \tag{2.13}$$

The above equation can be re-arranged

$$dE_n = dE_{ch} + dQ_{to} = (1 + \frac{c_v}{R})PdV + \frac{c_v}{R}VdP \tag{2.14}$$

The term $dE_n$ in Eq 2.14 is the net energy change from the reactants towards the products. Dividing Eq 2.14 by dt, we obtain the rate of net energy change during this process.

$$\frac{dE_n}{dt} = (1 + \frac{c_v}{R})P\frac{dV}{dt} + \frac{c_v}{R}V\frac{dP}{dt} \tag{2.15}$$

As shown in Eq 2.15, the rate of change in the net energy conversion depends upon following factors

- The rate of change in cylinder pressure (dP/dt)
- The rate of change in cylinder volume (dV/dt)
- Instantaneous cylinder pressure (P)
- Instantaneous cylinder volume (V )
- Isochoric specific heat capacity of the cylinder charge ($c_v$) and
- Specific gas constant of the cylinder charge (R)

Complete natural gas combustion in excess air, ignited by a hydrocarbon is illustrated by the following equation:

$$C_xH_yO_z+\alpha CH_4 + \beta(x+0.25y-0.5z+2\alpha)(O_2+3.76N_2) \rightarrow (x+\alpha)CO_2 + (0.5y+2\alpha)H_2O \\ + \beta(x+0.25y-0.5z+2\alpha)3.76N_2 + (x+0.25y-0.5z+2\alpha)(\beta-1)O_2 \tag{2.16}$$

Complete hydrogen combustion in excess air, ignited by a hydrocarbon is illustrated by the following equation:

$$C_xH_yO_z+\alpha H_2 + \beta(x+0.25y-0.5z+2\alpha)(O_2+3.76N_2) \rightarrow (x+\alpha)CO_2 + (0.5y+0.5\alpha)H_2O \\ + \beta(x+0.25y-0.5z+2\alpha)3.76N_2 + (x+0.25y-0.5z+0.5\alpha)(\beta-1)O_2 \tag{2.17}$$

In dual fueling cases, the quantity of pilot is fixed and the quantity of the gaseous fuel is increased to achieve higher power at a given speed. The term $\alpha$ in the above equations is introduced to take into account the varied quantity of the gaseous fuel, be it hydrogen or natural gas. There is another term $\beta$ in both of these two equations. The $\beta$ term is used to take into account the excess air that is present in the exhaust products because CI engines generally run fuel-lean. Hence the term $\beta$ is generally always larger than unity. For stoichiometric combustion of a neat fuel during normal CI engine operation, the term $\alpha$ approaches zero while $\beta$ becomes unity.

# CHAPTER 3

# PERFORMANCE AND EMISSIONS MAPS OF DIESEL AND RME

## 3.1 BACKGROUND AND MOTIVE

Development of alternative fuels to replace the conventional fuels in IC engines is a most active area of research. Fuels derived from different resources (especially renewable ones) have been tested in IC engines with their performance and emissions characteristics investigated to assess their suitability as substitute fuels [84].

Biodiesel is a generic term applied to an ester-based fuel (fatty esters) made from vegetable oils or animal fats through a simple transesterification process [85, 86]. A number of researchers have compared different biodiesels, depending on the feedstock that is used to manufacture the biodiesel. These biodiesels are then investigated as pure fuels or blended with mineral diesel with performance, emissions and other parameters investigated [87, 88].

The lower heating value of biodiesel is lower than mineral diesel so in all cases the specific fuel consumption is shown to increase with biodiesel fueling. This is not an ideal method to examine the combustion performance of the fuels relative to each other. The thermal efficiency of biodiesel shows a general trend of being lower that standard mineral diesel [88, 89, 85]. The lower brake thermal efficiency is often attributed to the injection and atomization character of the biodiesel due to its physical properties such as viscosity, density, and bulk modulus of elasticity. The presence of oxygen in the biodiesel itself has an influence on the combustion quality [90]. To fully realize a comparison between the two fuels, and therefore comment on any effect that the physical properties may have, engine tests need to be run over the full operating range of the engine.

The major factors affecting $NO_X$ formation are: combustion temperature; local oxygen concentration; and residence time in the high temperature zone. The trend concerning $NO_X$ emissions when fueling with biodiesel is uncertain, with studies giving $NO_X$ emissions results that vary widely dependent on engine design [91]. This is demonstrated by number

of review articles which have been conducted into the so called biodiesel $NO_X$ effect [92, 93, 94, 95, 36]. The reviews identify inconsistent findings.

It is believed that engines equipped with in-line fuel pumps lead to increased $NO_X$ emissions due to an advancing of the combustion process as a result of biodiesel's higher bulk modulus [96]. The specific $NO_X$ emissions across the entire operational range of an engine is rarely considered in the literature, and addressing this aspect would be helpful in elucidating the total effect.

There is general agreement in the literature that fueling with biodiesel leads to a reduction of carbon monoxide (CO), carbon dioxide ($CO_2$) and unburned hydrocarbon (HC) emissions compared to standard mineral diesel fuelling [97, 86]. Biodiesel has higher cetane number and therefore an improved ignition quality compared to standard diesel. This is believed to lead to the reduction in HC emissions [86]. Biodiesel typically contains 10 to 11% oxygen by weight, which has a significant effect on the combustion stoichiometry and equivalence ratios. This leads to the measured reduction of CO and particulate matter (PM) emissions compared to standard mineral diesel [98, 90, 89].

There are few engine "fuel maps" available in the open literature (these are the full contours of thermal efficiency or brake specific fuel consumption plotted throughout the power versus speed range of the engine, or the torque versus speed range of the engine). Sample fuel maps can be found in [99, 10, 1]. One such thermal efficiency map with dual-fueling has been presented previously to demonstrate the thermal efficiency within the operating range of the test engine used in this study [100]. Maps showing the thermal efficiency as well as specific emissions contours on the power-speed plane are not easily found in the open literature.

The same engine can be used as a power source for different power applications, each with its own different load characteristics. For instance the same engine can be used to power: two different-size cars; a small marine vessel; an electricity generator; and in several other applications. The procedure of selecting the engine (prime mover) while considering

the engine's contours of thermal efficiency on the power-speed range of the engine, and concurrently the load line of the powered device, has been briefly described in [6]. The automobile sales literature usually quotes maximum torque at one engine speed, maximum power at another engine speed (though the vehicle is rarely operating at these conditions even on a race track), and the average fuel consumption and total emissions over one or two strictly-specified drive cycles (which may or may not be representative of the intended use of the buyer). In research papers laboratory experiments of engine performance and emissions are usually conducted at constant equivalence ratio, or constant brake mean effective pressure, or occasionally at constant speed. All of these representations are of some use to the average consumer, but they do little to represent or explain the overall thermal efficiency and emissions characteristics of engines throughout their operating range.

In the current global situation where thermal efficiency and the effect of emissions on the environment are so prominent in the public and scientific media, it seems very strange (and it is misguided) that there is little attention paid to these efficiency and emissions trends throughout the operating range of engines.

In the work presented in this chapter operation of a direct injection CI engine is considered everywhere in its power and speed operating range while it is fueled with either diesel or RME. The results are presented as contours of thermal efficiency, volumetric efficiency, equivalence ratio and specific emissions on a power-speed plane throughout the operating range of the engine. The engine is a standard test engine, typical of the majority of such engines used in the developing economies of the world; and though more-modern engines may have higher thermal efficiency and lower emissions, the shape and regions of contours presented in this chapter are representative of those shapes for typical CI engines and are applicable to all engine performance and emissions maps. This is a novel approach to representing these data, especially for CI engines. As one example of the utility of the considerations presented in this chapter, the the $NO_X$ specific emissions contours presented later illustrate that the region of high $NO_X$ emissions is at intermediate engine speed and

power, dropping off at high and low values of engine speed and power, helping to explain the $NO_X$ emission trends presented elsewhere in the literature.

## 3.2 RESULTS AND DISCUSSION

This section presents, compares and discusses the experimentally obtained maps for different performance and emissions parameters for diesel and RME fuels. As there were 48 data points in the these maps, the in-cylinder pressure and the rate of energy release data have not been presented here. The in-cylinder pressure and the rate of energy release for diesel as well as RME on selected points (one lower load and one higher load) have been presented in appendix A.

### 3.2.1 Thermal Efficiency and Volumetric Efficiency

Figure 3.2.1 presents the experimentally obtained map of volumetric efficiency for diesel fuel. The volumetric efficiency measurements for diesel and RME were practically identical; the values for diesel are shown in figure 3.2.1. Brake thermal efficiency performance maps for diesel (figures 3.2(a)) and RME (figure 3.2(b)) should be interpreted in conjunction with the volumetric efficiency map in figure 3.2.1 and the equivalence ratio maps shown in figures 3.3(a) and 3.3(b). Apart from the highest power outputs, at each operating speed the thermal efficiency map of diesel fueled operation reflects an increase in brake thermal efficiency as the power output increases. This increase in brake thermal efficiency is caused by higher combustion temperatures as the load is increased. It is noticeable that there is a decrease in brake thermal efficiency at maximum power outputs for all speeds.

The reduction of volumetric efficiency at higher engine speeds can be attributed to increased frictional losses between the incoming flow and the intake manifold. It is evident from the equivalence ratio maps that more fuel is being injected as the load increases. The combined effect leads to the different directions of the slopes in the iso-contours of

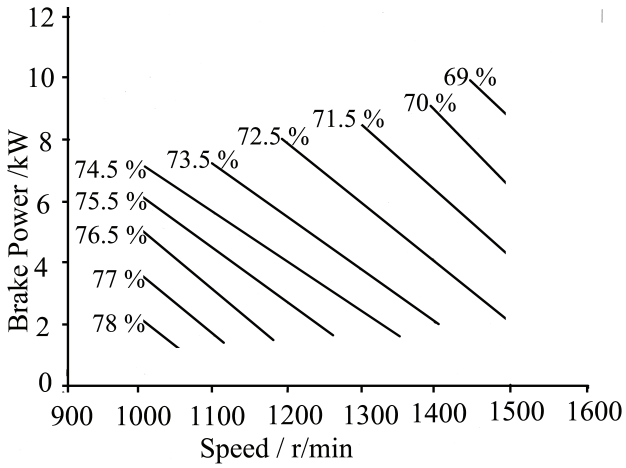


Figure 3.1. Experimentally obtained Volumetric Efficiency - Diesel

volumetric efficiency and equivalence ratio on the maps. Loss of thermal efficiency at the highest loads at each speed can be attributed to the air/fuel ratio (figures. 3.3(a) and 3.3(b)). Less oxygen is available to mix with fuel at the highest loads, causing a local drop in thermal efficiency.

The thermal efficiency map for RME (figure 3.2(b)) looks similar to the one obtained for diesel as a baseline fuel (figure 3.2(a)). While producing lower power output at all speeds, the thermal efficiency of RME is 3.5% (on average) lower than what is obtained with diesel. As demonstrated in appendix A, at lower loads, RME produces lower peak pressure when compared to diesel whereas the peak pressures for the two fuels are comparable at higher load condition. This is consistent with the findings in the literature and is often cited as an effect of poorer injection qualities. Higher viscosity of biodiesel can reduce combustion efficiency due to poor atomization characteristics. At the largest power outputs the RME has a higher brake thermal efficiency (about 3%) than the baseline diesel. This may be due to a dual effect of under-mixing in the case of diesel and the high oxygen content of the RME, which may become more significant at the higher temperatures at higher power output.

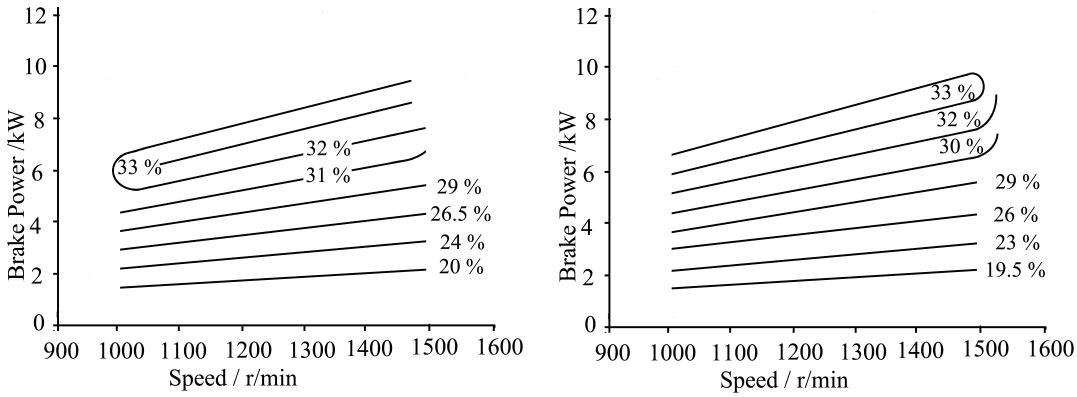


(a) Thermal Efficiency - Diesel

(b) Thermal Efficiency - RME

Figure 3.2. Experimentally obtained thermal efficiency contours of diesel (a) and RME (b)

### 3.2.2 Specific $NO_X$

The specific $NO_X$ map for diesel (figure 3.4(a)) reveals that starting at the location of maximum specific $NO_X$ at mid loads and mid speeds, the specific $NO_X$ decreases in all other directions of the operating regime. The $NO_X$ formation is dependent on operating temperature and therefore on equivalence ratio. For lower and medium speeds, the specific $NO_X$ emissions increases initially as the load is increased and then starts decreasing after reaching a maximum value. This can be attributed to the fuel-air mixture being leaner at lower loads and less lean at higher loads. This can be verified from equivalence ratio maps. At lower loads the in-cylinder temperature is lower than at higher loads as a result of less fuel being burnt per cycle. The heat transfer to any incoming charge from previous cycle gases (residuals), cylinder walls, exhaust valves and piston top land is reduced. The fuel evaporation rate upon injection is reduced leading to a smaller pre-mixed combustion phase.

This explains lower (both absolute as well as specific) values of $NO_X$ at lower loads at all speeds. As the engine load is increased the thermal efficiency of the engine increases (resulting in better utilization of the fuel) and volumetric efficiency decreases (resulting in reduced amount of oxygen available). Although the absolute values of $NO_X$ are increasing

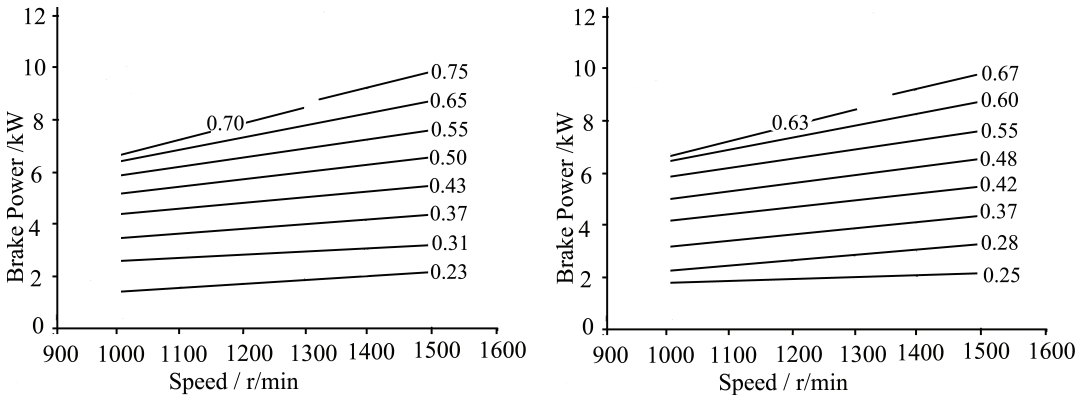


(a) Equivalence Ratio - Diesel (b) Equivalence Ratio - RME

Figure 3.3. Experimentally obtained equivalence ratio maps of diesel (a) and RME (b)

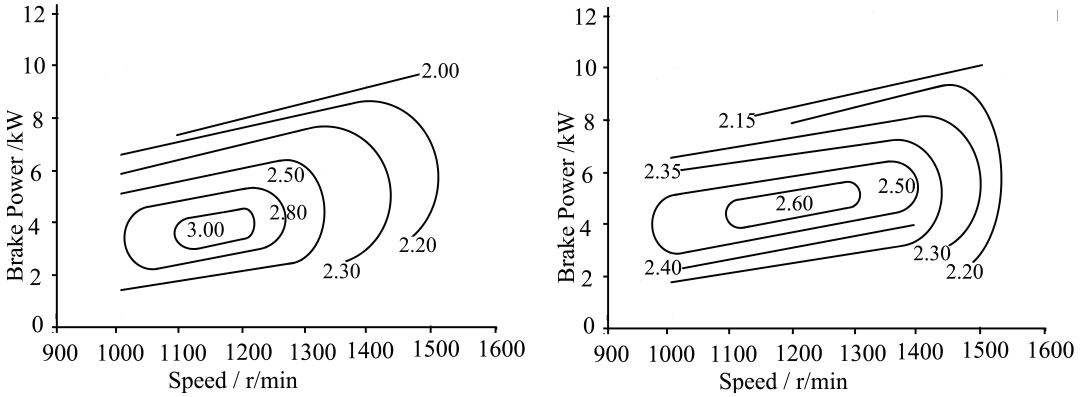


(a) Specific $NO_X$/ g/MJ- Diesel (b) Specific $NO_X$/ g/MJ - RME

Figure 3.4. Experimentally obtained contours of specific $NO_X$ of diesel (a) and RME (b)

with any increase power output, the specific values of $NO_X$ follow the opposite trend at higher power outputs. This can be attributed to reduction in volumetric efficiency and an increase in the brake thermal efficiency at higher powers. These two factors seem to offset higher temperature effects. It can be concluded that at constant speed, the specific $NO_X$ emissions are influenced by the temperature of the in-cylinder mixture. The reduction in specific $NO_X$ emissions with increasing speed may be due to the decrease in residence time of the in-cylinder charge and the cooling effect of incoming air.

For RME fuelling, the trend observed in specific $NO_X$ emissions (figure 3.4(b)) is

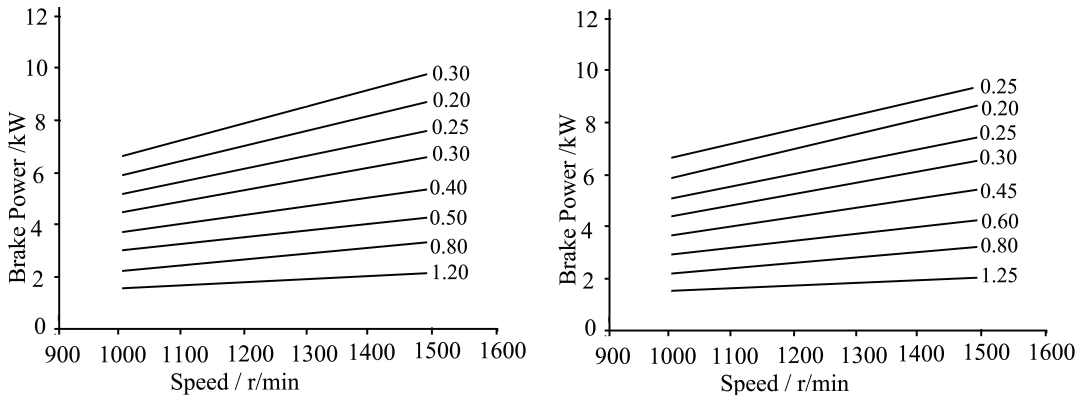


(a) Specific HC - Diesel/ g/MJ (b) Specific HC - RME/ g/MJ

Figure 3.5. Specific HC of Diesel (a) and RME (b)

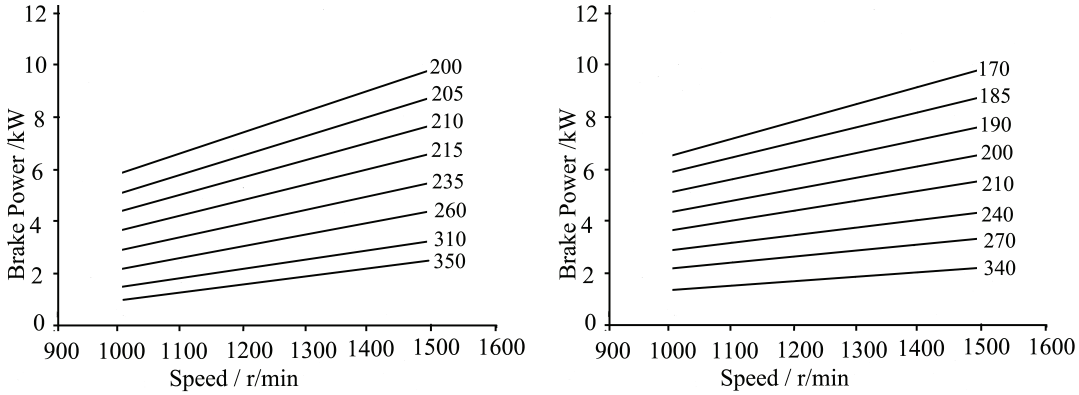


(a) Specific $CO_2$ - Diesel/g/MJ (b) Specific $CO_2$ - RME/g/MJ

Figure 3.6. Experimentally obtained contours of specific $CO_2$ of Diesel (a) and RME (b)

similar to diesel fuelling (figure 3.4(a)). RME has resulted in lower specific $NO_X$ across the whole map. The highest power output at all speeds is the only exception to this trend where RME has resulted in slightly higher $NO_X$. Another difference observed is the range (the difference between the maximum and the minimum ) of the values that is 0.8 g/MJ for diesel 0.35 g/MJ for RME.

The lower specific $NO_X$ values for RME can be attributed to higher cetane number of RME, which leads to a reduced ignition delay, advancing ignition and reducing the premixed phase. Specific $NO_X$ contours for RME are widely spread across different speeds

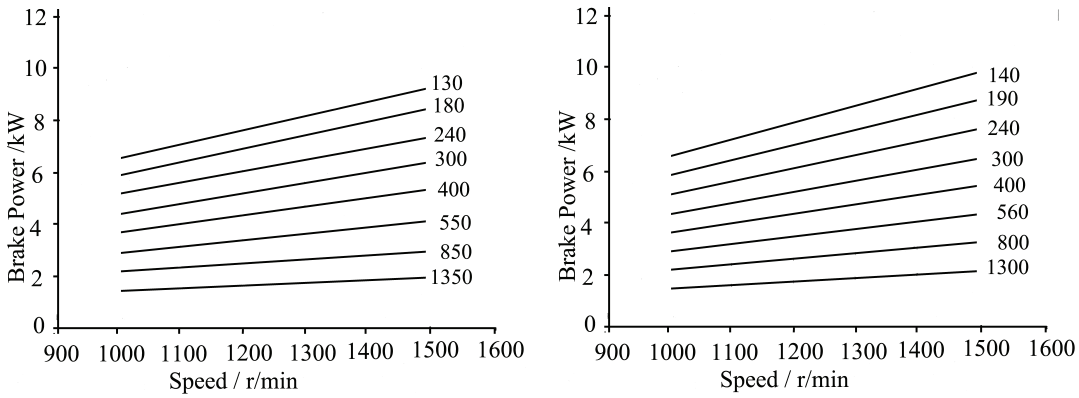


(a) Specific $O_2$ - Diesel/g/MJ (b) Specific $O_2$ - RME/g/MJ

Figure 3.7. Experimentally obtained contours of specific $O_2$ of diesel (a) and RME (b)

when compared to the diesel baseline.

### 3.2.3 Specific HC

Specific HC emissions are at their highest at the lower power outputs for all speeds with both fuels (figures 3.5(a) and 3.5(b)). As the power output increases the specific HC emission decrease to a minimum which then increases slightly for the very highest power output made. At the lower powers, the engine is operating under lean conditions resulting in lower combustion temperatures and a reduction the the brake thermal efficiency (figures. 3.2(a) and 3.2(b)). This has a combined effect of leading to the higher specific HC emissions. As the power increases, combustion is improved as the temperature increases with the engine operating less lean. The slight increase in the specific HC emissions at the highest powers may be attributed to the reduction in brake thermal efficiency, showing the combustion has suffered slightly. This is a result of a portion of the fuel not mixing fully with the air in the cylinder and resulting in slightly poorer fuel combustion. For similar power outputs, higher specific HC emissions are observed at higher engine speeds. Combustion quality is deteriorating with increasing speed. This is supported by the lower specific $NO_X$ emissions at higher speeds. This deterioration may be a consequence of the

combined effect of reduced volumetric efficiency and reduced residence time.

RME fueling compared with diesel has no significant impact on the specific HC emissions (figure 3.5(b)). At lower loads, RME shows slightly higher values of HC emissions. This can be attributed to relatively poor atomization and lower volatility of RME. Higher specific fuel consumption can be another reason for this difference between RME and diesel fuels. Unlike diesel, where HC emissions showed a surge at the highest loads in figure 3.5(a), the HC emissions for RME decreased even at the highest loads in figure 3.5(b). This shows that RME combustion is not affected by the under-mixing phenomenon, and enough oxygen is present to burn the fuel even at the highest loads.

### 3.2.4 Specific $CO_2$

The absolute values for $O_2$ emission decrease and specific $CO_2$ emissions increase as the load is increased. This is because more fuel is being injected at higher loads and the combustion chamber is at higher temperature. Looking at specific $CO_2$ (figure 3.6(a)) and specific $O_2$ (figure 3.7(a)) emission maps, it is evident that the specific values of these emissions decrease as the engine load is increased. This again can be attributed to increase in thermal efficiency and decrease in volumetric efficiency as the engine load is increased. A 90% drop in specific $O_2$ emissions has resulted in 46% drop in specific $CO_2$ emission. This is because both the specific as well as absolute emissions of $O_2$ decrease as the load is increased, whereas for $CO_2$ emissions absolute values increase and specific values decrease as the load is increased.

In terms of absolute numbers higher $CO_2$ emissions are obtained at higher speeds because absolute burning rate increases proportionally as the speed is increased. This increase does not reflect in specific $CO_2$ emission map because this increase in emission is offset by more power produced at higher speeds. Lower $CO_2$ emissions are obtained with RME (figure 3.6(b)) when compared to $CO_2$ values obtained with diesel (figure 3.6(a)) for all ranges of load and speed. This can be due to lower carbon to hydrogen ratio for RME

in comparison to diesel.

## 3.3 CHAPTER SUMMARY

Most studies presenting performance and emissions characteristics of compression-ignition (CI) engines operating with various fuels present these characteristics at a few load settings and engine rotational speed combinations. In general engine performance and emissions contours have not been investigated throughout the operating speed and power range of engines. In this chapter the performance and specific emissions contours of a diesel and RME fueled CI engine are experimentally investigated, assessed, compared, and critically discussed. The contours are plotted on load (brake power) versus engine rotating speed planes over a range of engine operating conditions. The thermal efficiencies of diesel and RME are comparable for all ranges of speeds and power outputs. At the maximum power range RME has slightly higher thermal efficiency. From the location of maximum $NO_X$ contours in the central region of the power-speed range, the specific $NO_X$ decreases in all directions across the whole map. RME produces lower $NO_X$ compared to the diesel fuel. At the higher loads RME produces fewer unburned hydrocarbon emissions than diesel, but at lower and intermediate loads the unburned hydrocarbon emissions are comparable. $CO_2$ is lower with RME than diesel throughout the engine operating range.

# CHAPTER 4

# PERFORMANCE AND EMISSIONS MAPS OF NATURAL GAS IN DUAL FUELING MODE

## 4.1 BACKGROUND AND MOTIVE

Natural gas has long been considered an alternative fuel for the transportation sector and has been used to fuel vehicles since the 1930s. Natural gas is the cleanest fossil fuels available and its proven reserves are 5288.5 trillion cubic feet, much larger than crude oil [101]. Low carbon content and clean burn features (low soot and smoke) have helped the proliferation of natural gas as an alternate fuel with the introduction of ever more stringent emissions standards. Natural gas has properties that are very similar to those of methane ($CH_4$), which is its primary constituent. It also contains heavier hydrocarbons such as ethane ($C_2H_6$), propane ($C_3H_8$), and butane ($C_4H_{10}$), and inert diluents such as molecular nitrogen ($N_2$) and carbon dioxide ($CO_2$) [102, 103, 104, 6].

Natural gas has a low cetane number (high octane number) [6, 101, 104] and high specific heat capacity ratio ($\gamma$). The poor ignition characteristics (extended ignition delay) of low cetane number fuels in CI engines often prevents ignition entirely at the temperatures found under compression in a CI engine. Various ignition strategies are used to ignite natural gas in unmodified CI engines. A glow plug or a high cetane liquid fuel such as diesel [6, 60, 105] or RME [6] have been widely used as an initial source of ignition using the dual fuel concept [106]. The natural gas is most often inducted into the engine in the air intake manifold with the high cetane fuel directly injected into the cylinder. To ensure ignition and sustain acceptable combustion there is a lower limit of the quantity of the high cetane fuel that must be injected [106].

The low cetane number of natural gas affords the opportunity to operate the engine with a higher compression ratio than can be achieved with standard mineral diesel. Higher compression ratio results in greater brake power, improved thermal efficiency [6]

and higher in cylinder temperatures. To take advantage of the low cetane number in this manner requires modification to a standard CI engine to increase compression ratio. This is infrequently done when testing natural gas in CI engines.

The higher specific heat capacity ratio of natural gas lowers in-cylinder charge temperature and increases ignition delay compared to the baseline diesel operation and hence is critical from an emissions perspective [84, 100]. Due to these competing factors dual fueling with natural gas needs to be investigated across a wider range of engine operating conditions to assess the affect of engine speed and load (power output) in addition to the above mentioned factors.

Dual fueling of CI engine with natural gas has demonstrated a slight reduction of brake thermal efficiency when compared to fueling with standard mineral diesel [60, 107, 105, 108, 65] whereas higher thermal efficiency values were reported at higher loads [59]. Concerning total brake specific fuel consumption, it is revealed that it becomes inferior under dual fuel operation compared to normal diesel operation at the same engine operating conditions because of the lower heating value of natural gas. At high load, the values of total brake specific fuel consumption under dual fuel operation tend to converge with that of normal diesel operation [60].

$NO_X$ is strongly dependent on local temperatures so most $NO_X$ is expected to form in the region around the pilot spray where high temperatures exist and the equivalence ratio is close to stoichiometric [109]. Earlier and faster combustion events increase the duration for which in-cylinder conditions are suitable for $NO_X$ formation[110]. The use of natural gas under dual fueling in CI engines has a positive effect on $NO_X$ emissions: the $NO_X$ concentration under dual fuel operation is lower when compared to normal diesel operation. At the same time, a significant decrease in soot emissions under dual fuel operation has also been reported [102]. On the other hand, CO and HC emissions levels have been reported to be considerably higher when compared to normal diesel operation [60, 84, 100, 107, 111].

Whereas literature has been reported on natural gas combustion and emissions under dual fueling conditions in CI engines, most of the studies lack one or the other important aspects. The studies are either restricted to various loads/powers at one engine speed (neglecting the effect of engine speed) or one or two load/power conditions at various speeds (neglecting load variations). There is a scarcity of engine "fuel maps" in the open literature (these are the full contours of thermal efficiency or brake specific fuel consumption plotted throughout the power versus speed range of the engine, or the torque versus speed range of the engine). Sample fuel maps can be found in [1, 10, 99]. One such plot of thermal efficiency contours with dual-fueling has been presented previously to demonstrate the thermal efficiency within the operating range of the test engine used in this chapter [100]. Maps showing the thermal efficiency as well as specific emissions contours on the power-speed planes are seldom found in the open literature [107].

The choice of pilot fuel has also been limited to either diesel or biodiesel only and the performance of these two pilots has hardly been investigated and compared over a wider range of operating conditions in compression ignition environment. The study presented here is an effort to fill these gaps in the literature available on natural gas based dual fueling in CI engines.

In research papers laboratory experiments of engine performance and emissions are usually conducted at constant equivalence ratio, or constant brake mean effective pressure, or occasionally at constant speed. All of these representations are of some use to the average consumer, but they do little to represent or explain the overall thermal efficiency and emissions characteristics of engines throughout their operating range.

In the work presented in this chapter both speed and power are considered for diesel and RME piloted natural gas combustion in a direct injection CI engine. The results are presented as iso-contours of thermal efficiency, volumetric efficiency and brake specific emissions on a power-speed graph throughout the operating range of the engine. This is a novel approach to representing these data, especially for CI engines. As one example of

the utility of the considerations presented in this paper, the the specific $NO_X$ emissions contours presented later illustrate that for the baseline single-fuel diesel configuration the region of high specific $NO_X$ emissions is at intermediate engine speed and power, dropping off at high and low values of engine speed and power, helping to explain the $NO_X$ emission trends presented elsewhere in the literature; while the dual-fueling specific $NO_X$ emissions contours show monotonically increasing trends with increasing engine load and increasing engine speed.

## 4.2 RESULTS AND DISCUSSION - DIESEL PILOTED NATURAL GAS

This section presents thermal efficiency, volumetric efficiency, specific $NO_X$, specific HC and specific $CO_2$ maps for diesel piloted dual fueling of natural gas and compares them against the maps obtained with diesel based single fueling. As there were lrge number of data points used to generate these maps, the in-cylinder pressure and the rate of energy release data have not been presented here. The in-cylinder pressure and the rate of energy release for pure diesel and RME as well as diesel and RME piloted natural gas on selected points (one lower load and one higher load) have been presented in appendix A.

### 4.2.1 Thermal Efficiency and Volumetric Efficiency

Figure 4.1(a) presents an experimentally obtained map showing iso-contours of thermal efficiency for diesel based single fueling whereas figure 4.1(b) presents a similar map for diesel piloted dual fueling of natural gas. While operating in dual fuel mode using diesel-ignited natural gas

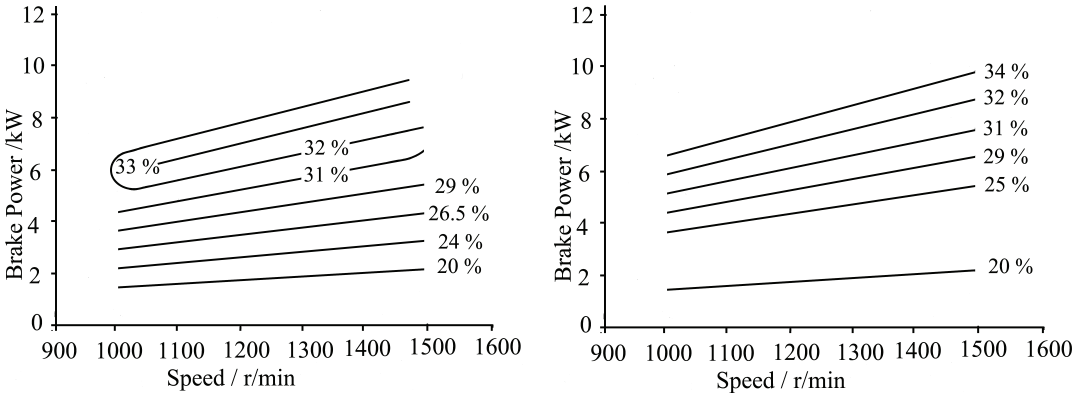


(a) Thermal Efficiency - Diesel (b) Thermal Efficiency - Diesel Plus NG

Figure 4.1. Experimentally obtained thermal efficiency contours of diesel single fueling (a) and diesel piloted natural gas dual fueling (b)

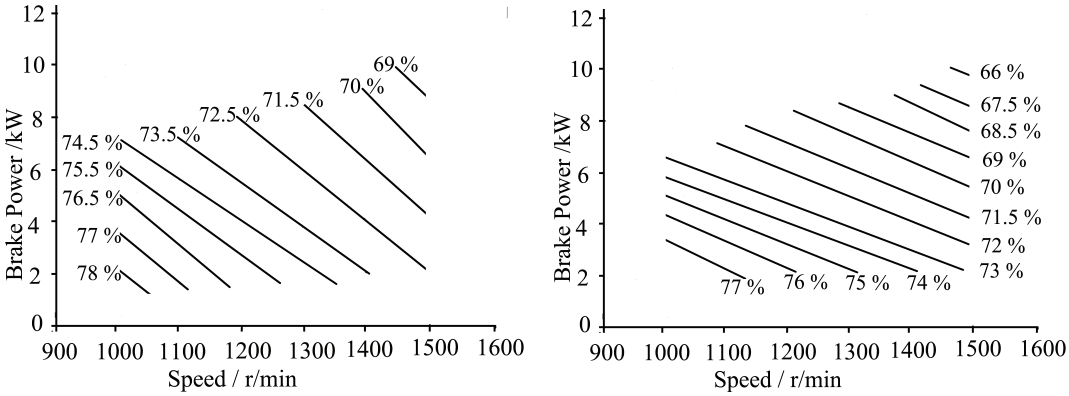


(a) Volumetric Efficiency - Diesel (b) Volumetric Efficiency - Diesel Plus NG

Figure 4.2. Experimentally obtained volumetric efficiency contours of diesel single fueling (a) and diesel piloted natural gas dual fueling (b)

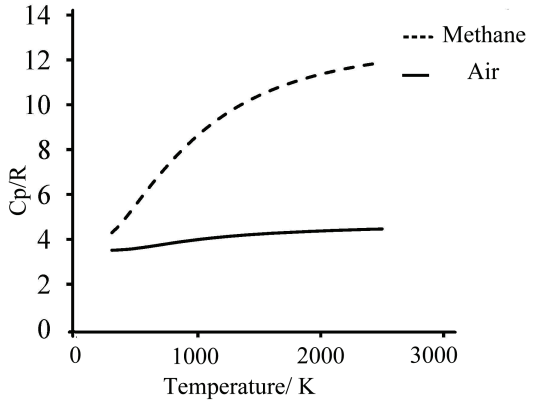


Figure 4.3. Specific heat at constant pressure, $C_P/R$ as a function of temperature for air and methane

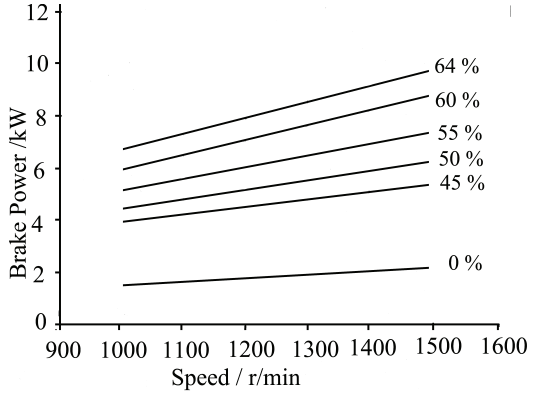


Figure 4.4. Enthalpy fraction of natural gas during diesel piloted natural gas dual fueling.

no significant difference (overall) is observed in thermal efficiency when compared to pure diesel operation. At higher power outputs, dual fuel mode produces similar or higher thermal efficiencies as compared to normal fueling mode whereas at relatively lower power outputs, lower values of thermal efficiency have been observed (figure 4.1(b)).

The lower thermal efficiency values at lower power outputs may be attributed to the failure of pilot fuel to ignite and sustain adequate combustion of the natural gas-air mixture. As demonstrated in appendix A, at lower and medium loads, diesel piloted dual fueling of natural gas produces lower pressure when compared to diesel based single fueling. Whilst the local equivalence ratio in the region of the pilot injection may be near unity (stoichiometric), especially during the initial pre-mixed combustion phase, the overall F/A

ratio is 0.25% lower than single diesel fueling at the lower power output. This suggests that the portion of the combustion chamber not in the pilot region contains a lean homogenous mixture of natural gas and air. At the highest power outputs the dual fuel mode exhibits a F/A ratio 3.73% higher than that of single diesel fueling. Under these conditions the pilot fuel is igniting a richer homogenous mixture resulting in a 3.1% (approximately) increase in thermal efficiency. As demonstrated in appendix A, at higher loads, natural gas dual fueling exhibit comparable peak cylinder pressure and higher rate of energy release peak when compared to the respective pilot fuel. As the power output increases the dual fuel mode recovers the thermal efficiency losses suffered at the lower power outputs with both modes of operation having similar F/A ratios.

Figure 4.2(a) presents an experimentally obtained map showing volumetric efficiency trends on a speed-power graph for diesel based single fueling whereas figure 4.2(b) presents a similar map for diesel piloted dual fueling of natural gas. The volumetric efficiency map (figure 4.2(b)) reflects the lower values for dual fuel mode. This is to be expected as a portion of the inducted air is being displaced by the natural gas in the intake, reducing the air partial pressure below that of the mixture pressure. Also as to be expected is the drop of volumetric efficiency as the engine speed increases for both modes of operation (figures 4.2(a) and 4.2(b)). The frictional losses are known to increase as the square of engine speed [10] . The slope of the volumetric efficiency contours is flatter for natural gas dual fueling with diesel than for baseline diesel operation and the values are lower. This is a consequence of the method used to introduce natural gas into the engine. As the natural gas has been introduced via manifold injection, a portion of the intake air is displaced by the natural gas, reducing the measured volume flow rate of air into the engine. This leads to a reduction of the engine's volumetric flow rate. The slope of the iso-contours differs due to a change in the scaling of volumetric efficiency with engine speed. As the amount of natural gas added is increased to meet the increase in speed demand, larger amounts of air are displaced. As the natural gas is introduced at the manifold and does not flow through

the entire intake system but the air does, the scaling law as noted by Heywood [10] does not hold.

### 4.2.2 Specific $NO_X$

Figure 4.5(a) presents an experimentally obtained map showing iso-contours of specific $NO_X$ for diesel based single fueling whereas figure 4.5(b) presents a similar map for diesel piloted dual fueling of natural gas. Significant reduction in $NO_X$ is noted with diesel

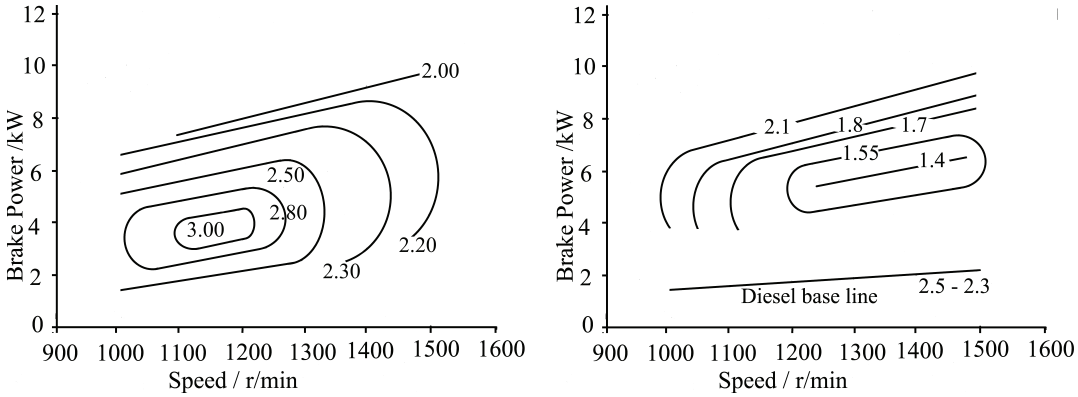


(a) Specific $NO_X$ /g/MJ - Diesel (b) Specific $NO_X$/ g/MJ - Diesel Plus NG

Figure 4.5. Experimentally obtained specific $NO_X$ contours for diesel single fueling (a)and diesel piloted natural gas dual fueling (b).

piloted natural gas dual fueling compared to diesel single fueling. The composition of the in-cylinder mixture prior to combustion in case of dual fueling is different from that during diesel single fueling. In case of single fueling the major constituent of the in-cylinder mixture during compression stroke is air along with a fraction of the residual gases from the previous combustion event. Whereas in case of dual fueling, the mixture during compression stroke is composed of a homogeneous mixture of air , natural gas and residual gases. Figure 4.3 shows the variation of the specific heat at constant pressure with temperature for air and methane ( main constituent of natural gas) and figure 4.4 shows enthalpy contribution of natural gas at different operating conditions.

The specific heat capacity ratio of natural gas is significantly higher than for air.

An overall increase in the heat capacity of the in-cylinder mixture as is the case for dual fueling results in a reduced average temperature at the end of the compression stroke. This will lead to an overall lower combustion temperature. With the formation of $NO_X$ highly dependent on the thermal mechanism, the reduced temperature leads to a level of reduced $NO_X$. As the combustion of the homogenous mixture propagates from a number of multi-site ignitions, the increased specific heat capacity will lead to a further reduction of combustion temperature. Reduction in specific $NO_X$ is more significant at lower power where this reduction ranges between 40%-53%. At lower powers, the engine is running relatively cooler compared to at higher powers and hence the higher heat capacity has a more pronounced effect on specific $NO_X$.

As is to be expected, as the power output is increased at a constant speed, the absolute $NO_X$ emissions increase due to the increasing in-cylinder temperatures, however figures 4.5(a)and 4.5(b) show specific $NO_X$ emissions across the engine's operational range. For diesel single fueling, as the power output increases the $NO_X$ levels do not increase at the same rate, hence the specific $NO_X$ at the higher powers is actually lower. The peak specific $NO_X$ emissions are centered around low power and low speed conditions. In terms of $NO_X$ emissions, this region is where the engine's combustion temperature and power relationship is at its worst.

### 4.2.3 Specific HC

Figure 4.6(a) presents an experimentally obtained map showing lines of constant specific HC for diesel based single fueling whereas figure 4.6(b) presents a similar map for diesel piloted dual fueling of natural gas. There is a significant increase in the specific HC emissions at lower and medium power outputs for diesel piloted natural gas dual fueling (figure 4.6(b)) compared to diesel single fueling (figure 4.6(a)). The HC emission iso-contour map reflects that a significant amount of unburnt natural gas is going into the engine exhaust. One possible explanation for this inefficient burning may be poor flame

propagation throughout the homogeneous natural gas-air mixture.

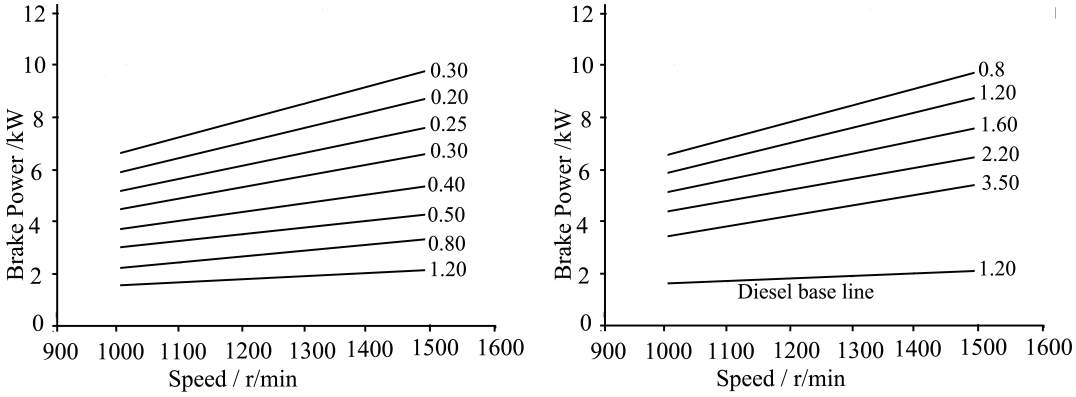


(a) Specific HC /g/MJ- Diesel

(b) Specific HC/ g/MJ - Diesel Plus NG

Figure 4.6. Experimentally obtained specific HC contours for diesel single fueling (a) and diesel piloted natural gas dual fueliing (b)

The equivalence ratio ($\phi$) threshold for dual fuel modes is 0.4. Below this threshold value, the HC emissions increase whereas increasing $\phi$ beyond this value results in a decrease in HC emissions. The equivalence ratio in this case ranges between 0.44 and 0.79 and this is reflected in gradual decrease of HC emissions as the load increases. When natural gas contributes approximately 45% of the total enthalpy (figure 4.4) the specific HC emissions increase by about 800%. As the load is increased, the difference between the two modes (single and dual fuel modes) in terms of specific HC emissions is narrowed down. At maximum load conditions when natural gas enthalpy fraction is more than 60%, the dual fuel case produces 250% more specific HC emissions when compared to the diesel single fueling which reflects a percentage decrease of about 20% when compared to the case when natural gas contributed about 45% of the total enthalpy required. These higher HC numbers in dual fueling case can again be attributed to deteriorated combustion (especially in the pre-mixed phase) due to low temperature of the in-cylinder mixture as explained in the $NO_X$ section.

### 4.2.4 Specific $CO_2$

Figure 4.7(a) presents an experimentally obtained map showing lines of constant specific $CO_2$ for diesel based single fueling whereas figure 4.7(b) presents a similar map for diesel piloted dual fueling of natural gas. Diesel piloted natural gas dual fueling produces less $CO_2$ emissions. $CO_2$ emissions decreases by 23-30% when diesel is substituted by diesel

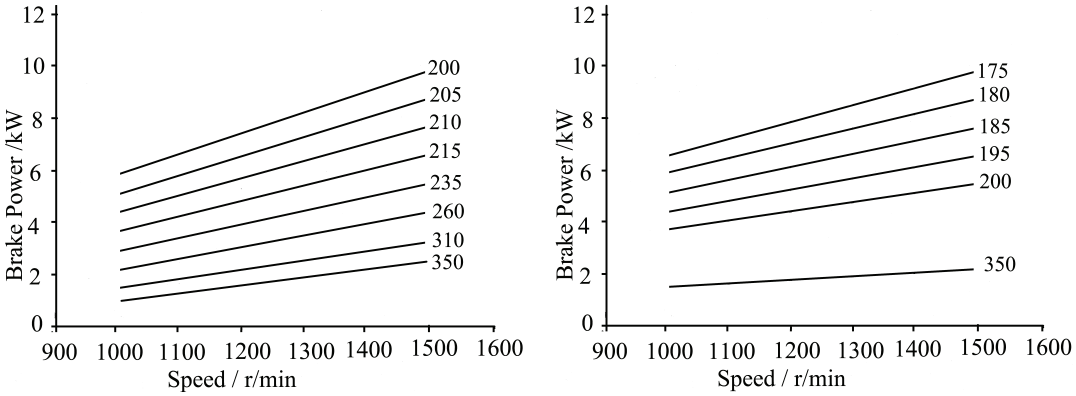


(a) Specific $CO_2$ /g/MJ - Diesel (b) Specific $CO_2$ /g/MJ - Diesel Plus NG

Figure 4.7. Experimentally obtained specific $CO_2$ contours for diesel single fueling (a)and diesel piloted natural gas dual fueling (b)

plus natural gas dual fuel. This decrease in $CO_2$ can be attributed to lower carbon to hydrogen ratio in case of dual fueling. Stoichiometrically, one gram of methane produces 2.0 g of $CO_2$ as compared to 3.2 g produced by 1.0 g of diesel (37.5% difference)

## 4.3 RESULTS AND DISCUSSION - RME PILOTED NATURAL GAS

This section presents thermal efficiency, volumetric efficiency,specific $NO_X$, specific HC and specific $CO_2$ maps for RME piloted dual fueling of natural gas and compares them against the maps obtained with diesel based single fueling.

### 4.3.1 Thermal Efficiency and Volumetric Efficiency

Enthalpy contribution of natural gas in an RME piloted dual fueling of the natural gas across different operating conditions has been shown in figure 4.8. It ranges between 48% at

relatively lower loads to and 65% at the highest loads across different speeds. Figure 4.9(a) presents an experimentally obtained map showing iso-contours of thermal efficiency for RME based single fueling whereas figure 4.9(b) presents a similar map for RME piloted dual fueling of natural gas. RME piloted dual fueling exhibits slightly inferior thermal efficiency at lower and medium loads when compared to the single fueling case (figure 4.9(b)). When compared to RME based single fueling operation (figure 4.9(a)), the RME piloted dual fueling of natural gas shows a decrease of 13%, 5% and 1.5% in thermal efficiency when the enthalpy fraction (figure 4.8) of natural gas was 48%, 53% and 58% respectively. No

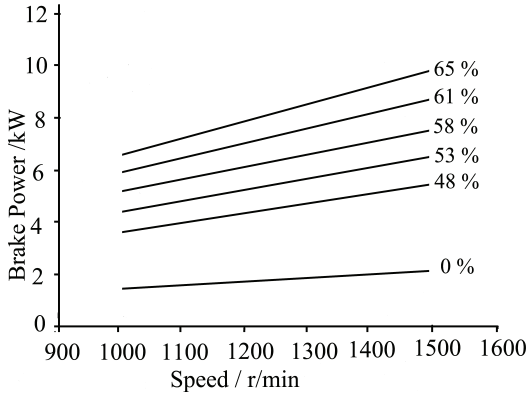


Figure 4.8. Enthalpy fraction of natural gas during RME piloted natural gas dual fueling.

significant difference in thermal efficiency is observed when the natural gas enthalpy fraction was 60% or above. As discussed in section 4.2.1, this is believed to be an effect of the pilot fuel failing to ignite and sustain acceptable combustion in the overall lean homogeneous mixture of natural gas and air. As with the diesel piloted dual fueling, this argument is supported by the HC emissions for dual fueling (figure 4.6(b)) which decrease significantly with increasing power output.

Figure 4.10(a) presents an experimentally obtained map showing lines of constant constant volumetric efficiency for RME based single fueling whereas figure 4.10(b) presents a similar map for RME piloted dual fueling of natural gas. The volumetric efficiency map (figure 4.10(b)) reflects the lower values for dual fuel mode. As with the case for diesel

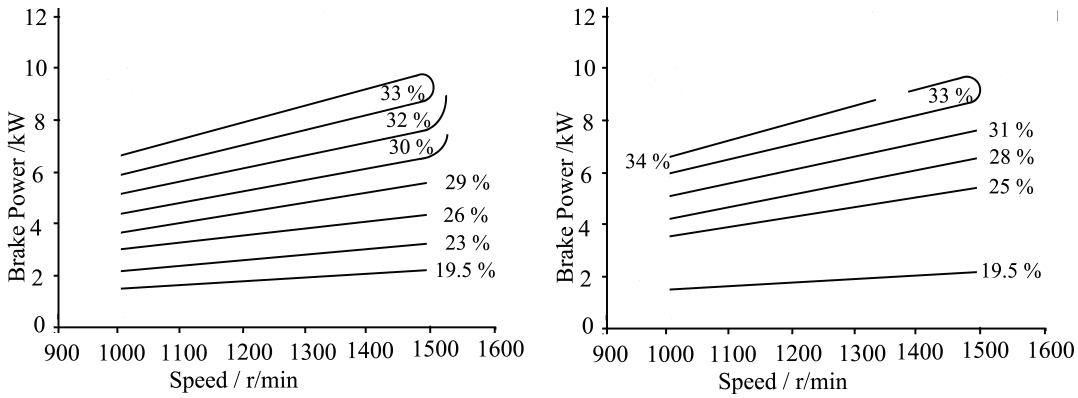


(a) Thermal Efficiency - RME

(b) Thermal Efficiency - RME Plus NG

Figure 4.9. Experimentally obtained thermal efficiency contours of RME single fueling (a) and RME piloted natural gas dual fueling (b)

piloted dual fueling as discussed in section 4.2.1 this trend is to be expected as a portion of the inducted air is being displaced by the natural gas in the intake. The value and slope of the constant volumetric efficiency lines for RME piloted dual fuel mode (figure 4.10(b)) differ slightly from those for diesel piloted dual fuel mode (figure 4.2(b)). This can be attributed to the slightly lower heating value of RME compared to diesel. This leads to a larger portion of the total enthalpy in the cylinder coming from the natural gas, meaning a larger portion of the intake air is displaced by the natural gas.

### 4.3.2 Specific $NO_X$

Figure 4.11(a) presents an experimentally obtained map showing iso-contours of specific $NO_X$ for RME based single fueling whereas figure 4.11(b) presents a similar map for RME piloted dual fueling of natural gas. When compared to RME based single fueling, the RME based dual fueling results in overall lower specific $NO_X$. This observation holds very good for all range of speed and load combinations.

Quantitatively, the difference between specific $NO_X$ is the lowest at the the junction of higher loads and medium speeds where it is approximately 7%. At medium loads and medium speeds, the specific $NO_X$ in dual fueling mode are reduced by approximately 40%.

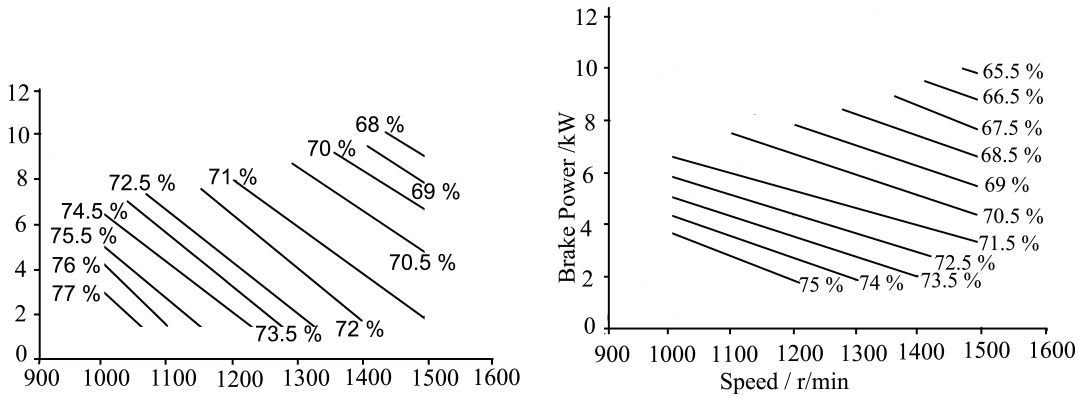


(a) Volumetric Efficiency - RME (b) Volumetric Efficiency - RME Plus NG

Figure 4.10. Experimentally obtained volumetric efficiency contours of RME single fueling (a) and RME piloted natural gas dual fueling (b)

At higher speeds for all range of load, the specific $NO_X$ reduction ranges between 40-43%. Another interesting observation is the variation in location of the maximum specific $NO_X$. While operating in single fuel mode, the maximum specific $NO_X$ are approximately concentrated at the junction of medium loads and medium speeds. This holds good both for diesel (figure 4.5(a)) as well as RME (figure 4.11(a)). Moving outwards from the position of maximum $NO_X$ results in gradual decrease in specific $NO_X$ numbers. On the other hand, the specific $NO_X$ contours for the two dual fueling cases reflect an opposite trend. Medium load and medium speed combination carries the lowest specific $NO_X$ and a gradual increase in specific $NO_X$ is observed on all outward contours. The only exception to this trend are the specific $NO_X$ contours at higher speeds. The specific $NO_X$ maps both for diesel (figure 4.5(b)) and RME (figure 4.11(b)) piloted dual fueling case reflect that the latter produces slightly higher specific $NO_X$ as compared to the former. This difference in specific $NO_X$ numbers for the two dual fueling cases can be explained by relatively higher absolute $NO_X$ numbers in case of RME and a slight variation in thermal efficiency (figures 4.1(b) and 4.9(b)).

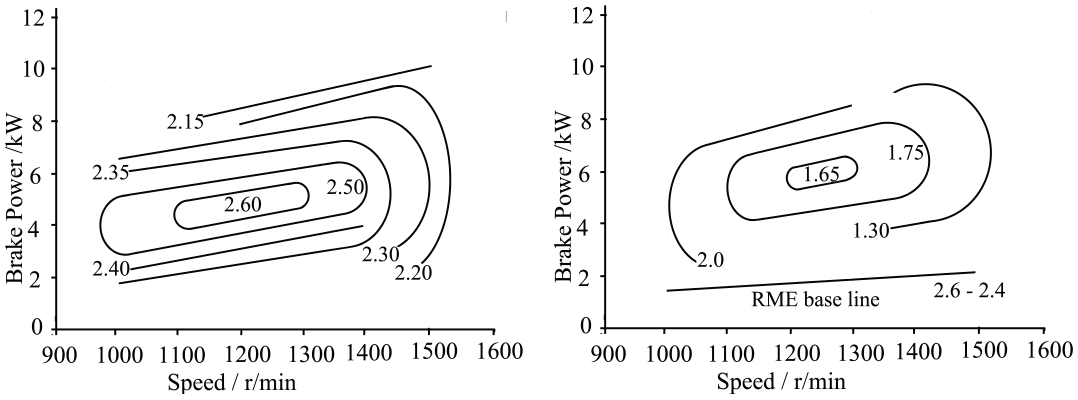


(a) Specific $NO_X$ /g/MJ - RME (b) Specific $NO_X$ /g/MJ - RME Plus NG

Figure 4.11. Experimentally obtained specific $NO_X$ contours for RME single fueling (a) and RME piloted natural gas dual fueling (b)

### 4.3.3 Specific HC

Figure 4.12(a) presents an experimentally obtained map showing lines of constant specific HC for RME based single fueling whereas figure 4.12(b) presents a similar map for RME piloted dual fueling of natural gas.

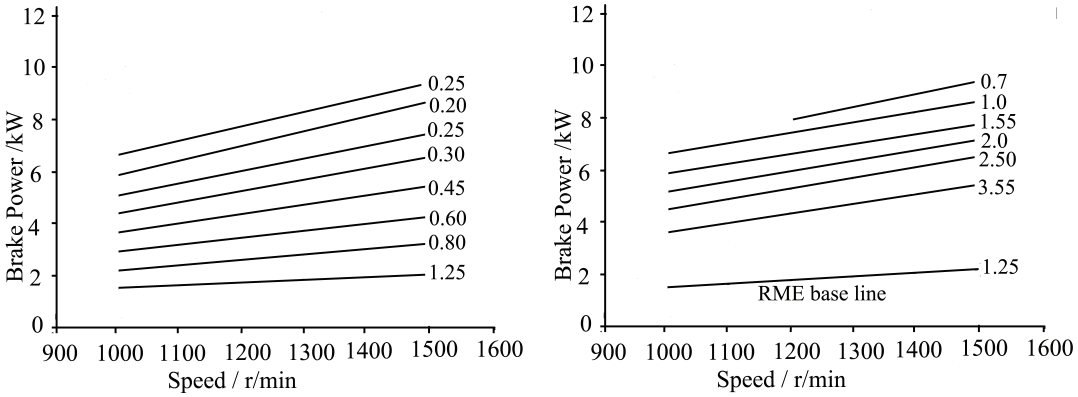


(a) Specific HC /g/MJ - RME (b) Specific HC /g/MJ- RME Plus NG

Figure 4.12. Experimentally obtained specific HC contours for RME single fueling (a) and RME piloted natural gas dual fueling (b)

When compared to RME based single fueling case, the RME piloted combustion of natural gas results in higher specific HC emissions. So far as the comparison of these two modes involving RME is concerned, the explanation put forward in specific HC section

(section 4.2.3) of diesel piloted combustion of natural gas holds for RME piloted combustion of natural gas as well. When the two dual fueling cases are concerned, there is no significant difference in HC values when RME substitutes diesel as pilot fuel for natural gas combustion in CI engines. When compared to the diesel piloted dual fueling of natural gas (figure 4.12(a)), a slight reduction in HC values at higher loads when RME pilots the natural gas combustion can be attributed to higher equivalence ratio at these conditions. This higher equivalence ratio is caused by extra in-fuel oxygen in case of RME. At lower and medium loads, RME led combustion of natural gas has resulted in higher specific HC emissions. This may attributed to the argument proposed in section 4.2.1 with the pilot fuel unable to ignite and sustain acceptable combustion in an overall lean mixture in the cylinder.

### 4.3.4 Specific $CO_2$

Figure 4.13(a) presents an experimentally obtained map showing lines of constant specific $CO_2$ for RME based single fueling whereas figure 4.13(b) presents a similar map for RME piloted dual fueling of natural gas. As with the diesel piloted dual fueling natural

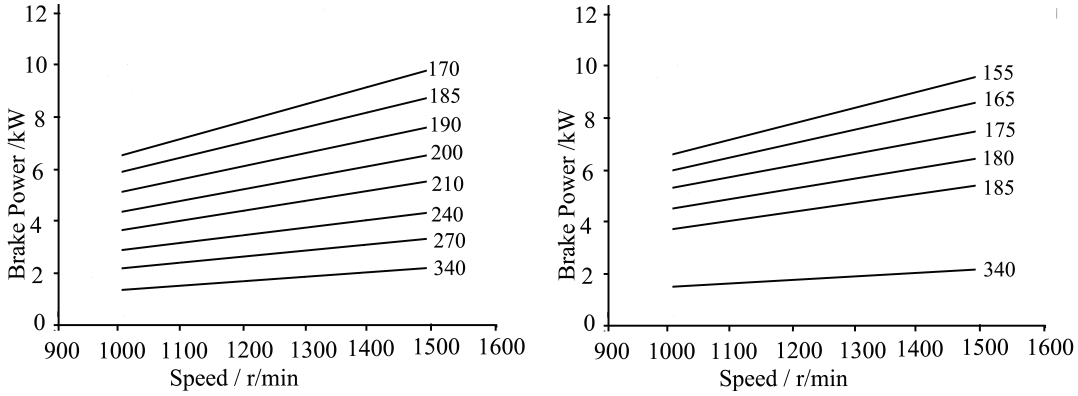


(a) Specific $CO_2$ /g/MJ - RME (b) Specific $CO_2$ /g/MJ - RME Plus NG

Figure 4.13. Experimentally obtained specific $CO_2$ contours for RME single fueling (a) and RME piloted natural gas dual fueling (b)

gas (figure 4.13(b)), RME piloted dual fueling results in lower specific $CO_2$ emissions (fig-

ure 4.13(b)) compared to the RME based single fueling (figure 4.13(b)). The difference can attributed be to the reduction in carbon going into the engine in case of dual fueling with natural gas. The data used to plot these maps has been used to tabulate the performance comparison of the two pilot fuels in table 4.1

Table 4.1. Performance comparison of Diesel and RME as pilot fuels in natural gas combustion

| Pilot Fuel | Natural Gas Enthalpy Fraction | Thermal Efficiency %ge change | Specific HC %ge change | Specific $CO_2$ %ge change |
|---|---|---|---|---|
| Diesel | 45% | 13.79%↓ | 875%↑ | 17.5%↓ |
| | 50% | 6.45%↓ | 730%↑ | 9.3%↓ |
| | 55% | 3.22%↓ | 635%↑ | 11.9%↓ |
| | 60% | 3.03%↓ | 600%↑ | 12.2%↓ |
| | 64% | 6.25%↑ | 266%↑ | 12.5%↓ |
| RME | 48% | 13.79%↓ | 788%↑ | 11.90%↓ |
| | 53% | 6.66%↓ | 830%↑ | 10%↓ |
| | 58% | 3.22%↓ | 800%↑ | 7.89%↓ |
| | 61% | 0%↓ | 500-775%↑ | 10.81%↓ |
| | 65% | 0 - 3.03%↑ | 280-400%↑ | 8.82%↓ |

## 4.4 CHAPTER SUMMARY

When natural gas is port/manifold injected into a compression ignition engine, the mixture of air and the natural gas is compressed during the compression stroke of the engine. Due to the difference in the values of specific heat capacity ratio between air and natural gas, the temperature and pressure at the time of pilot fuel injection are different

when compared to a case where only air is compressed. This significantly affects the performance as well as emissions characteristics of natural gas based dual fuelling in CI engine. Natural gas has been extensively tested in a single cylinder compression ignition engine to obtain performance and emissions maps. Two pilot fuels, diesel and RME, have been used to ignite natural gas. The performance of the two liquid fuels used as pilots has also been assessed and compared. Tests were conducted at 48 different operating conditions (six different speeds and eight different power output conditions for each speed) for single fueling cases. Both the diesel and RME based single fuelling cases were used as baselines to compare the natural gas based dual fuelling where data was collected at 36 operating conditions (six different speeds and six different power output conditions for each speed). Performance and emissions characteristics were maped on speed vs brake power planes. The thermal efficiency values of the natural gas dual fueling were lower when compared to the respective pilot fuel based single fueling apart from the highest powers. The effect of engine speed on volumetric efficiency in case of the natural gas based dual fueling was significantly different from what was observed with the single fueling. Contours of specific $NO_X$ for diesel and RME based single fueling differ significantly when these fuels were used to pilot natural gas combustion. For both of the single fueling cases, maximum specific $NO_X$ were centered at the intersection of medium speeds and medium powers and they decrease in all directions from this region of maximum values. On the other hand, an opposite trend was observed with dual fueling cases where minimum specific $NO_X$ were observed at the center of the map and they increase in all direction from this region of minimum $NO_X$. RME piloted specific $NO_X$ at the highest speeds were the only exception to this trend. Higher specific HC and lower specific $CO_2$ emissions were observed in case of natural gas based dual fueling.

# CHAPTER 5

# PERFORMANCE AND EMISSIONS MAPS OF HYDROGEN IN DUAL FUELING MODE

## 5.1 BACKGROUND AND MOTIVE

There is increasing interest in the use of alternative, clean-burning fuels in order to reduce the dependence on non-sustainable fossil-derived fuels and meet ever stricter emissions targets. Amongst the numerous alternatives proposed, hydrogen has received particular interest due to its superior combustion characteristics [112]. Approximately 95% of the hydrogen currently produced is by steam reforming of natural gas (a catalytic thermochemical conversion process). Renewable hydrogen-production methods, such as electrolysis of water using renewably generated electricity, pyrolysis, photo-biological water splitting, photo-electro-chemical water splitting and solar thermo-chemical water splitting are techniques yet to be fully realized [113] but make hydrogen a viable alternative to fossil derived fuels, or as a substitute fuel for at least a portion of the overall energy supplied to these engines, e.g. in dual fuel mode operation [114, 6]

Hydrogen's high autoignition temperature makes it difficult to ignite a hydrogen/air mixture on the basis of mixture temperature alone without some additional ignition source. In SI engines this is achieved by the spark. In CI engines a small amount of high cetane liquid fuel is injected into the chamber during the compression stroke at the desired point of ignition. This mode of operation in CI engines is referred to as dual fueling [114, 6]. Studies have been conducted with diesel piloted hydrogen combustion [115] and biodiesel piloted hydrogen [116, 114, 117]. Comparison between these two pilots has been made [100] but at a very limited range of engine operating conditions.

Hydrogen has a high burning velocity which leads to increased in-cylinder pressures and higher temperatures, resulting in increased $NO_X$ emissions. This effect may be reduced by making the mixture leaner using hydrogen's property to be flammable over a very wide

range of concentrations in air (from 4% to 75%) [116, 118, 115]. This allows for the application of learner combustion, resulting in a reduction of temperature and pressure, and lower $NO_X$ emissions [119]. However, the initiation and development of the multiple turbulent flames requires a $H_2$-air mixture richer than the lean flammability limit [120]. Most studies have limited the enthalpy fraction of hydrogen addition to a maximum of 15% [116, 108]. The upper limit of hydrogen addition with manifold injected hydrogen is determined by the quenching gap of hydrogen flame which can travel past the nearly-closed intake valve and more readily backfires into the engine's intake manifold [121]. There is a need to examine the performance and emissions of a naturally aspirated CI hydrogen dual fueled engine at higher hydrogen enthalpy fractions. The maximum enthalpy fraction in this study is 30%.

Hydrogen has been shown to increase flame stability [108] and improve thermal efficiency [79]. It is believed that the high diffusion coefficient of hydrogen leads to highly turbulent flame propagation rate [108]. The addition of hydrogen to increase the flame stability has been studied extensively because of the belief that flame propagation is the key factor in improving combustion [108, 122, 119, 123, 96]. Engine speed is often neglected in these studies, but it is clearly one of the key factors in mixing, flame propagation and the residence time. Increased engine speed enhances turbulence and hence affects mixing and flame propagation characteristics. On the other hand the residence time is reduced, therefore the overall effect of hydrogen addition on combustion should be examined with changing speeds. Measurement of $NO_X$ emissions offers an indirect indication of combustion temperatures. The effect of hydrogen addition on combustion and hence the thermal efficiency with varying amounts of hydrogen has been studied previously [116, 120, 117] but often limited to one engine speed and a small range of loads.

A number of studies have examined different emissions of hydrogen in dual fueled CI engines. Some of these studies have considered engine operation at one speed only [116, 120, 79, 73, 124, 78]; others have considered two speeds only [125, 114]. The general

trend exhibited in these studies is an increase in $NO_X$ emissions and a decrease in HC, CO and $CO_2$ when compared to single fueling with their respective pilot fuels. The increase in $NO_X$ emissions with increasing hydrogen addition are attributed to increased flame temperature, and the reductions in HC, CO and $CO_2$ emissions are attributed to the reduction in the carbon content of the fuel. The range of applied loads in these studies is one [125, 73], two [114, 120] three [116], four [79] and five [78].

There is a scarcity of engine "fuel maps" in the open literature (these are the full contours of thermal efficiency or brake specific fuel consumption plotted throughout the power versus speed range of the engine, or the torque versus speed range of the engine). Sample fuel maps can be found in [99, 1, 10]. One such plot of thermal efficiency contours with dual-fueling has been presented previously to demonstrate the thermal efficiency within the operating range of the test engine used in this chapter [100]. Contours showing the thermal efficiency as well as specific emissions contours on the power-speed plane are not easily found in the open literature.

In research papers laboratory experiments of engine performance and emissions are usually conducted at constant equivalence ratio, or constant brake mean effective pressure, or occasionally at constant speed. All of these representations are of some use to the average consumer, but they do little to represent or explain the overall thermal efficiency and emissions characteristics of engines throughout their operating range.

In the current global situation where thermal efficiency and the effect of emissions on the environment are so prominent in the public and scientific media, it seems very strange (and it is misguided) that there is little attention paid to these efficiency and emissions trends throughout the operating range of engines.

In the work presented in this chapter both speed and power are considered for diesel and RME piloted hydrogen combustion in a direct injection CI engine. The results are presented as contours of thermal efficiency, volumetric efficiency and brake specific emissions on a power-speed plane throughout the operating range of the engine. This is a

novel approach to representing these data, especially for CI engines. As one example of the utility of the considerations presented in this paper, the the specific $NO_X$ emissions contours presented later illustrate that for the baseline single-fuel diesel configuration the region of high specific $NO_X$ emissions is at intermediate engine speed and power, dropping off at high and low values of engine speed and power, helping to explain the $NO_X$ emission trends presented elsewhere in the literature; while the dual-fueling specific $NO_X$ emissions contours show monotonically increasing trends with increasing engine load and increasing engine speed.

The next section has divided into two parts. Diesel piloted dual fueling of hydrogen has been discussed in the first part whereas the second part focuses on RME piloted dual fueling of hydrogen.

## 5.2 RESULTS AND DISCUSSION - DIESEL PILOTED $H_2$

This section presents thermal efficiency, volumetric efficiency,specific $NO_X$, specific HC and specific $CO_2$ maps for diesel piloted dual fueling of hydrogen and compares them against the maps obtained with diesel based single fueling. As there were large number of data points used to generate, the in-cylinder pressure and the rate of energy release data have not been presented here. The in-cylinder pressure as well as the rate of energy release data for pure diesel and RME under single fueling whereas for diesel and RME piloted dual fueling cases of hydrogen have been presented in appendix A.

### 5.2.1 Thermal Efficiency and Volumetric efficiency

Figure 5.1(a) illustrates the thermal efficiency contours for the engine operating under normal CI conditions when fueled with diesel. The contours show that at any operating engine speed the engine's thermal efficiency increases with increasing power output except at the highest power levels, where a small reduction in thermal efficiency is observed.

This contour plot is a good example of the advantage of expressing engine data in this

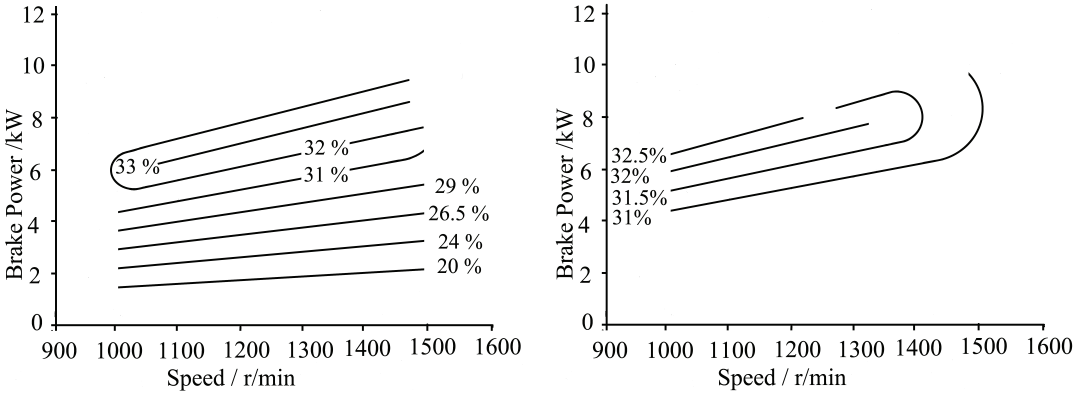


(a) Thermal Efficiency - Diesel

(b) Thermal Efficiency - Diesel Plus $H_2$

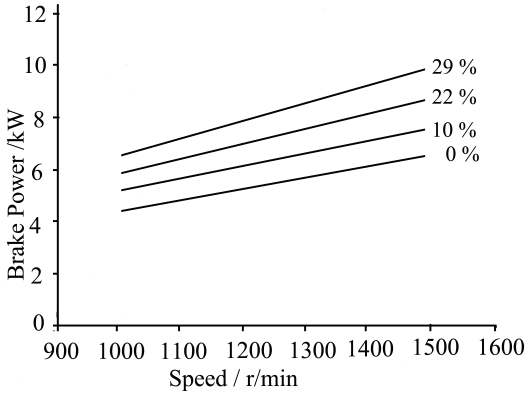


(c) Enthaply fraction from hydrogen

Figure 5.1. Experimentally obtained thermal efficiency contours of baseline diesel (a), diesel-$H_2$ dual fueling operation (b) and percentage enthalpy from hydrogen in diesel-$H_2$ dual fueling operation (c) where in all cases the pilot fuel contributes to 0.378 MPa of the total BMEP

manner. The full thermal efficiency contours with respect to both the power and the speed is expressed. The gradient of the contours indicates that at any value of power below 5 kW, and as engine speed increases, the thermal efficiency is monotonically decreasing. At higher engine powers, e.g. at 7 kW, the thermal efficiency is 32% at 1,100 r/min, increases to 33% at 1,250 r/min, and decreases from that maximum value with further increasing engine speeds.

The thermal efficiency contours of diesel piloted hydrogen dual fueling are shown in figure 5.1(b). They start from the baseline low-load line with BMEP value of 0.378 MPa

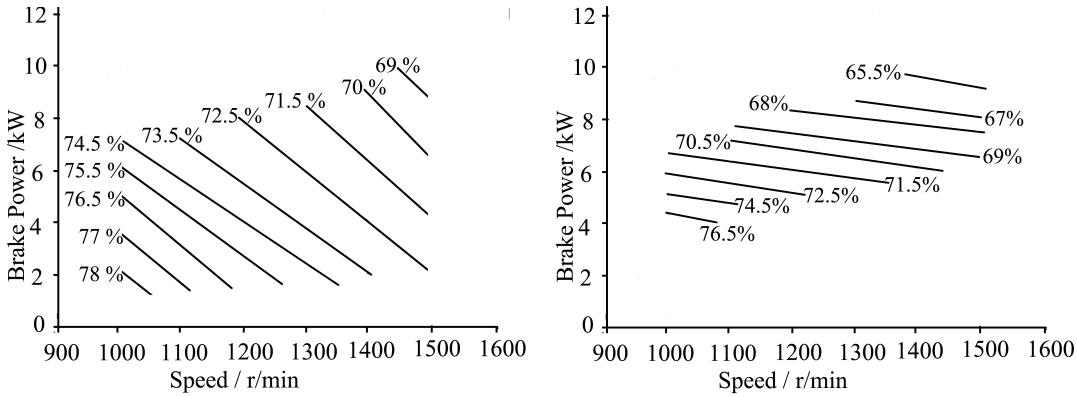


(a) Volumetric Efficiency - Diesel (b) Volumetric Efficiency - Diesel Plus $H_2$

Figure 5.2. Experimentally obtained volumetric efficiency contours of baseline diesel (a) and diesel-$H_2$ dual fueling operation (b) where in all cases the pilot fuel contributes to 0.378 MPa of the total BMEP

(where there is no hydrogen added i.e. all the fuel enthalpy is supplied by the diesel pilot fuel). Any further increase in power is obtained through the induction of hydrogen in the intake manifold, and the quantity of diesel pilot fuel is kept constant for that speed setting. The engine is operating at medium and higher load conditions when it is in dual fuel operation. The maximum enthalpy fraction from hydrogen in this case is 29% as illustrated in figure 5.1(c).

In the following comparisons between the various fueling modes are made at the same speed and power settings. When a smaller amount of hydrogen is inducted into the intake manifold, for instance when hydrogen is contributing 10% of the total fuel enthalpy, the thermal efficiency is 1.5% lower than the standard diesel-only fuel operation shown in figure 5.1(a). When the hydrogen enthalpy fraction was increased to 22% of the total fuel enthalpy, then the performance of the dual fuel mode deteriorated and the efficiency difference increased to 3% at the same speed and power settings. When the enthalpy fraction of $H_2$ was increased beyond 25% (near maximum power), it resulted in higher thermal efficiencies compared to the baseline diesel-only single fueling case at all speeds but the highest.

For different speeds while operating at hydrogen enthalpy fraction of 29% the increase in thermal efficiency was around 1.6% (at lower and medium speeds speed) but it was 3.0% lower at the highest speed. As demonstrated in appendix A, both diesel and RME piloted dual fueling cases of hydrogen produce higher peak pressure as well as higher rate of energy release peaks when compared to the respective pilot fuel based single fueling. This is in agreement with the literature in stating that the addition of hydrogen leads to an improvement in the thermal efficiency. However, at lower power outputs there is a reduction in thermal efficiency with hydrogen addition. At the highest power outputs the higher thermal efficiency values can be attributed to hydrogen contributing to more complete combustion due to higher combustion temperatures and pressures.

Comparison of figures 5.2(a) and 5.2(b) indicates that induction of hydrogen into the intake manifold compromises volumetric efficiency by approximately 5%; but near the peak loads attainable with dual fueling there is a 1.6% increase in thermal efficiency, especially at lower and medium speeds. This is because at lower and medium speeds hydrogen combustion is not affected by the phenomenon of under-mixing as observed in the single fueling case (the hydrogen is inducted into the intake manifold and it has more time to mix with air). This could be an advantage of manifold induction over direct injection of hydrogen into the combustion chamber.

In general, at a given power rating the volumetric efficiency decreases as the engine's speed increases due to increasing friction of the air flow during the induction and exhaust phase of the cycle. At a given engine operating speed higher loads mean more fuel and higher operating temperatures, including higher inlet manifold temperature, thus heating the intake air and adding to the reduction volumetric efficiency. Comparison of figures. 5.2(a) and 5.2(b) illustrates that the slope of the volumetric efficiency contours is flatter for hydrogen dual fueling than for baseline diesel operation. The lower values are observed because in the dual-fueling case, a part of the incoming air is being displaced by the hydrogen in the intake manifold, thus reducing the air flow rate. The frictional losses

are known to increase as the square of engine speed [10]. The slope of the iso-contours of volumetric efficiency for dual fuel mode differ significantly from those for single fuel mode. This is due to a larger portion of the intake air being displaced by the increasing addition of the hydrogen as the engine speed is increased. This increasing amount of displacement leads to a difference in scaling of volumetric efficiency with engine speed between the two modes. This is another consequence of the addition of the hydrogen in the intake manifold. As the volumetric efficiency is calculated from the air flow rate, increasing levels of hydrogen at the manifold displace air from the flow rate. There is less air flowing through the intake system thus the frictional effects of speed are reduced leading to the variation in scaling that is observed in the single fueling case.

The volumetric efficiency map as shown in figure 5.2(b) reflects the lower values for dual fuel mode. This is to be expected as a portion of the inducted air is being displaced by the hydrogen in the intake, reducing the air partial pressure below that of the mixture pressure. Also as to be expected is the drop of volumetric efficiency as the engine speed increases for both modes of operation. This drop in volumetric efficiency between the two modes is clear when figures 5.2(a) and 5.2(b) are compared. The frictional losses are known to increase as the square of engine speed [10] . The iso-contours of volumetric efficiency for dual fuel mode differ significantly from those for single fuel mode. This is due to a larger portion of the intake air being displaced by the increasing addition of the hydrogen as the engine speed is increased. This increasing amount of displacement leads to a difference in scaling of volumetric efficiency with engine speed between the two modes.

### 5.2.2 Specific $NO_X$

Figure 5.3(a) shows the full contours of specific $NO_X$ emissions for the engine operating on baseline diesel fuel. The absolute values of $NO_X$ emissions are increasing with increasing combustion temperature and increasing residence time. Therefore as engine operating speed is increased $NO_X$ emissions increase up to a maximum in mid operating speed, and then

decrease as residence time decreases with increasing speed.

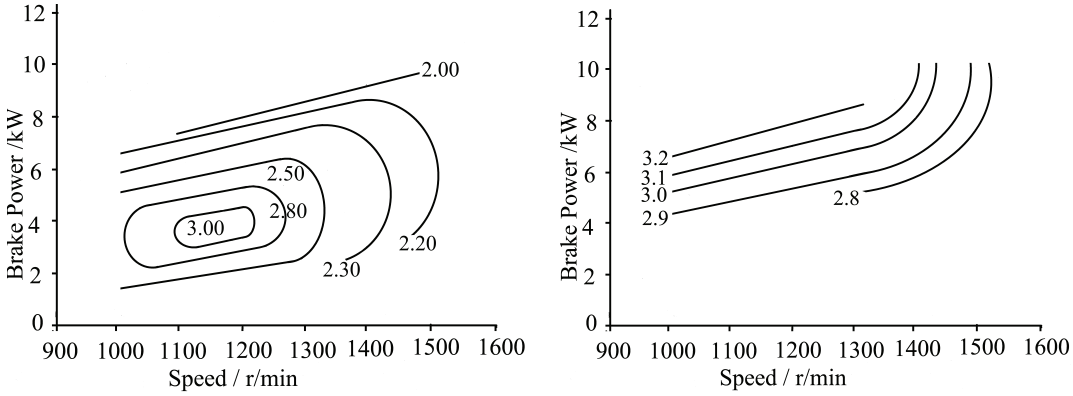


(a) Specific $NO_X$ /g/MJ - Diesel (b) Specific $NO_X$ /g/MJ - Diesel Plus $H_2$

Figure 5.3. Experimentally obtained specific $NO_X$ emissions contours for baseline diesel (a) and diesel-$H_2$ dual fueling (b)

At any engine operating speed the absolute $NO_X$ emissions increase with increasing power, but after the mid-power range the increase in absolute $NO_X$ is lower than the increase in power, so that the specific $NO_X$ emissions decrease above the mid-power range. These combined effects result in a central region of maximum specific $NO_X$ in the power-speed plane. At constant speed as the power output is increased or decreased from this central region, the specific $NO_X$ decreases. Similarly, at constant power as the speed is increased or decreased past the central region, the specific $NO_X$ decreases.

Figure 5.3(b) reflects the higher $NO_X$ specific emissions in the diesel-hydrogen dual-fueling case. Compared to the baseline diesel fueling, hydrogen based dual fueling resulted in higher $NO_X$ at all speed and power combinations. The high diffusivity (ability to disperse in air) of hydrogen makes the combustible mixture more pre-mixed, hence improving the combustion quality, resulting in higher in-cylinder temperatures. The smaller quenching distance in the case of hydrogen can be another reason for these higher specific $NO_X$ emissions. Smaller quenching distances make it possible for the hydrogen flame to travel closer to the combustion chamber walls before being extinguished, maintaining higher temperatures longer in the end phases of the combustion process. The range of specific $NO_X$

values is in a narrow band between 2.8 and 3.2 g/MJ across operating speeds and powers. This can be attributed to insignificant variation in minimum ignition energy required when the equivalence ratio varies in range $0.5<\phi<1.0$, leading in earlier beginning of combustion and therefore in higher in-cylinder temperature and pressure.

The slightly lower specific $NO_X$ values at higher speeds can be attributed to the shorter residence time available. The specific $NO_X$ values reflect three parameters: the in-cylinder temperature; the oxygen available; and the efficiency of the engine (a result of the specific nature of the measurement). As the power increases at constant speed, higher absolute $NO_X$ results due to higher in-cylinder temperature, and at the same time the engine is becoming more efficient. At higher powers, the rate at which the in-cylinder temperature increases is dominated by the rate at which the engine efficiency increases with any changes in the load applied to the engine. Therefore the lower ignition energy and wider operating equivalence ratio of hydrogen result in the specific $NO_X$ trends in the diesel-hydrogen fueling case to follow the shape of the thermal efficiency contours.

### 5.2.3 Specific HC

For the baseline single-fuel diesel case the specific HC emissions shown in figure 5.4(a) follow the reverse of the thermal efficiency contour shapes. Thus the lowest values of the specific HC emissions are at the regions of the highest thermal efficiency contours, and the highest specific HC emissions are measured at the lowest power outputs.

The specific HC emissions map for diesel piloted hydrogen dual-fueling mode is shown in figure 5.4(b). The specific HC emissions follow similar trends (they follow the reverse of the thermal efficiency contours for the dual-fueling case). Overall at the same speed and power settings the specific HC emissions are slightly lower in the dual fuel mode compared to the baseline diesel single-fuel case. This is because the amount of carbon going into the engine is not increasing as the pilot fuel quantity is fixed at the base load setting. Better combustion at higher load due to higher in-cylinder temperature can be another reason

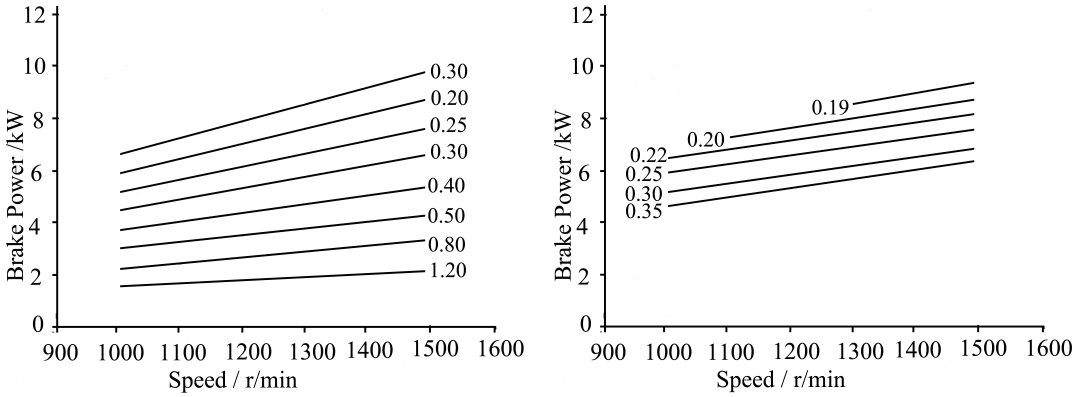


(a) Specific HC /g/MJ - Diesel (b) Specific HC /g/MJ - Diesel Plus $H_2$

Figure 5.4. Experimentally obtained specific HC emissions contours for baseline diesel (a) and diesel-$H_2$ dual fueling (b)

for this significant decrease in specific HC. This shows that unlike diesel, diesel ignited $H_2$ combustion does not have the problem of under mixing at higher loads. Figure 5.1(b) illustrates that at the highest power with the enthalpy fraction of hydrogen at 29%, the dual fueling case is more efficient compared to single fueling at the same operating points. This demonstrates a higher combustion efficiency as well as producing more brake power. This is another reason for the reduction of the HC emissions. Fundamental studies of non-premixed combustion have shown increased flame stability due to higher flame speeds and improved mixing with increased hydrogen addition [108]. The results presented here are consistent with this argument. Although the volumetric efficiency of the dual fueling case is about 5% less than diesel based single fueling, the specific HC values are lower. This can be attributed to better mixing of the hydrogen and air, the lower carbon content in the mixture, and the faster reaction rates of hydrogen combustion.

### 5.2.4 Specific $CO_2$

Figures 5.5(a) and 5.5(b) show specific $CO_2$ maps for the baseline diesel and the diesel piloted dual fueling of hydrogen respectively. Diesel piloted hydrogen combustion produces less $CO_2$ when compared to the pure diesel based single fueling . When the

hydrogen fraction is 22% and 29%, a decrease of 12.5% and 35% in $CO_2$ is observed. When

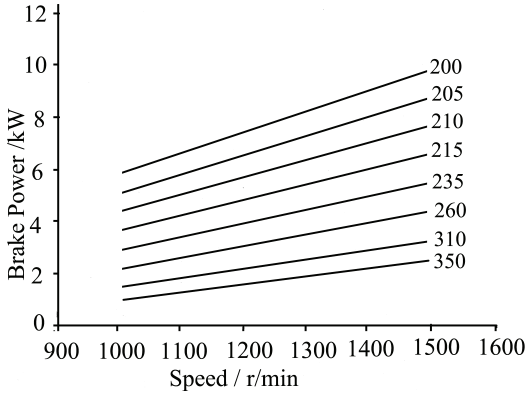


(a) Specific $CO_2$/g/MJ - Diesel

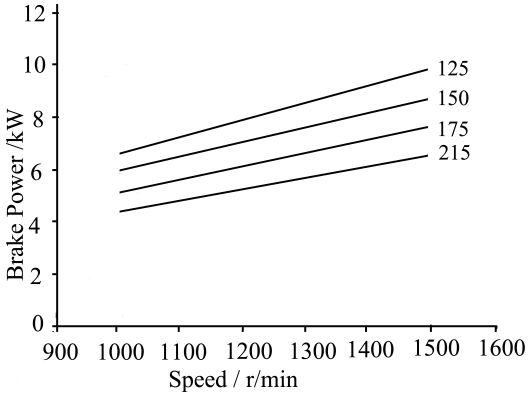


(b) Specific $CO_2$ /g/MJ - Diesel Plus $H_2$

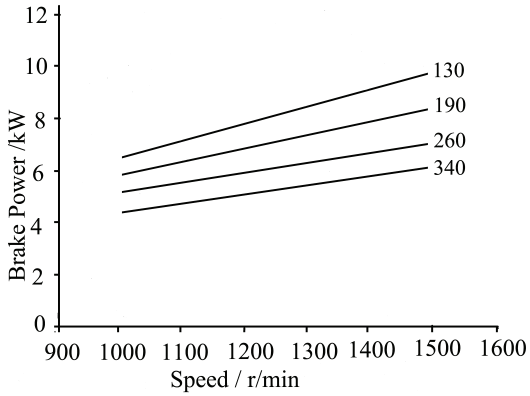


(c) Specific $O_2$ /g/MJ - Diesel Plus $H_2$

Figure 5.5. Experimentally obtained specific $CO_2$ emissions contours for baseline diesel (a) and diesel-$H_2$ dual fueling (b) and specific $O_2$ emissions for diesel-$H_2$ dual fueling (c)

compared to diesel based normal fueling, lower values of $CO_2$ emissions can be attributed to the lower carbon to hydrogen ratio. About a 5% loss in volumetric efficiency can be another reason for this but the specific $O_2$ map for the dual fueling as shown in figure 5.5(c) does not support this argument. Similar levels of specific $O_2$ are observed both for the single as well as dual fueling case. This also shows that the improved combustion of hydrogen can compensate for the oxygen which is displaced by the injection of hydrogen into the intake manifold.

## 5.3 RESULTS AND DISCUSSION - RME PILOTED $H_2$

This section presents thermal efficiency, volumetric efficiency, specific $NO_X$, specific HC and specific $CO_2$ maps for RME piloted dual fueling of hydrogen and compares them against the maps obtained with diesel based single fueling.

### 5.3.1 Thermal Efficiency and Volumetric Efficiency

Figure 5.6(a) illustrates the thermal efficiency contours for the engine operating under normal CI conditions when fueled with RME. Overall the shape of the thermal efficiency contours for diesel and RME baselines are very similar, but the thermal efficiency with RME is marginally higher than with diesel. The thermal efficiency contours with hydrogen dual fueling and RME pilot fuel are shown in figure 5.6(b).

They start from the baseline low-load line with BMEP value of 0.378 MPa (where there is no hydrogen added i.e. all the fuel enthalpy is supplied by the RME pilot fuel). Any further increase in power is obtained through the induction of hydrogen in the intake manifold, and the quantity of RME pilot fuel is kept constant for that speed setting. The engine is operating at medium and higher load conditions when it is in dual fuel operation. The maximum enthalpy fraction from hydrogen in this case is 33% as illustrated in figure 5.6(c).

Similar to the diesel-pilot case, the engine is operating at high medium and high power conditions when it is fueled by RME-piloted hydrogen. Comparison of the figures 5.6(a) and 5.6(b) illustrate that the thermal efficiency has deteriorated with addition of hydrogen, and the deterioration is slightly higher than what is observed in the diesel piloted hydrogen dual fueling case. When 15% , 27% and 33% of the total enthalpy is provided by hydrogen, the thermal efficiency of this dual fueling case decreases by about 5% for all cases at all speeds. Similar differences are observed when diesel piloted hydrogen combustion is compared to RME piloted hydrogen combustion. From the thermal efficiency point of view diesel has proved to be better pilot fuel compared to RME. More hydrogen is inducted when

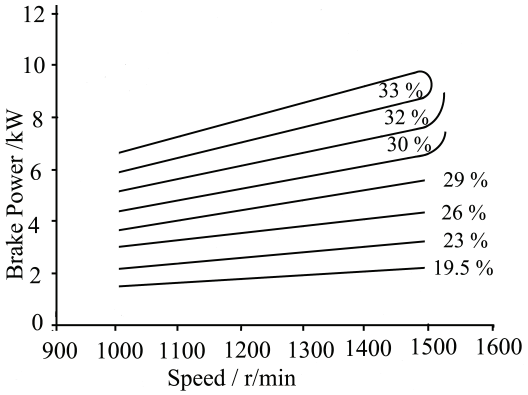


(a) Thermal Efficiency - RME

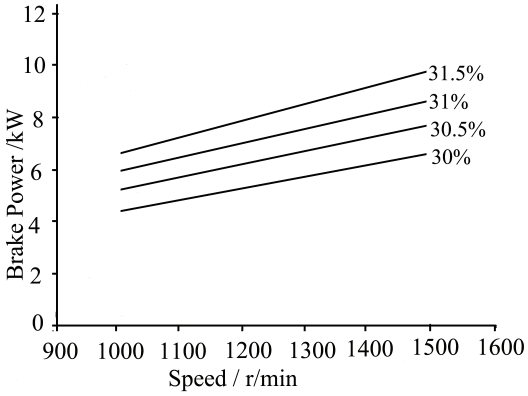


(b) Thermal Efficiency - RME Plus $H_2$

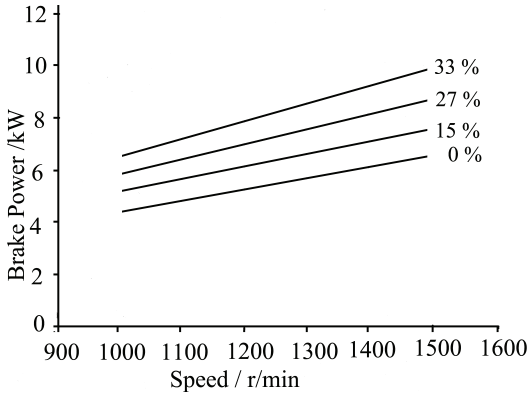


(c) Enthaply fraction from hydrogen

Figure 5.6. Experimentally obtained thermal efficiency contours of baseline RME (a), RME-$H_2$ dual fueling operation (b), and percentage enthalpy from hydrogen in RME-$H_2$ dual fueling operation (c) where in all cases the pilot fuel contributes to 0.378 MPa of the total BMEP

RME is used to pilot the hydrogen combustion. The performance comparison of diesel and RME as pilot fuels is shown in Table 5.1. The inferior performance of RME as a pilot fuel can be attributed to its poor ignition characteristics. The table shows hydrogen enthalpy fraction against any improvement or deterioration in thermal efficiency and specific $NO_X$. The thermal efficiency and $NO_X$ columns contain percentage change in these parameters when compared to the respective single fueling cases with diesel and RME as baselines.

The slopes and values of volumetric efficiency contours for diesel and RME baseline cases as shown in figures 5.2(a) and 5.7(a) are very similar . The slope of the volumetric

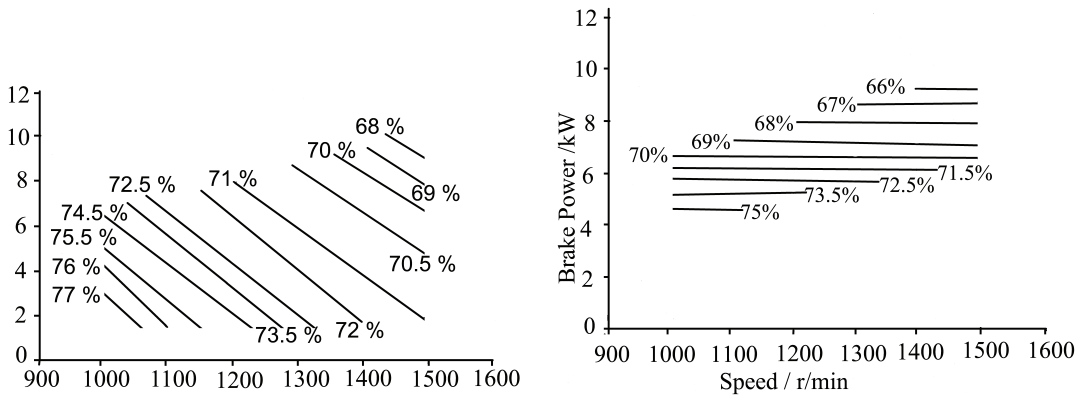


(a) Volumetric Efficiency - RME

(b) Volumetric Efficiency - RME Plus $H_2$

Figure 5.7. Experimentally obtained volumetric efficiency contours of baseline RME (a) and RME-$H_2$ dual fueling operation (b) at constant pilot fuel BMEP of 0.378 MPa

efficiency contours for RME piloted combustion of hydrogen as shown in figure 5.7(b) is flatter than the slope of the volumetric efficiency contours for diesel piloted hydrogen as shown in figure 5.2(b). This is a consequence of the reduced heating value of RME compared to diesel. Figures 5.1(c) and 5.6(c) show the enthalpy contribution of hydrogen for diesel and RME piloted dual fueling of hydrogen. The enthalpy fraction of hydrogen at each setting is larger with RME as compared to the diesel dual fueling hence a larger proportion of the intake air is being displaced by the hydrogen, further increasing the change in scaling between speed and volumetric efficiency as discussed previously at the end of section 5.2.1.

### 5.3.2 Specific $NO_X$

Figures 5.8(a) and 5.8(b) illustrate the specific $NO_X$ contours for the RME baseline and the RME piloted dual fueling of hydrogen respectively. The overall trends and explanations for the specific $NO_X$ emissions with RME single fueling are analogous to those of baseline diesel and diesel-piloted hydrogen of the previous section. Comparison of figures 5.8(a) and 5.8(b) reflect an overall higher $NO_X$ with RME piloted hydrogen combustion when compared to the RME single fueling case.

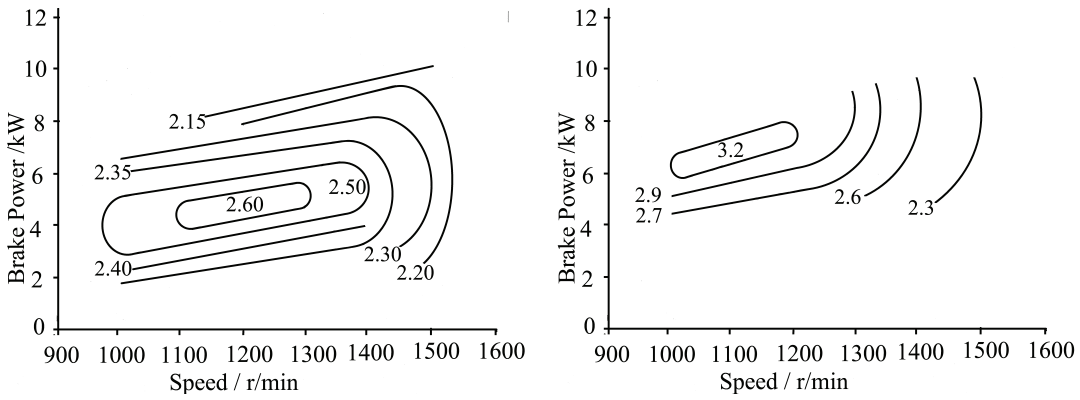


(a) Specific $NO_X$ /g/MJ - RME (b) Specific $NO_X$ /g/MJ - RME Plus $H_2$

Figure 5.8. Experimentally obtained specific $NO_X$ emissions contours for RME baseline (a) and RME-$H_2$ dual fueling (b)

The RME piloted hydrogen combustion results in higher absolute $NO_X$ due to higher in-cylinder temperatures. In addition the comparison of the thermal efficiency contours suggests that the RME piloted dual fueling is less efficient compared to pure RME single fueling across the entire contour range. When the two dual fueling cases are compared in terms of specific $NO_X$ emissions, RME piloted hydrogen combustion produces lower specific $NO_X$ compared to the diesel based dual fueling. Reduced volumetric efficiency in case of RME piloted hydrogen combustion when compared to the diesel based dual fueling case can be a reason for lower $NO_X$.

### 5.3.3 Specific HC

Figures 5.9(a) and 5.9(b) illustrate the specific HC maps for the RME baseline and the RME piloted dual fueling of hydrogen respectively. The overall trends and explanations for specific HC emissions with RME single fueling and RME piloted dual fueling of hydrogen are analogous to those of baseline diesel and diesel-piloted hydrogen of the previous section.

Similar or slightly higher specific HC values are recorded when RME substitutes diesel for piloted hydrogen combustion. This small difference in specific HC numbers can be

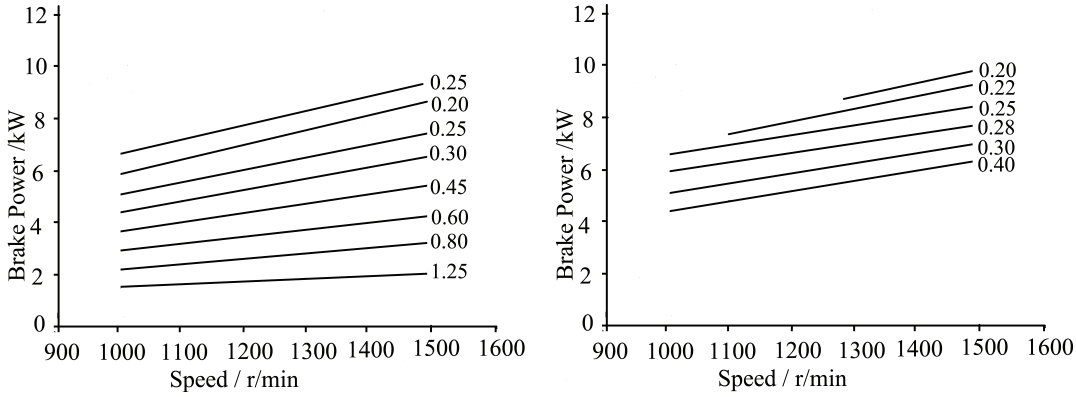


(a) Specific HC /g/MJ - RME (b) Specific HC /g/MJ - RME Plus $H_2$

Figure 5.9. Experimentally obtained specific HC emissions contours for RME baseline(a) and RME-$H_2$ dual fueling (b)

attributed to the relatively poor atomization and ignition characteristics of RME compared to diesel for the similar roles.

Although more carbon is being injected at higher power outputs, in the case of single fueling the specific HC values for both modes (single and dual) are practically the same. Figures 5.6(a) and 5.6(b) that illustrate the thermal efficiency contours for the two modes can be used to explain this trend. As discussed earlier, RME based single fueling is shown to be more efficient compared to RME piloted hydrogen dual fueling. This results in more brake power thus reducing the magnitude of specific HC emissions despite the fact that the absolute values of HC are higher.

### 5.3.4 Specific $CO_2$

Figures 5.10(a) and 5.10(b) illustrate the specific $CO_2$ maps for the RME baseline and the RME piloted dual fueling of hydrogen respectively. The overall trends and explanations for specific $CO_2$ emissions with RME single fueling and RME-piloted hydrogen are analogous to those of baseline diesel and diesel-piloted hydrogen of the previous section. No significant difference in specific $CO_2$ emissions is observed when the pilot fuel choice was switched from diesel to RME. This is due to similar hydrogen to carbon ratio for both pilot

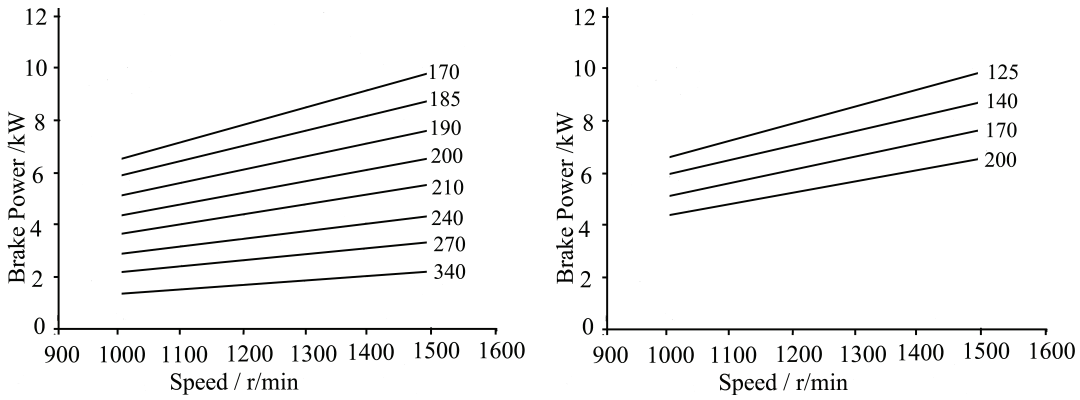


(a) Specific $CO_2$/g/MJ - RME (b) Specific $CO_2$ /g/MJ - RME Plus $H_2$

Figure 5.10. Experimentally obtained specific $CO_2$ emissions contours for baseline RME (a) and RME-$H_2$ dual fueling (b)

fuels. When compared to pure RME based fueling, $CO_2$ values are higher at all speeds and powers in the case of RME piloted combustion of hydrogen.

## 5.4 CHAPTER SUMMARY

This chapter presents performance and emissions contours of a hydrogen dual fueled CI engine with two pilot fuels (diesel and RME), and compares the performance and emissions iso-contours of diesel and RME single fueling with diesel and RME piloted hydrogen dual fueling throughout the engine's operating speed and power range. Performance and emissions data has been collected at six engine operating speeds and eight different load settings for single fueling, and four load settings for dual fueling. The load settings have been used to determine the brake power the engine is producing. The collected data has been used to produce iso-contours of thermal efficiency, volumetric efficiency, specific $NO_X$, specific HC and specific $CO_2$ on a power-speed plane. The performance and emissions contours are experimentally investigated, assessed, compared and critically discussed. Considering these iso-contours provides greater insight across a wider operational range of a dual fuel engine. Apart from medium loads at lower and medium speeds with diesel piloted hydrogen combustion, dual fueling produced lower thermal efficiency everywhere across the map. For

| Pilot Fuel | Load/Speed | Enthalpy Fraction of $H_2$ | Thermal efficiency | Specific $NO_X$ |
|---|---|---|---|---|
| Diesel | Lower Medium/All | 10% | 1.5%↓ | 3.3%↑ |
| | Medium /Low → Medium | 22% | 3.2%↓ | 16%↑ |
| | High/Low → Medium | 29% | 1.5%↑ | 31%↑ |
| | High/High | 29% | 3.2%↑ | 27%↑ |
| RME | Lower Medium/All | 15% | 4.5%↓ | 4%↑ |
| | Medium /All | 27% | 6%↓ | 7%↑ |
| | High/All | 33% | 4.5%↓ | 23%↑ |

Table 5.1. Performance comparison of Diesel and RME as pilot fuels in hydrogen combustion

diesel and RME single fueling the maximum specific $NO_X$ emissions are centered at the mid speed, mid power region. Hydrogen dual fueling produce higher specific $NO_X$ with both pilots as compared to their respective single fueling operations. The range, location and trends of specific $NO_X$ varied significantly when compared to single fueling cases. The volumetric efficiency is discussed in detail with the implications of manifold injection of hydrogen analyzed.

# CHAPTER 6

# EFFECT OF PILOT FUEL QUANTITY AND TYPE ON COMBUSTION AND EMISSIONS OF NATURAL GAS AND HYDROGEN IN DUAL FUELING MODE

## 6.1 BACKGROUND AND MOTIVE

Development of alternative fuels to replace the conventional fuels in IC engines is an active area of research. Fuels derived from different resources (especially but not exclusively renewable ones) have been tested in IC engines with their performance and emissions characteristics investigated to assess their suitability as substitute fuels. Both natural gas and hydrogen have long been considered alternative fuels for the transportation sector and have fueled vehicles for decades.

When compared to the reserves of crude oil on volume basis, natural gas has much larger reserves, estimated to be 5288.5 trillion cubic feet [101]. The cleanliness of any burning process is indicated by the amount of soot or smoke produced, natural gas qualifies this test owing to its lower carbon content. Natural gas is generally a mixture of primary alkanes with methane ($CH_4$) contributing around 95%.

An initial source of ignition is required to ignite both natural gas and hydrogen-air mixtures in unmodified CI engines. This is due to lower cetane number (high octane number) of natural gas [101, 104] and high auto-ignition temperature of hydrogen. To ignite these gaseous fuel in compression ignition engine, various ignition strategies have been employed. A glow plug or a high cetane liquid fuel such as diesel [60, 6, 105, 115] or a biodiesel [116, 114, 117, 6] have been widely used as an initial source of ignition using the piloted dual fuel concept [106]. All of these studies consider a fixed quantity of pilot fuel, hence the effect of varying quantity of pilot fuel remains to be investigated.

Natural gas has high specific heat capacity ratio ($\gamma$). Due to this, the temperature of the in-cylinder charge is lowered and hence ignition is delayed which is critical from

an emissions perspective [84, 100]. These studies have considered a variety of pilot fuels but were limited to a fixed quantity of pilot fuel. They present a good comparison of how different pilot fuels perform under certain operating conditions but lack an account on what will be the effect if the pilot fuel quantity is varied.

When compared to baseline single fueling case, the natural gas based dual fueling mode exhibit a slight reduction in brake thermal efficiency at lower loads [60, 107, 105, 108, 65]. Higher thermal efficiency values were reported at higher loads for natural gas dual fueling [59]. Hydrogen has been shown to increase flame stability [108] and improve thermal efficiency [79]. It is believed that the high diffusion coefficient of hydrogen leads to highly turbulent flame propagation rate [108]. The addition of hydrogen to increase the flame stability has been studied extensively because of the belief that flame propagation is the key factor in improving combustion [108, 122, 119, 123, 96]. All of these studies highlight one or the other important aspect of the natural gas and hydrogen based dual fueling cases but the effect of changing the pilot fuel quantity and type on various combustion and emissions parameters has not been reported.

Concerning total brake specific fuel consumption, it is revealed that it becomes inferior under dual fuel operation compared to normal diesel operation at the same engine operating conditions. At high load, the values of total brake specific fuel consumption under dual fuel operation tend to converge with that of normal diesel operation [60]. The concept of multi ignition centers that result from the pilot fuel igniting the gaseous fuels in case of dual fueling modes requires an investigation on how changing the number of ignition centers (by injecting a different quantity of pilot fuel) shall affect the total brake specific fuel consumption and hence power and emissions characteristics. The lower heating value of the fuel also affects brake specific fuel consumption. It is worth investigating how two pilot fuels with different lower heating values shall perform in dual fuel mode from the brake specific fuel consumption perspective.

$NO_X$ is a strong function of local temperatures. It has been reported that most of the

$NO_X$ are formed in the region around the pilot spray where high temperatures exist and the equivalence ratio is close to stoichiometric [109]. Natural gas based dual fueling results in lower $NO_X$ emissions when compared to the $NO_X$ concentration under normal single fuel operation. At the same time, a significant decrease in soot emissions under dual fuel operation has also been reported. On the other hand, CO and HC emissions levels have been reported to be considerably higher compared to normal diesel operation [60, 111, 107, 84, 100]. How would these different emissions parameters change if both the quantity as well as the type of the pilot fuel are changed, remain to be investigated and reported.

Hydrogen has high burning velocity which can lead to increased in-cylinder pressures and higher temperatures, resulting in increased $NO_X$ emissions. Hydrogen is flammable over a wide range of concentrations in air(from 4% to 75%) [116, 118, 115]. This wider flammability can be used to prepare leaner mixtures resulting in lower in-cylinder temperatures and pressures and hence reduced $NO_X$ emissions [119]. However, the initiation and development of the multiple turbulent flames requires a $H_2$-air mixture richer than the lean flammability limit [120]. Most studies have limited the enthalpy fraction of hydrogen addition to a maximum of 15% [116, 108]. The upper limit of hydrogen addition with manifold injected hydrogen is determined by the quenching gap of hydrogen flame which can travel past the nearly-closed intake valve and more readily backfires into the engine's intake manifold [121]. Using different quantities of the pilot fuels to achieve a certain BMEP in hydrogen dual fueling can be helpful in quantifying the effect of wider flammability and smaller quenching gap on different performance and emissions parameters.

Most of the studies reported on natural gas and hydrogen dual fueling lack one or the other important aspect. They are either confined to one type of gaseous fuel (either hydrogen or natural gas) or one type of pilot fuel (either diesel or a biodiesel). These two dual fueling cases with two different pilot fuels have hardly been reported in a single study. Changing the quantity of pilot fuel in natural gas and hydrogen based dual fueling is yet to be investigated, compared and reported. This study is an effort to fill all these gaps

in the literature on natural gas and hydrogen based dual fueling of compression ignition engines. The study was conducted at two different engine speeds and the effect of variation in engine speed on different performance and emissions parameters has also been discussed.

## 6.2 RESULTS AND DISCUSSION - NATURAL GAS

This section is further divided into two parts. The first part discusses the implications of the change in the pilot fuel quantity and type on in-cylinder pressure,rate of energy release and ignition delay. The second part discusses the effect of change in pilot the fuel quantity and type and engine speed on different emissions.

### 6.2.1 Ignition Delay and Pressure Data

Figure 6.1 reflects the effect of pilot fuel quantity on ignition delay for pure diesel and pure RME as well as three natural dual fueling cases piloted by each of these two fuels. When compared to pure diesel and pure RME at 1500 rev/min and 0.503 MPa BMEP, all of the natural gas based dual fueling cases have shown larger ignition delay. For all combinations of the pilot fuel quantity , type and engine speed, the lowest pilot fuel setting (n=1) has exhibited maximum ignition delay and the ignition delay was generally reduced as the quantity of the pilot fuel was increased. This can be attributed to more ignition centers being resulting form the injection of greater amount of pilot fuel and hence shortening the time between the fuel injection and the start of the ignition process. RME piloted dual fueling of natural gas at 1000 rev/min showed a slightly different trend where the medium pilot fuel setting (n=2) showed the minimum ignition delay when compared to the two other pilot fuel settings (n=1,3). At lowest pilot fueling setting (n=1), the enthalpy contribution of the natural gas is maximum. As n ( the BMEP value where the pilot fuel quantity is fixed) increases, the pilot fuel is set at a relatively higher BMEP resulting in relatively lower enthalpy contribution from the natural gas. The specific heat capacity ratio $\gamma$ for the natural gas - air mixture is considerably higher than the pure air.

This higher specific heat capacity ratio results in lower in-cylinder temperatures and hence an increased ignition delay. The ignition delay for the middle pilot fuel setting (n=2) is

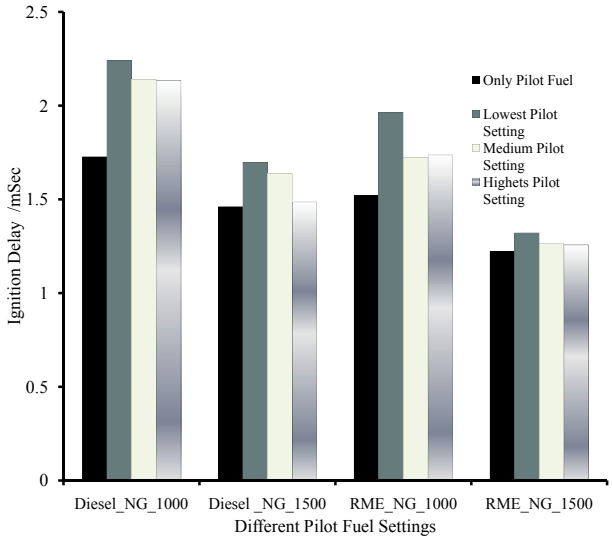


Figure 6.1. Effect of pilot fuel quantity, type and engine speed on ignition delay for different pilot fuel settings in diesel and RME piloted combustion of natural gas at 1000 rev/min and 1500 rev/min

marginally different from the highest pilot fuel setting (n=3). This can be attributed to the fact that there is only a difference of 0.069 MPa between these two cases when compared to a difference of 0.127 MPa between the lowest (n=1) and the middle pilot fuel setting (n=2). Insignificant difference between the ignition delays of the two higher pilot fuel quantity settings (n=2,3) suggests that increasing the pilot fuel quantity shall not result in proportional reduction in ignition delay. This view seems to hold good for all cases and diesel piloted natural gas combustion at 1500 rev/min is the exception where significant reduction has been observed as quantity of pilot was increased.

Figure 6.2(a) shows the in-cylinder pressure and figure 6.2(b) shows the corresponding rate of energy release for pure diesel and three cases of natural gas dual fueling with three different diesel pilot fuel settings to achieve a BMEP of 0.503 MPa and 1500 rev/min. Figure 6.3(a) shows the in-cylinder pressure and figure 6.3(b) shows the corresponding rate of energy release for pure RME and three cases of natural gas dual fueling with three different RME pilot fuel settings to achieve BMEP of 0.503 MPa and 1000 rev/min.

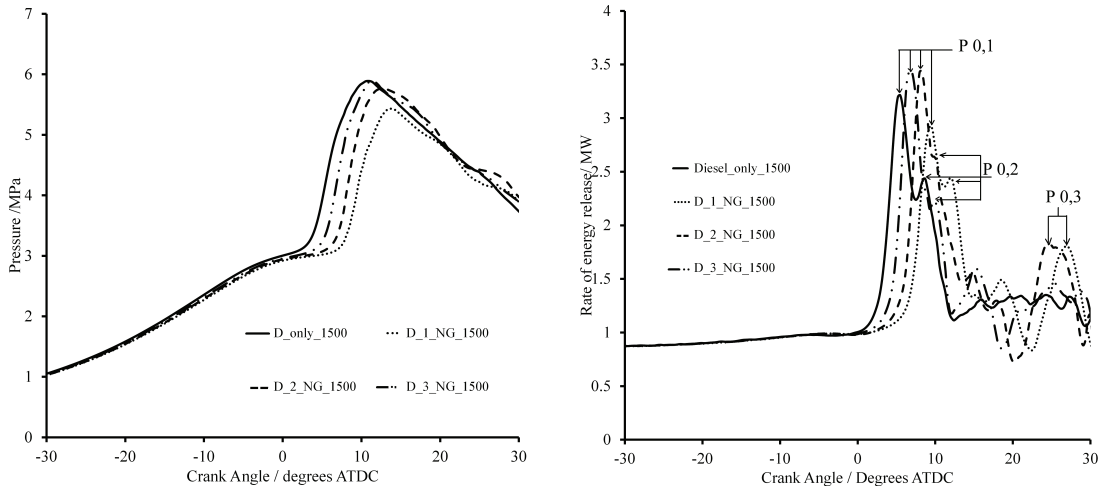


(a) Cylinder Pressure for pure diesel and three cases of natural gas combustion with different diesel pilot fuel settings at a BMEP of 0.503 MPa and 1500 rev/min

(b) Rate of energy release for pure diesel and three cases of natural gas combustion with different diesel pilot fuel settings at a BMEP of 0.503 MPa and 1500 rev/min

Figure 6.2. Effect of the pilot fuel quantity and type on in-cylinder pressure (a) and rate of energy release (b) for pure diesel and three cases of natural gas combustion with different diesel pilot fuel settings at a BMEP of 0.503 MPa and 1500 rev/min

As reflected in figure 6.2(a), for diesel piloted dual fueling of natural gas, the combustion peaks followed the trend observed for the ignition delays for different fuel combinations. Higher combustion peak was achieved when the ignition delay was reduced. For 1000 rev/min with diesel piloted combustion of natural gas, the ignition delay has shown similar trends as shown at 1500 rev/min as the lowest pilot fuel quantity has shown maximum ignition delay but there was no significant difference noted between the two higher pilot fuel settings. In figure 6.2(b), $P_{0,1}, P_{0,2}$ and $P_{0,3}$ are the points on the rate of energy release graph pointing towards the first, second and the third (if any) peaks respectively for diesel piloted dual fueling of natural gas. The highest peak for the rate of energy release (indicated by $P_{0,1}$) for different pilot fuel settings has shifted in proportion to the ignition delay observed. The two higher pilot fuel settings (n=2,3) have resulted in higher peaks

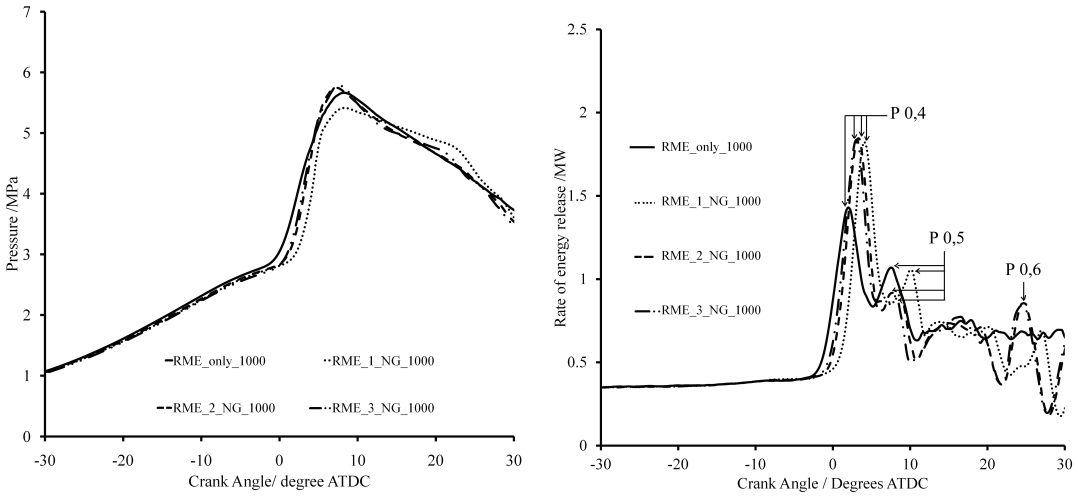


(a) Cylinder Pressure for pure RME and three cases of natural gas combustion with different RME pilot fuel settings at a BMEP of 0.503 MPa and 1000 rev/min

(b) Rate of energy release for pure RME and three cases of natural gas combustion with different RME pilot fuel settings at a BMEP of 0.503 MPa and 1000 rev/min

Figure 6.3. Effect of the pilot fuel quantity and type on in-cylinder pressure 6.3(a) and rate of energy release 6.3(b) for pure RME and three cases of natural gas combustion with different RME pilot fuel settings at a BMEP of 0.503 MPa and 1000 rev/min

for the rate of energy release when compared to the lowest pilot fuel setting. Although the two higher pilot fuel settings exhibit similar peaks (point $P_{0,1}$) for the rate of release peaks but the two peaks occur at different crank angles. The first peak for the rate of energy release for pilot setting (n=2) occurs 8.089° CA ATDC whereas for pilot setting (n=3), it occurs at 6.84° CA ATDC. For the lowest pilot fuel setting, the the first peak for the rate of energy release occurs at 9.39° CA ATDC. For the two cases (n=2,3), a relatively longer ignition delay when compared to the diesel based single fueling has retarded the first peak ($P_{0,1}$) for the rate of energy release.

The second peak for the rate of energy release (indicated by $P_{0,2}$) at 11.96° is more clear when the pilot fuel is set at the lowest BMEP (n=1) whereas it is not very clear for the higher pilot fuel settings (n=2,3). The third peak (indicated by $P_{0,3}$) is observed for the

lowest (n=1) at 27° and for the middle (n=2) pilot fuel settings at 24° whereas the highest pilot fuel setting (n=3) shows the trend similar to what is observed with pure diesel in the latter part of the combustion. The latter peaks in case of relatively lower pilot fuel setting cases can be attributed to the fact that some of the gaseous does not get oxidized in the earlier phase of combustion and hence cause these latter peaks.

For RME piloted dual fueling of natural gas at 1000 rev/min as shown in figure 6.3(a), lower peak pressure was recorded for the lowest pilot fuel setting (n=1) whereas similar rate of pressure rise and the peak pressures were observed with two of the higher pilot fuel settings (n=2,3). In figure 6.3(b), $P_{0,4}, P_{0,5}$ and $P_{0,6}$ are the points on the rate of energy release diagram pointing towards the first , second and the third peak (if any) respectively for diesel piloted dual fueling of natural gas. The first rate of energy release peak for the three RME piloted dual fueling cases (indicated by $P_{0,4}$) occurs at 4° CA ATDC for the lowest pilot setting whereas 3.2° CA ATDC for the two higher pilot fuel settings (n=2,3). The second rate of energy release peak ($P_{0,5}$) occurring at 10.12° CA ATDC is more clear for the lowest pilot fuel setting whereas the two higher pilot fuel setting cases, the second rate of energy release peak occur at 8.14° CA ATDC. The two higher pilot fuel settings show a noticeable third peak ($P_{0,6}$)in the latter part of the combustion event (24 ° CA ATDC) which is not observed with the lowest pilot fuel setting case.

### 6.2.2 Specific $NO_X$

Figure 6.4(a) shows specific $NO_X$ emissions for diesel piloted combustion of natural gas at 1500 rev/min. Figure 6.4(b) shows specific $NO_X$ emissions for RME piloted combustion of natural gas at 1000 rev/min. At 1000 rev/min, apart from the highest load condition, the diesel piloted natural gas combustion produced minimum $NO_X$ when the quantity of the pilot fuel was set at a minimum BMEP value(n=1). Maximum $NO_X$ were produced when the diesel pilot was set at a BMEP value of 0.251 MPa. A linear increase in specific $NO_X$ with any increment in BMEP was observed for pilot fuel settings of n=2,3 whereas for n=1,

the specific $NO_X$ initially dropped then an increase was observed. At similar speed (1000 rev/min), RME piloted natural gas combustion demonstrated different trends as compared to the diesel piloted case. Any increase in pilot fuel quantity resulted in lower specific $NO_X$. With pilot fuel set at the minimum (n=1), both RME as well as diesel based combustion of natural gas showed similar trend as there was an initial decrease and then a serge was observed although they differed in magnitude as RME resulted in higher specific $NO_X$ at the minimum pilot fuel setting. For the two higher pilot fuel settings (n=2,3), RME piloted

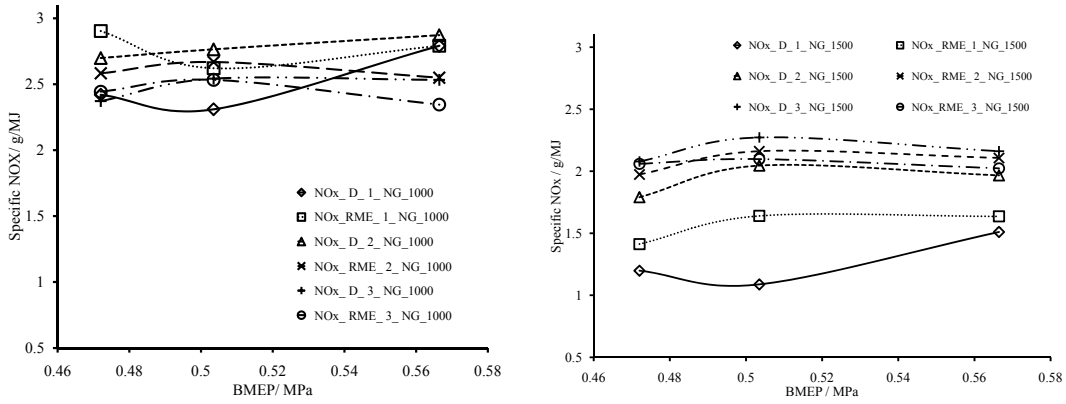


(a) Specific $NO_X$ for natural gas combustion with three different diesel pilot and RME pilot fuel settings at 1000 rev/min

(b) Specific $NO_X$ for natural gas combustion with three different diesel pilot and RME pilot settings at 1500 rev/min

Figure 6.4. Effect of pilot fuel quantity and type on specific $NO_X$ emissions at 1000 rev/min (a) and 1500 rev/min (b)

combustion of natural gas produced lower specific $NO_X$ as compared to the diesel piloted natural gas combustion. Lower specific $NO_X$ resulted for all case six cases at 1500 rev/min when copmared to the similar conditions at 1000 rev/min At 1500 rev/min, the diesel based natural gas dual fueling has shown different trends for specific $NO_X$ when compared to the same fuel settings at 1000 rev/min. The specific $NO_X$ were observed increasing as the quantity of pilot fuel was increased. At minimum pilot fuel setting (n=1) for diesel piloted natural gas combustion, the specific $NO_X$ exhibited similar trend at both speed i.e. an initial decrease and then an increase in specific $NO_X$. For all other cases at 1500 rev/min,

the specific $NO_X$ increased initially and then stayed constant. An offset proportional to the quantity of pilot fuel was observed for for $NO_X$ from diesel piloted natural gas whereas RME based natural gas dual fueling produced similar (or slightly different) magnitudes of specific $NO_X$ for the two higher pilot fuel settings (n=2,3). The trends of specific $NO_X$ emissions can be attributed to multi-centered ignition of the dual fuelling. At relatively lower BMEP values, lower values of specific $NO_X$ with lower quantity of pilot fuel can be attributed to the failure of the pilot fuel to ignite natural gas and air mixture properly. The increase observed in specific $NO_X$ attributed to relatively higher in-cylinder temperature. The higher in-cylinder temperature can ensure timely evaporation of the pilot fuel and hence better distribution of the ignition centers across the charge. At lower speeds (1000 rev/min in this case), the lower specific $NO_X$ with the highest pilot fuel setting (n=3) can be attributed to the cooling caused as a result of fuel evaporation. Greater quantity of pilot fuel results in large number of ignition centres and the cooling effect of the fuel evaporation is more pronounced at this condition as compared to the lower pilot fuel quantities. The maximum specific $NO_X$ with pilot fuel setting at a medium BMEP suggests that there is a pilot fuel quantity threshold for specific $NO_X$ where these are maximum and there would be lower specific $NO_X$ below or above this threshold. There can be many reasons for this trend. Some of them have been already presented in this section but there may be some other factors playing their roles. Both for diesel and RME piloted dual fueling of natural gas at 1000 rev/min and the highest BMEP values, the specific $NO_X$ resulted from the lowest pilot fuel setting ((n=1) supersedes the specific $NO_X$ resulted from the highest pilot fuel setting. This can be attributed to the subsequent rate of energy release peaks occurring after the highest peak for the lowest pilot fuel quantity case.

Lower values of specific $NO_X$ with RME based natural gas operation when compared to diesel piloted natural gas operation can be explained on the basis of higher cetane number of RME as compared to the diesel fuel. Premixed combustion is strongly affected by ignition delay. Lower cetane number has been reported to result in longer ignition delays

and hence more time for premixed combustion, leading to higher in-cylinder temperature. In the pre-mixed combustion phase, fuel and air that have already mixed ignite, causing a rapid rise in temperature and pressure. This temperature and pressure rise depends upon the amount of fuel that has already been injected, which is related to the length of the ignition delay. With shorter ignition delays (related to high cetane number), less fuel is injected and mixed with air before ignition occurs, thus leading to moderate temperature and pressure increases. This ignition delay dependence of specific $NO_X$ explains the trends in most of the cases considered here.

Table 6.1. Specific $NO_X$ and Specific HC variation in different dual fuelling cases with different pilot fuels

| Case Description | Specific $NO_X$ | Specific HC |
|---|---|---|
| D-1-NG-1000 | 15%↑ | 59%↓ |
| D-2-NG-1000 | 7%↑ | 22%↓ |
| D-3-NG-1000 | 7%↑ | 26%↓ |
| RME-1-NG-1000 | 3.5%↓ | 32%↓ |
| RME-2-NG-1000 | 1.5%↓ | 38%↓ |
| RME-3-NG-1000 | 4%↓ | 40%↓ |
| D-1-NG-1500 | 26%↑ | 54%↓ |
| D-2-NG-1500 | 9%↑ | 30%↓ |
| D-3-NG-1500 | 4.5%↑ | 27%↓ |
| RME-1-NG-1500 | 15%↑ | 44%↓ |
| RME-2-NG-1500 | 6.5%↑ | 28%↓ |
| RME-3-NG-1500 | 1.5%↑ | 34%↓ |

### 6.2.3 Specific HC

Figures 6.5(a) and 6.5(b) show specific HC emissions for diesel and RME piloted combustion of natural gas at 1000 rev/min and 1500 rev/min respectively. For diesel piloted natural gas combustion at 1000 rev/min, any increase in pilot fuel quantity has resulted in lower specific HC emissions. The highest load condition where the minimum pilot fuel setting (n=1) have produced lower specific HC as compared to the middle pilot fuel setting (n=2)is the only exception to the above mentioned trend. This is consistent with

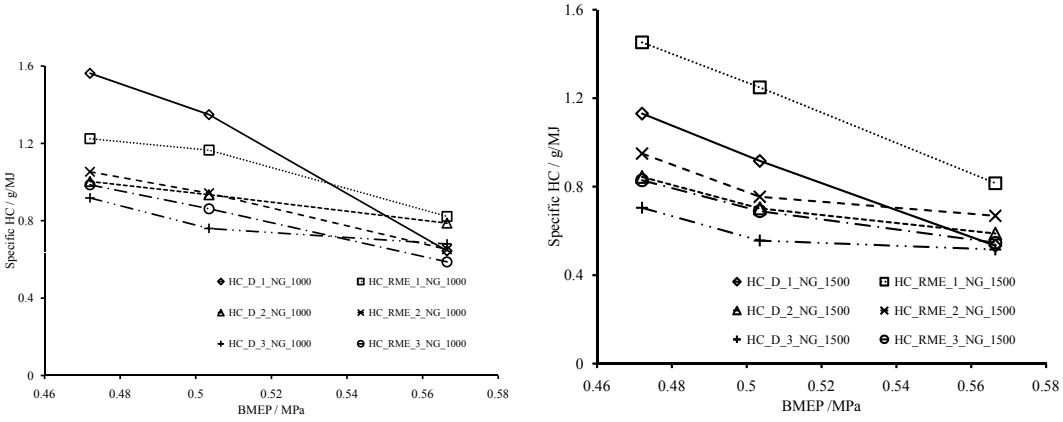


(a) Specific HC for natural gas combustion with three different diesel pilot and RME pilot fuel settings at 1000 rev/min

(b) Specific HC for natural gas combustion with three different diesel pilot and RME pilot settings at 1500 rev/min

Figure 6.5. Effect of pilot fuel quantity and type on specific HC emissions at 1000 rev/min (a) and 1500 rev/min (b)

the trends obtained in specific $NO_X$ emissions as the minimum pilot fuel setting produced higher $NO_X$ at the highest load so that it resulted in minimum specific HC emissions at the same operating conditions. Apart from the lowest pilot fuel setting (n=1), the specific HC emissions vary in very small range. This suggests that when the pilot fuel is set constant at a relatively lower value of BMEP, a significant portion of the fuel escapes unburnt as the pilot fuel fails to provide enough ignition sites to launch natural gas combustion. A comparable (or even lower) value of specific HC emission at the highest load when the pilot is set at a minimum BMEP can be attributed to a relatively higher in-cylinder temperature.

This relatively higher in-cylinder temperature can ensure timely evaporation of the pilot fuel and hence better distribution of the ignition centers across the charge.

At 1000 rev/min, RME piloted combustion of natural gas has generally produced lower levels of specific HC emissions when compared to the diesel piloted combustion of natural gas. The highest load condition is the only exception to this trend where diesel piloted natural gas combustion has resulted in lower specific HC numbers for similar operating conditions.

At 1500 rev/min, the specific HC have shown similar trends as observed at 1000 rev/min. The only exception is when RME is used to pilot the natural gas combustion with pilot fuel set at a minimum BMEP value (n=1). RME-1-NG-1500 case has produced higher levels of HC at all operating condition when compared to all other five cases. This can be attributed to poor atomization characteristics of RME which become more evident at lower pilot fuel setting. When the pilot fuel is set at a minimum BMEP value, there is more natural gas present in the combustion chamber. As natural gas has higher heat capacity value, it shall result in a lower temperature charge which can further deteriorate the atomization problems with RME. The effect is more pronounced at higher speed as there is less residence time available at higher speeds. With diesel as pilot fuel at 1000 rev/min, the ignition delay decreased initially as the quantity of pilot fuel was increased and then stayed constant for any further decrease. On the other hand, at 1500 rev/min, a gradual decrease in ignition delay was observed when the quantity of pilot fuel was increased. With RME as a pilot fuel, the ignition delay decreased slightly and then stayed the same as the quantity of pilot fuel was increased. This trend was exhibited at both speeds. Considering the diesel piloted natural combustion at the peak load conditions at 1000 rev/min, lower specific HC emission resulted when the ignition delay was shortened. A shorter ignition delay can afford the fuel mixture and the initial combustion products to have longer residence time at temperature, thereby reducing the specific HC emissions. At 1500 rev/min for similar fuel and operating conditions combination; the ignition delay showed a different trend as

it decreased gradually as the quantity of pilot fuel increased. This can be attributed to greater magnitude of vortices of turbulence at higher engine rev/min helping to achieve better mixing and an early start of ignition and hence a greater reduction in specific HC values. Like specific $NO_X$, specific HC emissions from diesel and RME piloted combustion of natural gas also exhibit the pilot fuel quantity threshold phenomenon. At lower speeds, the specific HC emissions decrease as the quantity of pilot fuel is increased whereas at higher speeds, there exists a pilot fuel quantity threshold below or above which the specific HC emissions increase. Also, at relatively lower values of BMEP, the specific HC emissions vary significantly and the trend lines converge as BMEP is increased. This confirms that higher temperatures at higher BMEP values make better use of the pilot fuel.

### 6.2.4 Specific $CO_2$ and CO

Figures 6.6(a) and 6.6(b) show specific $CO_2$ emissions and figures 6.7(a) and 6.7(b) show specific CO emissions for diesel and RME piloted combustion of natural gas at 1000 rev/min and 1500 rev/min respectively. While operating at 1000 rev/min, specific $CO_2$ emission showed little variation across all BMEP values and the different fuel combination cases. The highest $CO_2$ magnitudes were recorded when RME piloted the natural gas combustion at medium (n=2) pilot fuel setting (RME-2-NG-1000). For all other five cases, the specific $CO_2$ range was 50 g/MJ. More carbon is being inducted as the BMEP value increases and it results in higher absolute $CO_2$ numbers. The drop in specific $CO_2$ can be attributed to the fact that there is more power being delivered at higher BMEP values which causes a drop in specific $CO_2$ numbers. At 1000 rev/min, maximum specific $CO_2$ emissions were obtained with the highest pilot fuel setting (n=3) followed by the medium pilot setting (n=2) and then the lowest pilot fuel setting (n=3) respectively.

At 1000 rev/min, RME piloted combustion of natural gas exhibited different order in which the specific $CO_2$ trend lines appear for the three cases involved when compared to the diesel piloted three cases of natural gas combustion. The highest specific $CO_2$ numbers

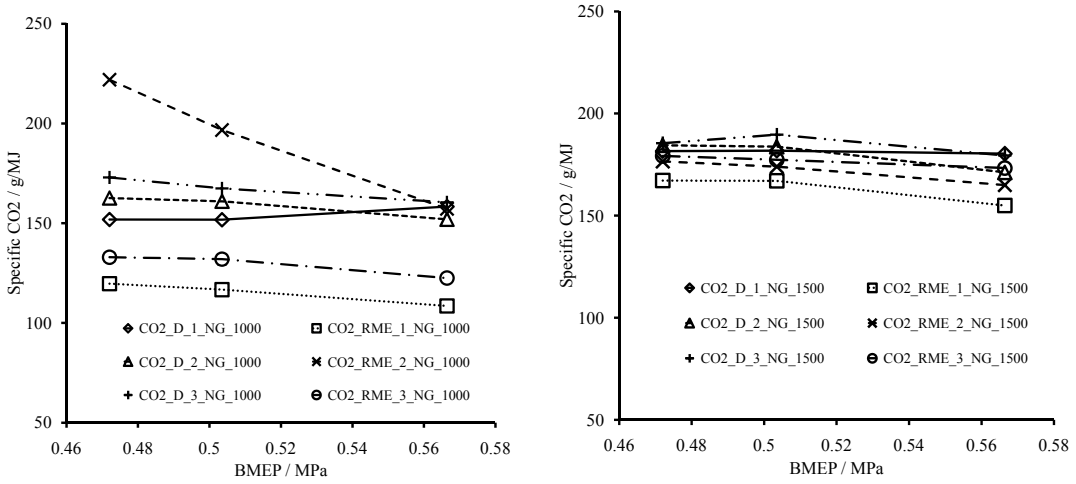


(a) Specific $CO_2$ for natural gas combustion with three different diesel pilot and RME pilot fuel settings at 1000 rev/min

(b) Specific $CO_2$ for natural gas combustion with three different diesel pilot and RME pilot settings at 1500 rev/min

Figure 6.6. Effect of pilot fuel quantity and type on specific $CO_2$ emissions at 1000 rev/min (a) and 1500 rev/min (b)

were obtained at medium pilot fuel setting (n=2) followed by the highest (n=3) and the lowest pilot fuel setting (n=1) respectively. At 1500 rev/min, the specific $CO_2$ exhibited similar trends as recorded at 1000 rev/min i.e. a small decrease in $CO_2$ numbers as the BMEP is increased. The range of the specific $CO_2$ numbers was even smaller, 30 g/MJ against 113 g/MJ at 1000 rev/min across all six fuel combinations. Interestingly, for RME piloted combustion of natural gas , the order in which the trend lines of the specific $CO_2$ emissions appear at 1500 rev/min was reversed for the two higher pilot fuel settings (n=2,3) when compared to what was obtained at 1000 rev/min. For both the diesel as well as RME piloted cases, the specific $CO_2$ numbers have increased as the quantity of the pilot fuel was increased. The highest load setting with diesel piloted natural gas combustion was the only exception to this trend.

At 1000 rev/min, specific CO have shown sharp decrease with any increase in BMEP when compared to the $CO_2$ trends across all fuel combinations at similar operating condi-

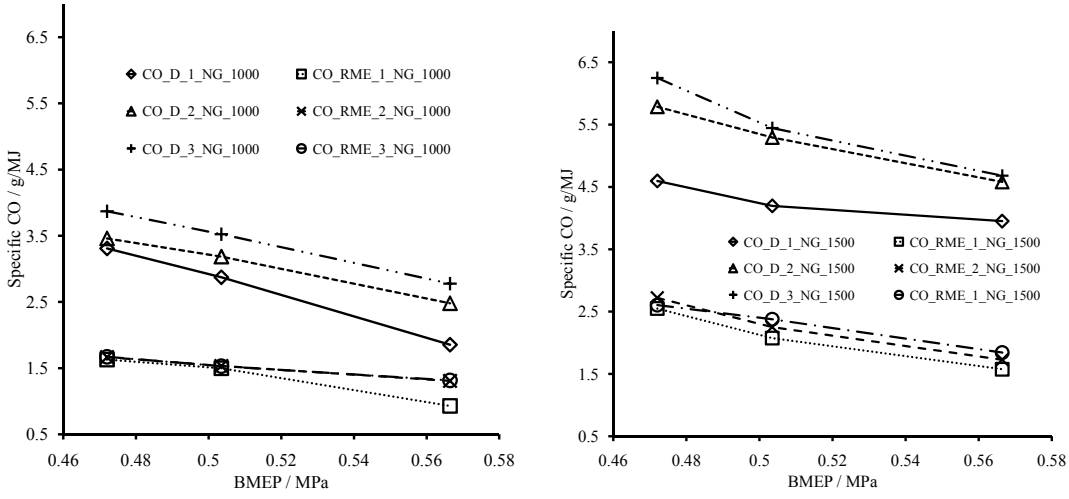


(a) Specific CO for natural gas combustion with three different diesel pilot and RME pilot fuel settings at 1000 rev/min

(b) Specific CO for natural gas combustion with three different diesel pilot and RME pilot settings at 1500 rev/min

Figure 6.7. Effect of pilot fuel quantity and type on specific CO emissions at 1000 rev/min (a) and 1500 rev/min (b)

tions.

This can be attributed to the fact that any increase in BMEP while operating at a constant speed shall result in higher absolute $CO_2$ and lower CO numbers due to higher in-cylinder temperature and better combustion quality. Absolute numbers for CO emissions decrease and the power output increases as the BMEP is increased. These two trends together cause a sharp drop in specific CO emissions. At 1000 rev/min for diesel piloted combustion of natural gas, the specific CO numbers have increased as the quantity of pilot was increased. For RME piloted combustion of natural gas, no significant change has been observed in specific CO emissions as the quantity of the pilot fuel was changed. Overall lower specific CO numbers were achieved when RME was used as a pilot fuel at 1000 rev/min. At 1500 rev/min, the specific CO emissions have exhibited similar trends as observed at 1000 rev/min. For both of the pilot fuels, any increase in pilot fuel quantity has resulted in increased levels of CO emissions. The range of specific CO emissions is very

small with RME (1.14 g/MJ) as compared to the one obtained with diesel as pilot (2.29 g/MJ).

## 6.3 RESULTS AND DISCUSSION - HYDROGEN

This section is further divided into two parts. The first part discusses the implications of the change in the pilot fuel quantity and type on in-cylinder pressure, rate of energy release and ignition delay. The second part discusses the effect of change in the pilot fuel quantity and type and engine speed on different emissions.

### 6.3.1 Ignition Delay and Pressure Data

Figure 6.8 shows the effect of the pilot fuel quantity , type and the engine speed on the ignition delay of different cases of hydrogen dual fueling piloted by either diesel or RME. Compared to the respective diesel or RME based single fueling, the diesel and RME piloted combustion of hydrogen has shown longer ignition delays for all combinations of the pilot fuel quantity, type and engine speed. When the three diesel piloted hydrogen dual fueling

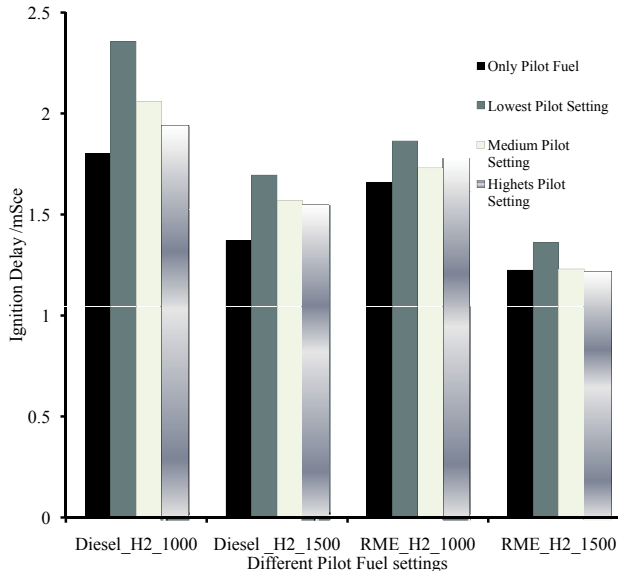


Figure 6.8. Effect of Pilot Fuel Quantity on ignition delay for different pilot fuel settings in diesel and RME piloted combustion of Hydrogen at 1000 rev/min and 1500 rev/min

cases are compared with each other, the ignition delay was shortened as the quantity of pilot fuel was increased. Relatively smaller difference was observed in terms of ignition delays for the two higher pilot fuel settings (n=2,3) at 1500 rev/min. Greater number of ignition centers when the pilot fuel is set at a higher BMEP (n=2 or 3) value (or when the energy contribution from the hydrogen is lower) causes the ignition delay to be shortened as more ignition sites are available to ignite the available amount of hydrogen. This can explain the difference between different ignition delay values for the different cases especially between the lowest pilot fuel setting and the two higher settings. Smaller difference between the higher pilot fuel setting cases can be attributed to smaller variation in ignition energy for hydrogen.

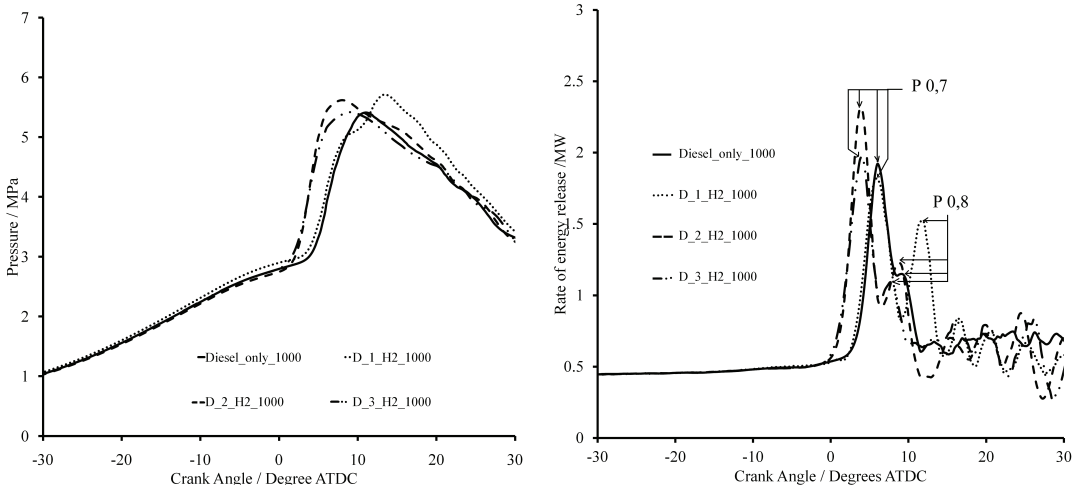


(a) Cylinder Pressure for pure diesel and three cases of hydrogen combustion with different diesel pilot fuel settings at a BMEP of 0.44 MPa and 1000 rev/min

(b) Rate of energy release for pure diesel and three cases of hydrogen combustion with different diesel pilot fuel settings at a BMEP of 0.44 MPa and 1000 rev/min

Figure 6.9. Effect of the pilot fuel quantity and type on in-cylinder pressure 6.9(a) and rate of energy release 6.9(b) for pure diesel and three cases of hydrogen with different diesel pilot fuel settings at a BMEP of 0.44 MPa and 1500 rev/min

Similar ignition delays in case of the two higher pilot fuel settings suggest that if the

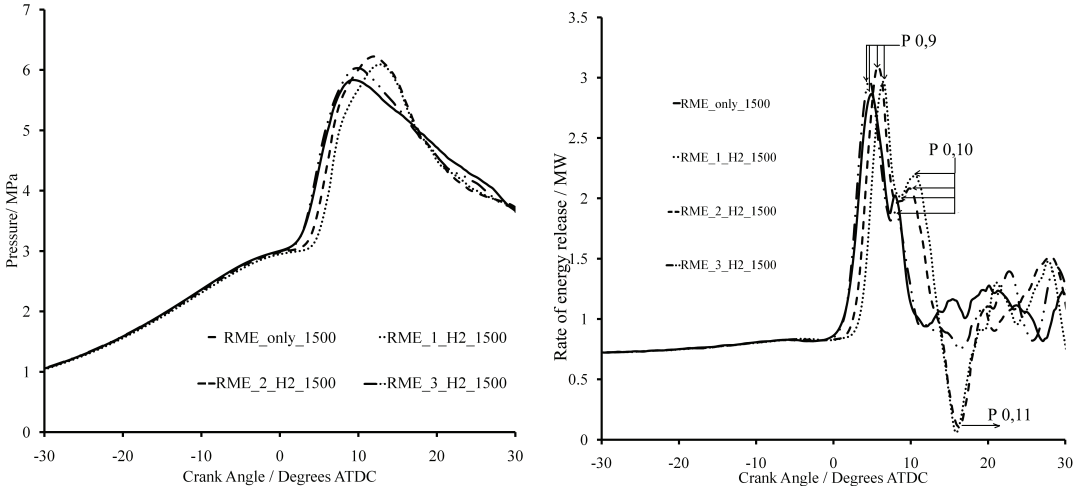


(a) Cylinder Pressure for pure RME and three cases of hydrogen combustion with different RME pilot fuel settings at a BMEP of 0.44 MPa and 1500 rev/min

(b) Rate of energy release for pure RME and three cases of hydrogen combustion with different RME pilot fuel settings at a BMEP of 0.44 MPa and 1500 rev/min

Figure 6.10. Effect of the pilot fuel quantity and type on in-cylinder pressure 6.10(a) and rate of energy release 6.10(b)for pure RME and three cases of hydrogen combustion with different RME pilot fuel settings at a BMEP of 0.503 MPa and 1000 rev/min

quantity of pilot fuel is set at a BMEP higher than a certain value, the ignition delay will not be affected significantly. At 1500 rev/min, the RME piloted dual fueling of natural gas exhibits trends similar to the diesel piloted dual fueling of the natural gas; shortening of the ignition delay as the quantity of pilot fuel was increased. At 1000 rev/min, the RME piloted dual fueling of natural has deviated from the trend observed for the rest of the combinations. When compared to the highest pilot fuel setting (n=3), the medium pilot fuel setting (n=2) exhibited relatively shorter ignition delay. This can be attributed to the poor atomization characteristics of the RME which become more evident at lower speeds due to relatively lower levels of in-cylinder turbulence.

Figures 6.9(a) and 6.9(b) show the in-cylinder pressure and the corresponding rate of energy release plotted against the crank angle for pure diesel and the three cases of diesel

piloted combustion of natural gas at 1000 rev/min.

In figure 6.9(b), the first peak in the rate of energy release diagram for the diesel piloted dual fueling of natural gas at 1000 rev/min is indicated by point ($P_{0,7}$) whereas the points ($P_{0,8}$) indicates the second peak. When the diesel pilot was set at the minimum BMEP value (n=1), two very distinct peaks were observed. The first peak in the rate of energy release diagram for this case occurred at 5.95° CA ATDC which was similar to the diesel based single fueling. There was another very obvious peak observed at 12° CA ATDC. The first peak in the rate of energy release diagram for the two higher diesel pilot settings (n=2,3) occurred at 3.9° CA ATDC. The second peak in the rate of energy release diagram for these two (n=2,3) cases occurred at 7.5° CA ATDC and 9.0° CA ATDC respectively. The medium setting (n=2) of the pilot fuel for the diesel piloted dual fueling of hydrogen produced higher first as well as the second peaks when compared to the highest pilot fuel setting. The medium pilot fuel setting for the diesel piloted dual fueling of hydrogen exhibited the highest first peak when compared to all other diesel piloted dual fueling cases.

At 1500 rev/min when compared to pure diesel base case, all diesel piloted hydrogen combustion cases have shown shorter ignition delay and higher peak cylinder pressure and higher rate of pressure rise. Relatively smaller difference was observed in terms of ignition delays for the two higher pilot fuel settings (n=2,3) but the medium (n=2) pilot fuel setting case showed the highest peak pressure. The lowest pilot fuel setting, when the amount of hydrogen was maximum, showed the longest ignition delay but the peak pressure in this case was comparable to the maximum pressure obtained for the case n=2. Also the occurrence of the peak pressure for the lowest pilot fuel quantity was delayed proportional to the ignition delay when compared to the other cases with diesel piloted combustion of hydrogen. Similar ignition delays but different peak pressures in case of the two higher pilot fuel settings suggest that if the quantity of pilot fuel is set at a BMEP higher than a certain value, neither ignition delay will be shortened nor a higher peak pressure will be achieved. A higher peak pressure with the lowest pilot fuel setting can

be attributed to different combustion properties of hydrogen as a fuel. Higher flame speed and shorter quenching distances seem to play vital role as more hydrogen is present inside the combustion chamber so the combustion can occur near the relatively colder cylinder walls as well due to short quenching distances. Maximum quantity of hydrogen is inducted when the pilot fuel is set at the lowest BMEP (n=1). A higher second peak for the rate of energy release for the lowest pilot fuel setting (n=1) suggests that for the for this particular setting, the hydrogen is burning in two different phases. In the first phase, it is the diesel-air mixture which gets oxidized along with a small quantity of hydrogen. In the second phase, the bulk of hydrogen is burnt.

Figures 6.10(a) and 6.10(b) show the in-cylinder pressure and the corresponding rate of energy release plotted against the crank angle for pure RME and the three cases of RME piloted combustion of natural gas at 1500 rev/min. When compared to diesel piloted combustion of hydrogen at 1000 rev/min, RME piloted combustion of hydrogen at 1500 rev/min exhibit different trends when the pressure traces of the two modes are compared. The medium pilot fuel quantity setting (n=2) produced the maximum pressure followed by n=1 and n=3 respectively. The comparable peak pressure for the lowest pilot fuel setting when compared to the middle pilot fuel setting (n=2) when RME piloted the hydrogen combustion can be explained on the similar grounds as presented for the similar condition with diesel piloted hydrogen at 1500 rev/min.

In figure 6.10(b), the first peak is the rate of energy release diagram for the diesel piloted dual fueling of hydrogen at 1000 rev/min is indicated by point ($P_{0,9}$) whereas the point ($P_{0,10}$) indicates the second peak for the rate of energy release. The first peak for the rate of energy release is the highest for the medium pilot fuel setting (n=2) when compared to all other RME piloted hydrogen dual fueling cases hydrogen. It occurs at 5.7° CA ATDC. As the RME pilot fuel quantity was increased, the occurrence of the first rate of energy release peak is delayed. It occurs at 4.5° CA ATDC for the highest pilot fuel quantity whereas at 6.5° CA ATDC, the lowest pilot fuel setting shows a relatively more

clear second peak at 10.67° CA ATDC when compared to all other cases of RME piloted dual fueling of hydrogen.

### 6.3.2 Specific $NO_X$

Figures 6.11(a) and 6.11(b) show specific $No_X$ emissions for diesel and RME piloted combustion of natural gas at 1500 rev/min and 1000 rev/min respectively. At 1000 rev/min when RME pilots hydrogen combustion figure 6.11(a), there is clear decrease in specific $NO_X$ numbers as the quantity of pilot fuel is increased. For a particular pilot fuels setting, any increase in BMEP resulted in higher specific $NO_X$ for all cases. The three cases with RME as pilot fuel resulted in comparable levels of specific $NO_X$ when compared to the cases with diesel as pilot fuel at similar conditions. For the lowest pilot fuel setting (n=1), higher rate of increase in $NO_X$ was recorded when compared to relative higher pilot fuel settings (n=2,3). This was held for both RME as well as diesel piloted hydrogen combustion cases at 1000 rev/min. Higher specific $NO_X$ at higher BMEP values can be attributed to higher in-cylinder temperature as the engine is running hotter due to more fuel being injected to meet the higher power requirement. The larger gradient of specific $NO_X$ at lowest pilot fuel setting (n=1) could be a result of more hydrogen being inducted at these conditions. Maximum ignition delay was observed when the pilot fuel quantity was set at the minimum so more pilot fuel was injected during this delay period and results in higher temperature and pressure. With longer residence time more fuel is injected and mixed with air before ignition occurs and this explains the higher in-cylinder temperature. Increasing the quantity of pilot fuel has lowered the ignition delay. The specific $NO_X$ seem to be more affected by the quantity of hydrogen being inducted at a particular condition. Lower ignition energy and short quenching distances for hydrogen combustion suggest that it may not depend strongly upon the initial source of ignition to achieve sustainable combustion. The flame travels faster through hydrogen and hence the initial source of ignition becomes irrelevant very quickly. This explains the higher specific $NO_X$ for lower pilot fuel setting case when

the hydrogen quantity was maximum.

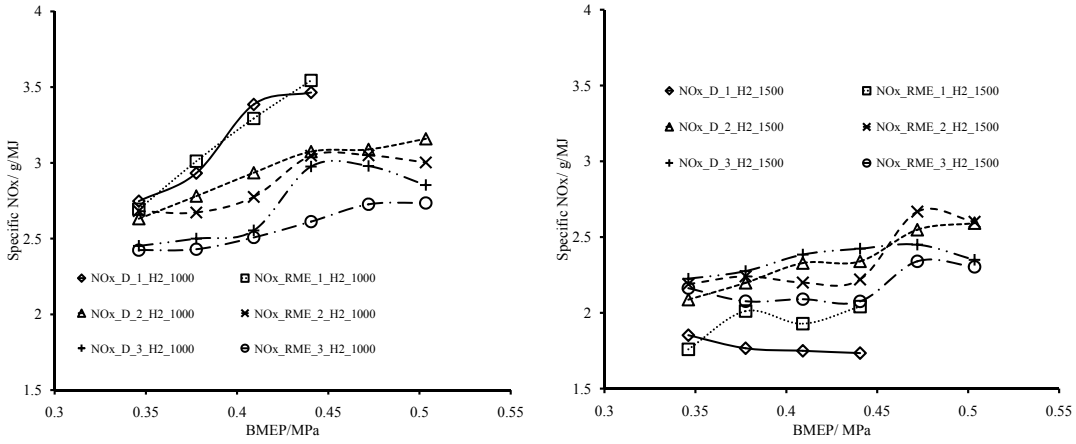


(a) Specific $NO_X$ for hydrogen combustion with three different diesel pilot and RME pilot fuel settings at 1000 rev/min

(b) Specific $NO_X$ for hydrogen combustion with three different diesel pilot and RME pilot settings at 1500 rev/min

Figure 6.11. Effect of pilot fuel quantity and type on specific $NO_X$ emissions at 1000 rev/min (a) and 1500 rev/min (b)

At 1500 rev/min, the specific $NO_X$ produced by diesel piloted hydrogen combustion exhibits different trends to what is observed at lower speed (1000 rev/min in this case). There is a complete reversal of the orders of the magnitude of the specific $NO_X$ for different cases at these two conditions. At 1500 rev/min, the minimum pilot fuel quantity (n=1) has produced the lowest specific $NO_X$ and these emissions have increased as the quantity of pilot fuel is increased. This trend holds good for the three diesel based cases apart from the highest BMEP value where the two higher pilot fuel settings swap their trends. For the lowest pilot fuel setting, specific $NO_X$ are not only lower in magnitude but also vary differently with any change in the BMEP value when compared to the trends observed at 1000 rev/min. Increase in BMEP value has caused the diesel piloted hydrogen specific $NO_X$ to decrease slightly. For the two higher pilot fuel settings, the specific $NO_X$ exhibit similar trend as observed at 1000 rev/min, although the emissions are lower in magnitude when compared diesel piloted hydrogen combustion $NO_X$ at 1000 rev/min. A larger ignition

delay is observed with the lowest pilot fuel setting as was the case at 1000 rev/min, but the higher engine speed seems to counter the effect of longer ignition delay. With longer ignition delays, more fuel is supplied during the delay period and causes higher combustion temperature and pressure. At higher speeds the effective residence time is reduced resulting in relatively milder combustion pressure and temperature. The pressure and rate of energy release curves for RME piloted combustion of hydrogen at 1500 rev/min (figures 6.10(a) and 6.10(b)) seem to support this argument. In diesel piloted combustion of hydrogen where the lowest pilot fuel setting (n=1) showed higher maximum in-cylinder pressure and a very strong second rate of energy release peak (point $P_{0,8}$ in figure 6.9(b) when compared to the two higher pilot fuel setting cases (n=2,3), in contrast, with RME piloted combustion of hydrogen at 1500 rev/min, all three pilot fuel settings show similar peak cylinder pressure and the second rate of energy release peak for the lowest pilot fuel quantity is also less strong (point $P_{0,10}$ in figure 6.10(b). Hydrogen combustion characteristics ( shorter quenching distances, faster flame speeds and smaller variation in ignition energy that helped the lowest pilot fuel settings case at 1000 rev/min exhibit maximum peak cylinder pressure ) seem to be downplayed by this shorter residence at higher engine rev/min. Although the turbulence levels are increased at higher engine rev/min, but the smaller residence time at these conditions seems to dominate combustion phenomenon. The variation in specific $NO_X$ with different pilot fuel setting cases can also be explained on this basis. When the ignition is delayed and overall residence is shortened, it results in relatively lower combustion peak pressure and temperature and hence lower specific $NO_X$. For the lowest pilot fuel setting, RME piloted combustion of hydrogen has produced higher $NO_X$ as compared to the diesel piloted combustion of hydrogen. The trend is reversed for the highest pilot fuel setting. For the medium pilot fuel setting , the specific $NO_X$ are comparable for both of the cases. This can be attributed to relatively poor injection and atomization characteristics of RME, which become more evident as the combustible mixture become relatively more RME-enriched and a shorter residence time.

### 6.3.3 Specific HC

Figures 6.12(a) and 6.12(b) show specific HC emissions for diesel and RME piloted combustion of natural gas at 1000 rev/min and 1500 rev/min respectively. While operating at 1000 rev/min, the diesel and RME piloted hydrogen combustion resulted in sharp decrease in specific HC emissions before an increase is observed at the highest BMEP. For the lowest pilot fuel setting (n=1), RME and diesel piloted combustion of hydrogen produced similar trends with the diesel piloted case producing higher specific HC numbers for range of BMEP in investigation. The three diesel cases have produced comparable specific HC emissions apart from the BMEP value where the lowest pilot fuel setting has increased. For the lowest pilot fuel setting, the increase in specific HC numbers is consistent with a drop in specific $NO_X$ at the same condition for this case. This can be attributed to some part of the pilot fuel escaping the combustion event due to lack of oxygen and lower turbulence levels in the combustion chamber at higher BMEP values. Another valid observation would be to consider the range of specific HC emissions for the diesel and RME piloted combustion. It is 0.1g/MJ for diesel and 0.22 g/MJ for RME piloted combustion $H_2$ across all values of BMEP. Generally lower values of specific HC emissions with lower pilot fuel setting can be attributed to the fact that there are no specific HC emissions from $H_2$ combustion. These specific HC emissions result from the combustion of the pilot fuel and hence are proportional to the pilot fuel quantity. At 1500 rev/min the specific HC emissions are decreased when there is any increase in BMEP apart from the lowest pilot fuel setting with diesel piloted hydrogen combustion. For diesel piloted hydrogen combustion cases, the specific HC emissions decreased as the quantity of pilot fuel was increased. The reasons presented to explain higher specific $NO_X$ with higher pilot fuel setting hold for lower specific HC emissions with higher pilot fuel setting. As observed at 1000 rev/min, the diesel piloted combustion of hydrogen produce higher specific HC emissions when compared RME piloted combustion of hydrogen.

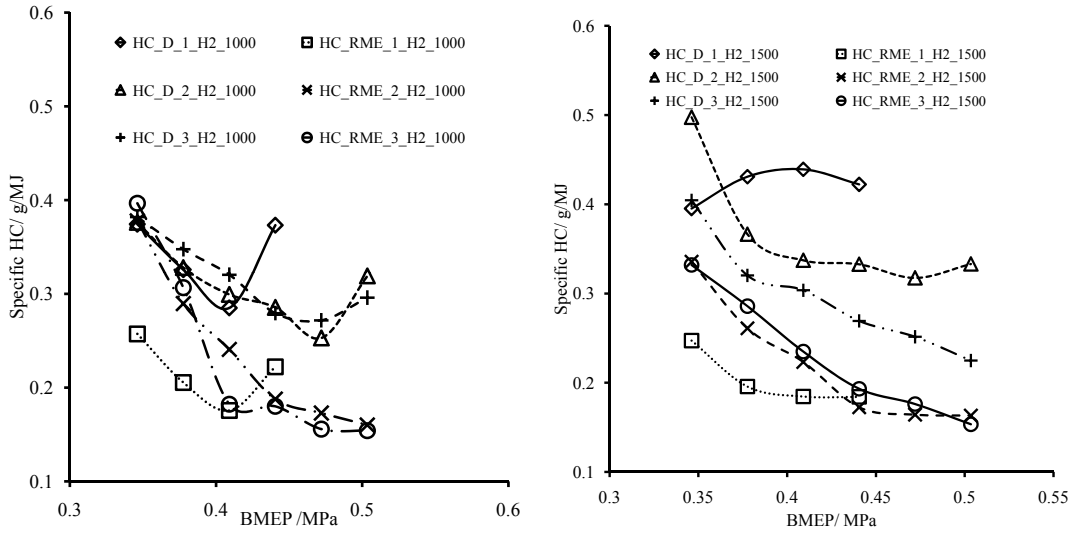


(a) Specific HC for hydrogen combustion with three different diesel pilot and RME pilot fuel settings at 1000 rev/min

(b) Specific HC for hydrogen combustion with three different diesel pilot and RME pilot settings at 1500 rev/min

Figure 6.12. Effect of pilot fuel quantity and type on specific HC emissions at 1000 rev/min (a) and 1500 rev/min (b)

### 6.3.4 Specific $CO_2$ and CO

Figures 6.13(a) and 6.13(b) show specific $CO_2$ emissions and figures 6.14(a) and 6.14(b) show specific CO emissions for diesel and RME piloted combustion of hydrogen at 1000 rev/min and 1500 rev/min respectively. For hydrogen based dual fueling cases piloted by either diesel or RME, the quantity of pilot fuel is critical to specific HC, CO and $CO_2$ emissions as there is no extra carbon going into the combustion chamber when hydrogen is inducted after the quantity of pilot is fixed at a certain BMEP value. At 1000 rev/min, any increase in BMEP has resulted in lower specific $CO_2$. This can be attributed to better combustion of the pilot fuel being injected at higher BMEP values as the engine is operating at higher temperature. Also, the amount of carbon going into the combustion chamber is constant at the BMEP where the pilot fuel quantity is fixed, but the power produced by the engine is increasing as the BMEP is increased. The specific $CO_2$ produced

by RME piloted combustion of hydrogen are comparable to what is obtained with diesel piloted combustion of hydrogen at similar conditions. The specific $CO_2$ offset observed for different pilot fuel quantity cases is proportional to the quantity of the pilot fuel and this holds good for both of the pilot fuels. At 1500 rev/min, the specific $CO_2$ trends seem similar to what is observed at 1000 rev/min although a bit less linear with any change in BMEP values. Higher specific $CO_2$ were as observed the quantity of pilot fuel was set at a relatively higher BMEP value. This trend can be explained on similar grounds as presented for different cases at 1000 rev/min. At 1000 rev/min, the levels of specific $CO_2$ for RME

| case description | $n_1$ | $n_2$ | $n_3$ |
|---|---|---|---|
| Diesel-$H_2$-1000 | 0.4 | 1.45 | 1.23 |
| Diesel-$H_2$-1500 | 0.836 | 1.77 | 3.91 |
| RME-$H_2 - 1000$ | 3.4 | 6.23 | 6.29 |
| RME-$H_2 - 1500$ | 4.11 | 5.95 | 5.43 |

Table 6.2. Range of specific CO emissions /g/MJ from diesel and RME piloted hydrogen dual fueling for different pilot fuel settings at two different engine speeds

piloted combustion of hydrogen were comparable to diesel piloted combustion of hydrogen but RME piloted cases have produced lower specific $CO_2$ when compared to diesel piloted respective cases at 1500 rev/min. The Lower carbon to hydrogen ratio of RME when compared to diesel seems to become more evident at higher engine rev/min. Like specific $CO_2$ emissions, specific CO emissions are lowered as BMEP is increased and this can be attributed to better combustion and the higher power produced at higher BMEP values. Unlike the specific $CO_2$ emissions where comparable levels of the emissions were obtained for both diesel and RME piloted combustion of hydrogen, the specific CO emissions form diesel and RME piloted hydrogen combustion have different regions of occurrence on the graph of specific CO plotted against BMEP. Although the specific CO emissions increased

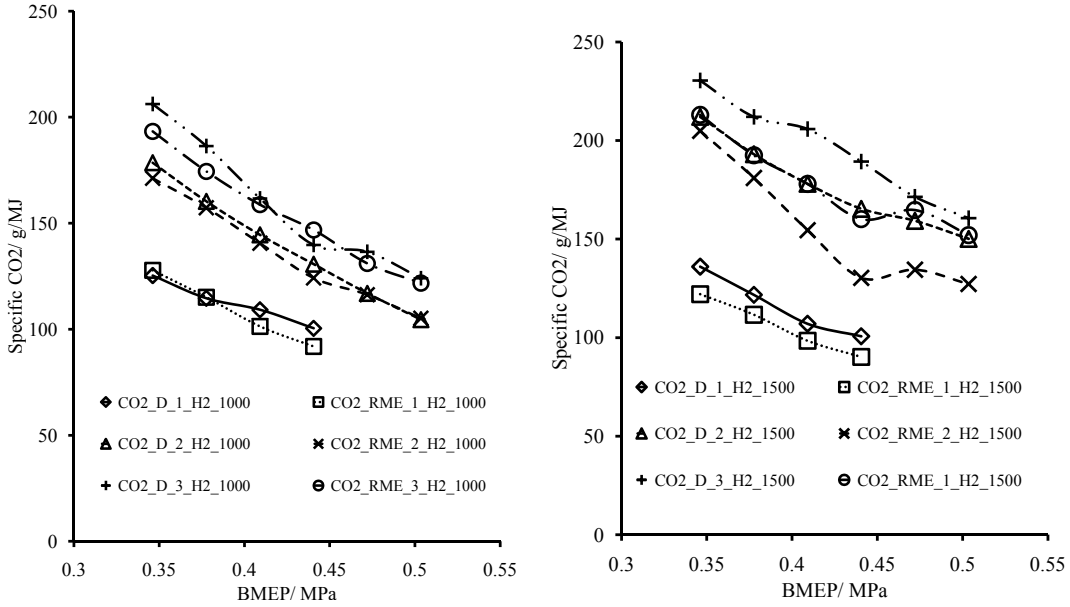


(a) Specific $CO_2$ for hydrogen combustion with three different diesel pilot and RME pilot fuel settings at 1000 rev/min

(b) Specific $CO_2$ for hydrogen combustion with three different diesel pilot and RME pilot settings at 1500 rev/min

Figure 6.13. Effect of pilot fuel quantity and type on specific $CO_2$ emissions at 1000 rev/min (a) and 1500 rev/min (b)

as the quantity of pilot fuel was increased. The increase in specific CO emissions is not proportional to the quantity of the pilot fuel which was a case with specific $CO_2$ emissions at similar conditions. The specific CO emissions do not seem to change for a certain pilot fuel setting as the BMEP value is changed. The range of specific CO emissions for diesel piloted hydrogen combustion for different pilot fuel settings has been presented in a two way table 6.3.4. For all three cases of diesel piloted dual fueling of hydrogen, the variation in specific CO emissions is small. The higher range of specific CO emissions for RME piloted dual fueling of hydrogen can be attributed to RME's poor atomization characteristics.

At 1500 rev/min, specific CO emissions were lowered when there was any increase in BMEP. This trend is similar to what is obtained at 1000 rev/min but higher levels of the specific CO emissions were obtained at 1500 rev/min for diesel piloted combustion

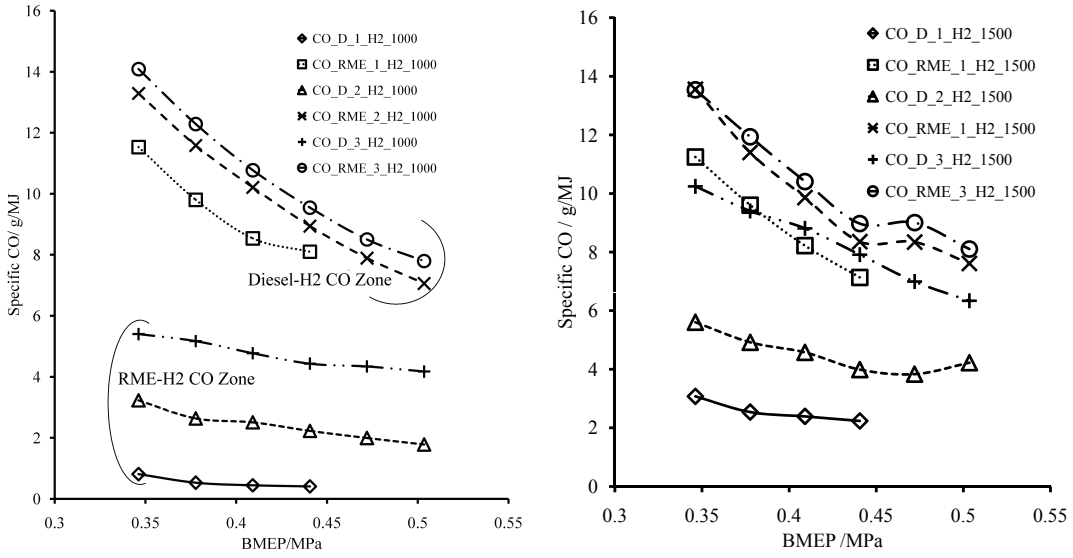


(a) Specific CO for hydrogen combustion with three different diesel pilot and RME pilot fuel settings at 1000 rev/min

(b) Specific CO for hydrogen combustion with three different diesel pilot and RME pilot settings at 1500 rev/min

Figure 6.14. Effect of pilot fuel quantity and type on specific CO emissions at 1000 rev/min (a) and 1500 rev/min (b)

of hydrogen. Also, the specific CO emissions from diesel piloted hydrogen combustion for different pilot fuel settings are no more concentrated to a specific region as observed at 1000 rev/min and the highest pilot fuel setting with diesel has yielded specific CO emissions comparable to what is obtained with different pilot fuel settings with RME. Higher range of specific CO emissions for the highest pilot fueling setting for diesel piloted hydrogen combustion can be attributed to the fact that more pilot fuel is being injected and the residence time is reduced due to higher engine speed.

## 6.4 CHAPTER SUMMARY

Natural gas and hydrogen have been extensively tested in dual fuel mode in a compression ignition engine. A high cetane number liquid fuel (mostly diesel or a biodiesel) is used as an initial source of ignition for the two gaseous fuels which are hard to ignite under

normal CI conditions. Many studies conclude that the emissions especially $NO_X$ resulting from these dual fueling cases are expected to form in the region around the pilot spray where high temperatures exist and the equivalence ratio is close to stoichiometric but the effect of changing the pilot fuel quantity has been hardly reported. This study investigates the effect of changing pilot fuel quantity and type and assess the effect of this change on various combustion and emission parameters. Diesel and RME have been used as pilot fuels for both the natural gas as well as hydrogen and three different pilot fuel settings have been employed for each of the gaseous fuels. The effect of using a different pilot fuel quantity of diesel and RME to achieve the same BMEP for the two gaseous fuel has been analysed and compared. The study was conducted at two engine speeds to assess the effect of engine speed variation on different combustion and emissions parameters. Dual fueling of natural gas and hydrogen exhibit an increased ignition delay when compared to the ignition delay exhibited by the pilot fuel at similar operating conditions. For dual fueling cases, the ignition delay is reduced as the quantity of pilot fuel is increased. For both diesel as well as RME piloted combustion of natural gas at higher speeds, the specific $NO_X$ have been generally found proportional to the quantity of pilot fuel. At lower speeds, there exists a pilot fuel quantity threshold where maximum specific $NO_X$ are produced and any pilot fuel setting below or above the threshold shall result in lower specific $NO_X$. For diesel as well as RME piloted hydrogen combustion, the ignition delay is shortened as the quantity of pilot fuel increased but the peak cylinder pressure does not seem to be a very strong function of this ignition delay in hydrogen dual fueling as similar peak pressure is achieved even when the pilot fuel is set at a minimum BMEP.

# CHAPTER 7

# COMPUTATIONAL PREDICTION OF IN-CYLINDER PRESSURE, RATE OF ENERGY RELEASE AND ENGINE EMISSIONS

### 7.0.1 Finite Rate Chemistry and Unsteady Flamelet Approaches

The finite rate chemistry approach computes the chemical source term using Arhenius expressions. It ignores the effects of turbulence fluctuations. The model is exact for laminar flames but is generally applied to the situations where there is small chemistry - turbulence interactions. The net source of chemical species due to reaction is computed as the sum of the Arrhenius reaction sources over all the reactions that the species participate in [126]. The unsteady flamelet approach achieves significant reduction in calculation time when compared to the finite rate chemistry approach. This model solves the flamelet species and energy equations simultaneously with flow equation. The flamelet equations are advanced for a fractional step using properties from the flow, and then the flow is advanced for the same fractional time-step using properties from the flamelet [126]. The initial flamelet distribution is mixed but unburnt. The volume-averaged scalar dissipation, pressure, temperatures of the fuel and oxidizer are passed from the flow solver to the flamelet solver for the fractional time step solver. The rise in flamelet temperature due to compression leads towards ignition. After the flamelet equations have been advanced for the fractional time-step, the PDF table is created. Using the properties of this table, the CFD flow field is then advanced for the same fractional time-step [126].

### 7.0.2 PDF and ISAT

Being highly turbulent in nature, the combustion in IC engines is governed by Navier Stokes equations. Different techniques are used to solve these Navier Stokes equations as the direct solution of these equations computationally expensive. Reynolds averaging of these equations is one way to solve these equations. For turbulent chemistry in IC engines,

the Reynolds averaging approach results in two unknown terms for turbulent scalar flux and mean reaction rate. ANSYS FLUENT uses gradient diffusion to model turbulent scalar flux and treats turbulent convection as enhanced diffusion. Laminar, Eddy Dissipation Concept (EDC) finite rate chemistry models are used to model the mean reaction rate [126].

A transport equation for single-point, joint Probability Density Function (PDF) can alternatively be derived instead of Reynolds averaging of the species and energy equations. This PDF represents the fraction of time that the fluid spends at each temperature and pressure and the fraction of time that each species is present. For N species the PDF has N+2 dimensions (N arises due to the number of species and +2 arises from the temperature and pressure). Based on Pope's work [127], the following transport equation for PDF has been derived [126].

$$\begin{aligned} &\frac{\partial}{\partial t}(\rho P) + \frac{\partial}{\partial x_i}(\rho u_i P) + \frac{\partial}{\partial \Psi_k}(\rho S_k P) \\ &\qquad = -\frac{\partial}{\partial x_i}[\rho \langle u'' | \Psi \rangle P] + \frac{\partial}{\partial \Psi_k}[\langle \frac{1}{\rho} \frac{\partial J_{i,k}}{\partial x_i} \rangle P] \end{aligned} \tag{7.1}$$

Where $\rho$ is density, P and $u_i$ are Favre averaged PDF composition and mean fluid velocity, $\Psi$ and $S_k$ are the composition space vector and rate of reaction for species k respectively. $u''$ and $J_{i,k}$ are vectors representing fluctuation in fluid velocity and molecular diffusion flux respectively. The two terms on the right hand side involves expectation and conditional probability and can be summarized in the following analogy: $\langle$ X | Y $\rangle$ represents the expectation of X occurring provided that Y has occurred. The three terms on the right hand side of the equation 7.1 represent unsteady rate of change of PDF, change of PDF due to convection arising from the mean velocity field and the change of PDF due to chemical reactions. All the terms are closed and hence do not require any modeling. The closure of this heavily non linear term representing chemical reactions is a great advantage. Changes in PDF due to turbulent scalar flux and molecular diffusion are represented by the terms on the right hand side of the equation 7.1. The two terms on right hand side are not closed

and hence require modeling.

The composition vector $\phi$ which is a function of mass fraction of different species, temperature and pressure can be expressed as follows

$$\phi = (Y_1, Y_2, Y_3....Y_N, T, p) \tag{7.2}$$

where $Y_N$ is the mass fraction of the n$^{th}$ species. Integrating the reaction source term through reaction fraction step results in following equation.

$$\phi^1 = \phi^0 + \int_0^{dt} S dt \tag{7.3}$$

where S is the chemical source term. Some chemical reactions are fast and occur over a time scale of $10^{-10}$ seconds whereas other reactions may be considered slow and occur over a time scale of $10^{-3}$ seconds. The difference in these time scales of results in numerical stiffness. Direct or pre-integration [128, 129] of chemical results are others options. An earlier study [130] in the group has used pre-integration approach to map the combustion response in IC engines. This study used SENKIN, a sub-program in CHEMKIN-II to calculate the detailed chemical kinetic reactions of air/fuel mixtures at different temperatures, pressure and compositions. These calculations were done prior to the engine simulations. The reaction results were decoupled from their chemical time scales (order of about $10^{-10}$) and then integrated and saved in physical time scale (order of about $10^5$) in a database file. The reactions results of different initial conditions (temperature, pressure and composition) are stored in different zones. The zones were indexed using their respective reaction conditions. These reaction results were retrieved from this database file when needed during the simulation. It took 29 days to generate the database file.

For a simulation containing 40,000 cells and 15 particles per cell, if the convergence is achieved in 1500 iterations then $10^8$ stiff ordinary differential equations are required to be solved. If each integration is done in a few milli seconds, the solution becomes time expensive. Theoretically, the pre-tabulation of chemical results can help to avoid integration

via lookup tables but practically the scheme has many pitfalls. Any table constructed in this manner would have N+3 dimensions, where N stands for the number of species and 3 is for pressure, temperature and time. If each dimension has X points, the total number of data points will be $X^{N+3}$. For 10 points in each direction and 10 species , the table would have $10^{13}$ data entries. Another problem with this pre-tabulation is that it stores data on some reactions that are at unrealistic conditions, i.e. a data entry for OH radical at 300K.

ISAT is reported to be a powerful tool to integrate the realistic chemistry into multi-dimensional flows in an accelerated way [126]. The simulation starts with an empty ISAT table. As a first step, direct integration is performed by using ODE solver to integrate Eq. 7.3. This creates the first entry into the ISAT table. The first entry in the table consists of the initial composition ($\phi^0$), the mapping ($\phi^1$), the mapping gradient matrix ($\partial\phi^0/\partial\phi^1$) and a hyper ellipsoid of accuracy. The ellipsoid of accuracy is the elliptical space around a table point $\phi^0$ where the linear approximation to the mapping is accurate to the specified tolerance [126]. The mapping for the next reaction $\phi_q^1$ can be calculated as follows

$$\phi_q^1 = \phi^1 + (\partial\phi^0/\partial\phi^1)(\phi_q^0 - \phi^0) \tag{7.4}$$

$\phi_q^0$ is the initial composition vector for the second reaction and q stands for query. Whenever a query is raised, the table is linearly interpolated using the mapping gradient. If the new query $\phi_q^1$ is within the ellipsoid of accuracy, the linear interpolation is sufficiently accurate and mapping is retrieved. If the new query is $\phi_q^1$ is out side the ellipsoid of accuracy, a direct integration is performed and the mapping error is calculated. The mapping error is compared against the error tolerance. If the mapping error $<$ error tolerance, ellipsoid of accuracy is grown so as to include $\phi_q^1$. If the mapping error $>$ error tolerance, a new entry is added into the table. The ISAT table is structured as leaves in a binary tree. For each new query $\phi_q^0$, the already constructed ISAT table is traversed to identify which leaf has composition $\phi^0$ closer to the composition of the new query.

## 7.1 COMPUTATIONAL MODELS

A 90° sector mesh is used to take advantage of the symmetry of the four equally spaced injector nozzle holes. ICEM-CFD, a state of the art mesh generation package, was used to generate the mesh. With piston at the bottom dead center (BDC), the mesh consists of 26788 cells. The mesh is moved from BDC to the crank angle where intake valve closes. This is done through the dynamic mesh utility.

### 7.1.1 Numerical Scheme and Selection of Models

Unsteady flamlet model (UFM) has been used to predict in-cylinder pressure, the rate of heat release and different emissions. Two different spray breakup models have been used in the UFM approach; WAVE breakup model and KHRT. Three different values of each breakup constant were used for the parametric study conducted to assess the effect of the breakup constants on ignition delay, rate of pressure rise and the maximum in-cylinder pressure. The optimized set of breakup constants were selected and used in FRC approach to simulate the in-cylinder pressure and rate of heat release. The FRC approach uses a stiff chemistry solver with long computational times. To overcome this problem the volumetric reactions and the species that form during these reactions are switched off as no reaction can take place before the start of injection. During this time, only flow, turbulence, fuel (residuals), $O_2$, $CO_2$ and $H_2O$ equations are solved. All other reactions are switched off. A bigger time step is used during compression of the in-cylinder mixture. When injection starts, the time step is reduced to 0.1° CA for injection and combustion events. All reactions are switched on. The different physical aspects of the fluid are modelled as follows:

- Turbulence: RNG k-$\epsilon$ has been used. It takes into account swirling flow. Its computational cost is lower than LES model.
- Discrete Phase: Langrangian approach has been used to track individual droplets. It requires lower computational resource and simulation runtime.

- Primary breakup: Solid cone injection type has been used due to 3-D nature of the computational domain. It provides general shape of the spray.

- Secondary breakup model: Both WAVE and KHRT breakup models have been utilized as described in the following section.

- Droplet deformation: Dynamic drag model has been used due to its ability to capture droplet deformation due to aerodynamic forces.

- Droplet collision and coalescence: Droplet collision and coalescence models have been been considered. These models capture head-on collision, side collision and multi-body collision and coalescence. If these models are not used, the prediction of particle breakup due to collision is not captured.

- Wall-film: This model is used to predict the formation of thin fuel film at contact regions. This model takes into account the particle splashing, convective heat transfer from wall to fuel film and the evaporation of the fuel film.

- $NO_X$: Extended Zeldovich mechanism has been used to model the formation of $NO_X$. Thermal and prompt $NO_X$ have been predicted. The effect of turbulence on the formation of $NO_X$ has been considered. Temporal fluctuation of temperature and species concentration result from the turbulence.

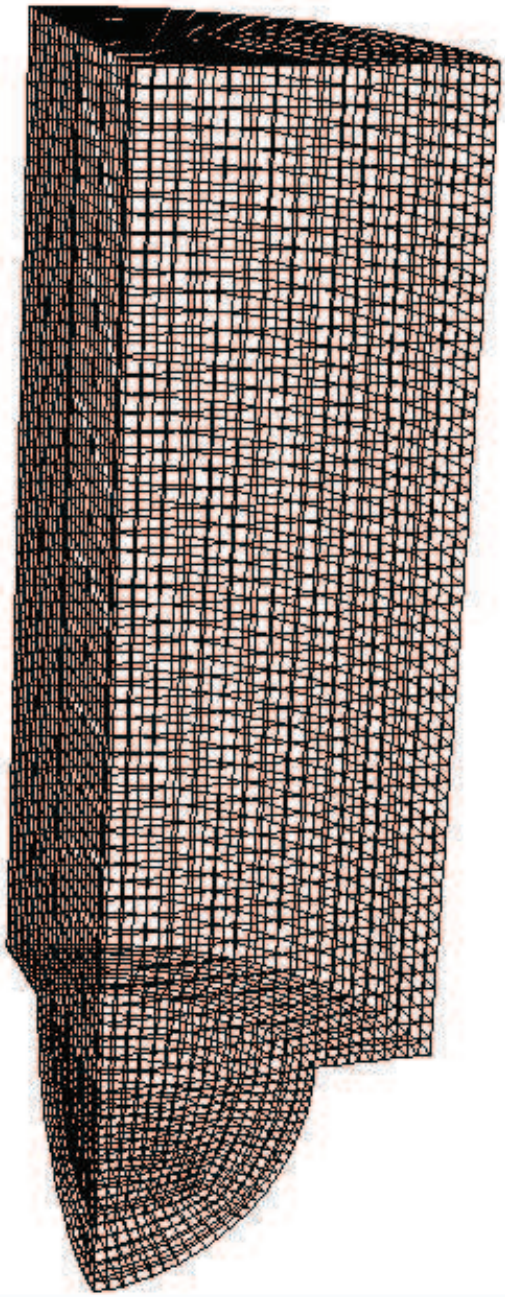

Figure 7.1. Computational Mesh used in the study

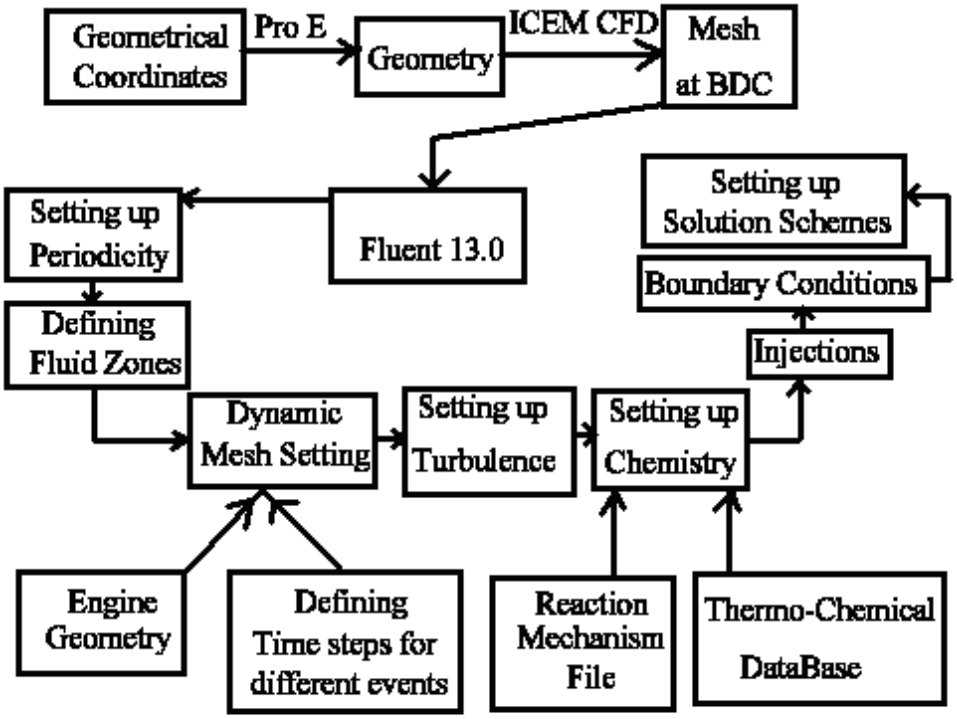


Figure 7.2. General numerical scheme used in the study

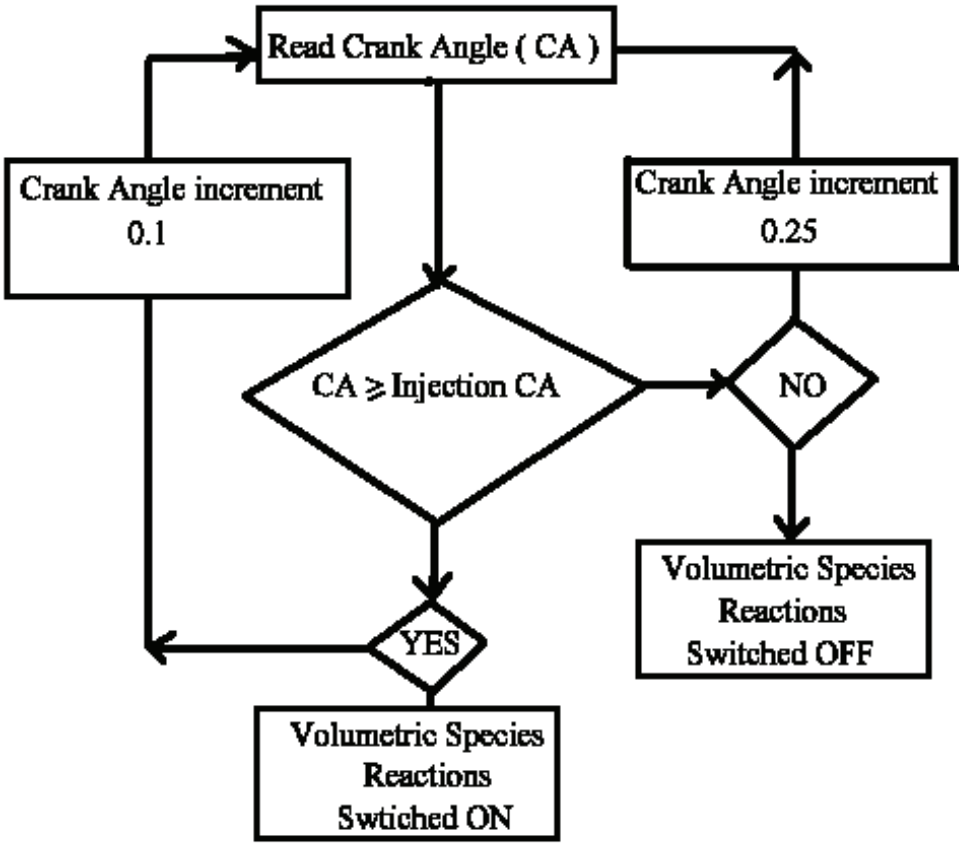


Figure 7.3. Numerical scheme used in finite rate chemistry approach to reduce computational time

### 7.1.2 Initial and Boundary Conditions

The Table 7.1 summarizes the initial and boundary conditions used in the simulations. Experimentally obtained values of temperature and pressure have used to initialized the solution at the time when the inlet valve closes and the simulation starts.

Table 7.1. Initial and boundary conditions used in the simulation

| Sr. No | Initial or boundary condition | Value |
|---|---|---|
| 1 | Start crank angle | -140$^0$ATDC |
| 2 | Stop crank angle | 130$^0$ATDC |
| 3 | Time step during compression stroke | 0.5$^0$ CA |
| 4 | Time step during injection, ignition and combustion | 0.1$^0$ CA |
| 5 | Temperature of cylinder wall | 545 K |
| 6 | Temperature of cylinder cylinder head | 610 K |
| 7 | Temperature of cylinder piston | 650 K |
| 8 | Initial pressure | 0.16 MPa |
| 9 | Fuel inlet temperature | 370 K |
| 10 | Pressure discretization scheme | Standard |
| 11 | Turbulent dissipation rate discretization scheme | second order upwind |
| 12 | Density for diesel | 840 kg/m$^3$ |
| 13 | Saturation vapour pressure schem | piecewise linear |
| 14 | Droplet surface tension calculation | piecewise polynomial |

### 7.1.3 Parametric Study

Three values (10, 25 and 50) of the breakup model constant $B_1$ are used. Three values (10, 30 and 50) of the KHRT breakup model constant $C_3$ are used. When unsteady flamlet model (UFM ) uses WAVE model for the secondary break, the effect of variation in $B_1$ is significant. Ignition, rate of pressure rise as well the maximum in-cylinder pressure are all affected by any change in this breakup constant. As the value of this breakup constant is increased, ignition is slightly delayed and a higher rate of pressure rise as well as higher peak in-cylinder pressures are observed. The minimum value of $B_1$ produces the best agreement with the experimental data. Theoretically, a higher value of $B_1$ shall reduce the breakup and hence increase the penetration length. On the other hand, a smaller value of $B_1$ results in increased spray atomisation. The increased spray atomisation results in better fuel/air mixing. Relatively shorter ignition delay for the two lower values of the breakup constant $B_1$ and a longer ignition delay when $B_1$ was set at 50 can be explained on this basis.

All three cases of UFM with different values of $B_1$ have captured the ignition delay trend. The peak pressure occurs at the same crank angle position for all three cases. This can explain the higher rate of pressure rise when the ignition delay is maximum at $B_1$=50. With shorter breakup length, the fuel is atomised and combustion commences earlier but the dispersion of the fuel may not cover the whole volume of high temperature air available at that particular crank angle (reduced air utilisation). With longer breakup length, the fuel atomisation and hence ignition is delayed but air utilisation is improved. Hence a larger proportion of the fuel is consumed at the same time leading to higher rate of pressure rise and hence increased heat release rate. When UFM uses KHRT model to simulate the secondary breakup model, a very good agreement is noted between the experimental and the computational results. The effect of change in $C_3$ on ignition delay, rate of pressure rise and the peak in-cylinder pressure is less pronounced when compared to the effect of change in WAVE breakup model constant $B_1$. For the two smaller values of $C_3$, no difference was observed in terms of ignition delay, rate of pressure rise and the peak in-cylinder pressure.

When $C_3$ was set a very higher number, smaller rate of pressure rise and lower peak in-cylinder pressure were obtained. According to the model, the breakup will only occur if the wavelength of the wave growing on the surface of the liquid droplet is smaller than the droplet diameter. A larger value of $C_3$ shall reduce the breakup and result in larger droplet diameter. This can explain the smaller rate of pressure rise with increasing value of $C_3$. Larger diameter droplets shall take longer to evaporate and hence result in slower rate of pressure rise. For the largest $C_3$ value, the pressure drops more rapidly in the expansion stroke of the cycle.

### 7.1.4 In-Cylinder Pressure and Rate of Energy Release

Figures. 7.4 and 7.5 show computationally predicted in-cylinder pressure using UFM approach utilizing the WAVE and KHRT breakup models respectively. An overall better agreement is achieved with UFM approach when KHRT breakup model is used. Figures. 7.6 and 7.7 show computationally predicted rate of energy release using UFM approach utilizing the WAVE and KHRT breakup models respectively. From Figures 7.6 and 7.7, it is clear that the experimental rate of energy release rises first compared to the computational trend line which reflects that the model does not predict the ignition behaviour well but the start of the main combustion event is well predicted. This may be due to limited knowledge of the injection mass profile, differences between fuel surrogate and the real diesel, cavitation in the injector, pressure changes in the injector, fuel residuals and injector dribble. With

| Chosen value of $B_1$ | Peak Combustion Pressure/ MPa |
|---|---|
| 10 | 6.085 |
| 25 | 6.261 |
| 50 | 6.47 |

Table 7.2. Effect of Wave breakup constant $B_1$ on peak combustion pressure

UFM, two rate of energy release peaks are observed. The first predicted rate of energy release peak occurs 1°CA before the corresponding peak for the experimentally obtained rate of energy release curve. All predicted results produced higher second rate of energy release peak when compared to the experimental results. For the different values of breakup constants tested within the different models used, $B_1 = 10$ (WAVE model) and $C_3 = 30$ (KHRT model) give better prediction of in-cylinder pressures and the rate of energy release. Hence these two values have been chosen to be used for the FRC model.

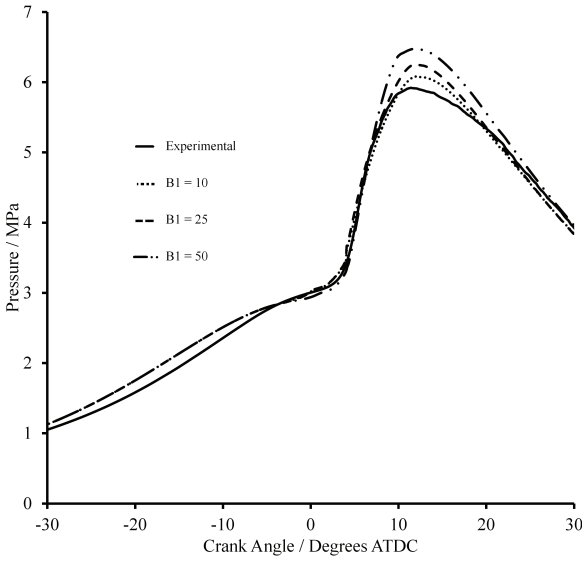


Figure 7.4. Comparison of In-cylinder pressure for different values of breakup constant $B_1$ using wave breakup model

Figures 7.8 and 7.9 show computationally predicted in-cylinder pressure and rate of energy release by using FRC approach and utilizing the WAVE ($B_1 = 10$) and KHRT ( $C_3 = 30$ ) breakup models respectively. The FRC model does not show as close agreement to the experimental data as was observed with UFM. The model fails to simulate the start of the main combustion event and also produces higher peak pressure for both spray models. When FRC approach utilizes WAVE breakup model, the start of the combustion is further delayed and the in-cylinder peak pressure is also higher compared to the results obtained using the KHRT model.

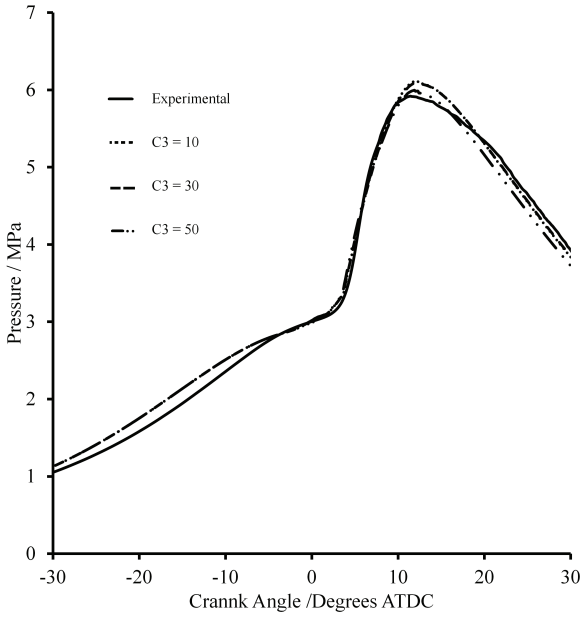


Figure 7.5. Comparison of In-cylinder pressure for different values of breakup constant $C_3$ using KHRT breakup model

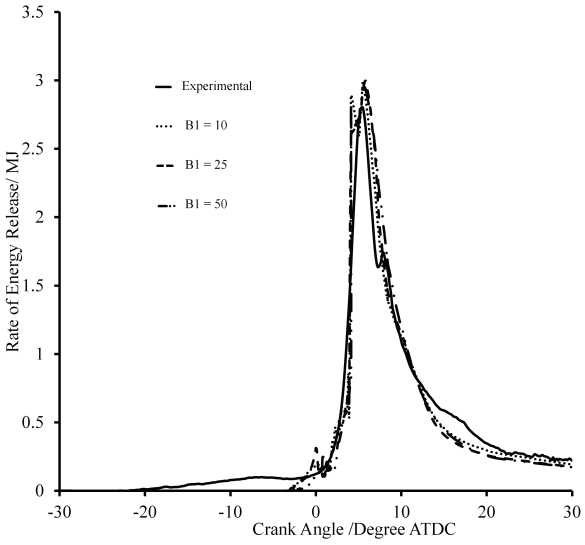


Figure 7.6. Comparison of rate of energy release for different values of breakup constant $B_1$ using wave breakup model

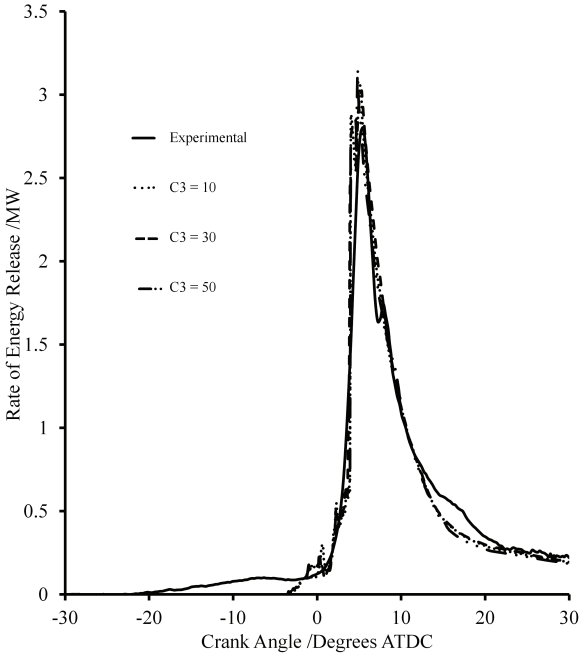


Figure 7.7. Comparison of rate of energy release for different values of breakup constant $C_3$ using KHRT breakup model

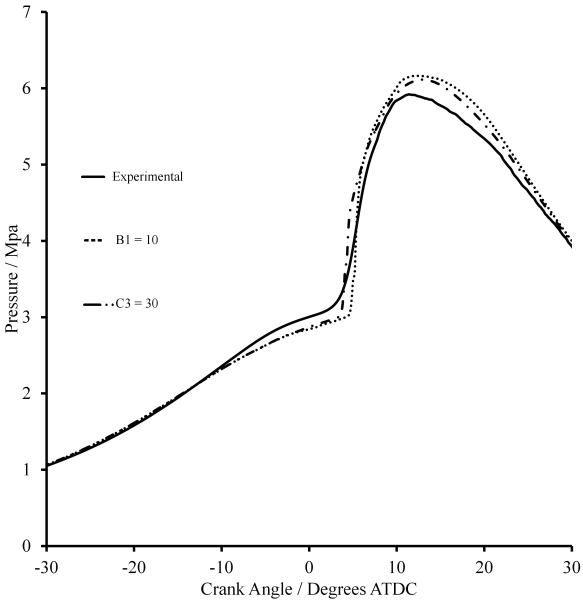


Figure 7.8. Comparison of In-cylinder pressure for wave breakup model ($B_1 = 10$ ) and KHRT breakup model ( $C_3 = 30$ ) using using finite rate chemistry approach

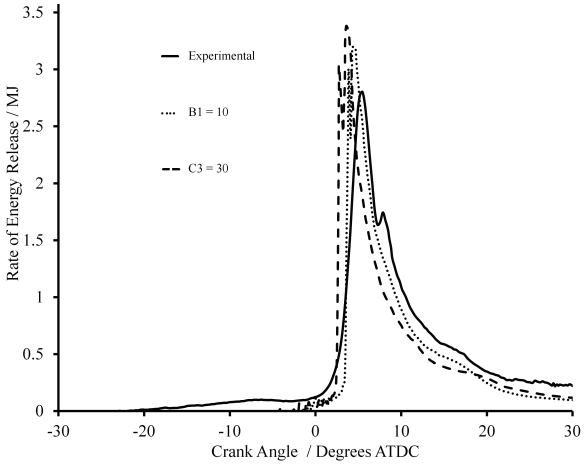


Figure 7.9. Comparison of rate of energy release for wave breakup model ($B_1 = 10$ ) and KHRT breakup model ( $C_3 = 30$ ) using using finite rate chemistry approach

### 7.1.5 Prediction of Emissions

Figures 7.10, 7.11 and 7.12 show comparison of experimentally and numerically obtained emissions of specific $NO_X$, $CO_2$ and CO respectively.

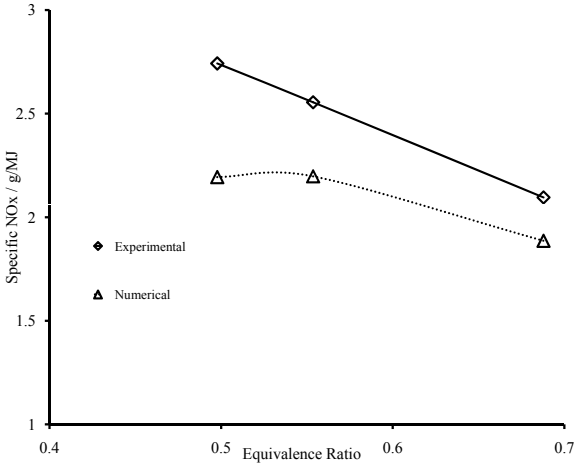


Figure 7.10. Comparison of experimentally and numerically obtained specific $NO_X$ emissions

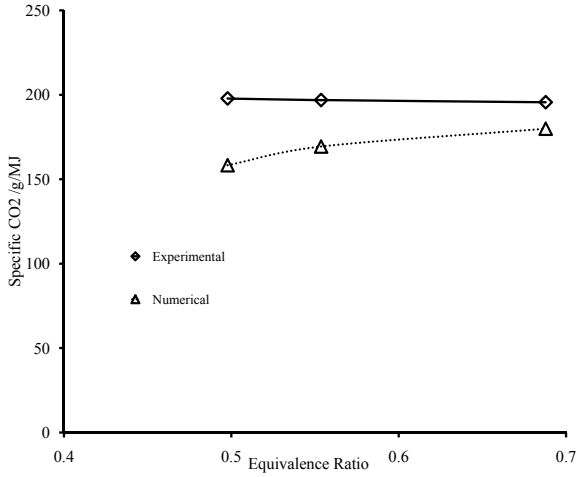


Figure 7.11. Comparison of experimentally and numerically obtained specific $CO_2$ emissions

Of all combinations of combustion and spray models tried with different breakup constants, the UFM produces the best estimate of the in-cylinder pressure and the rate of energy release when KHRT spray model with a breakup constant ($C_3$) set at 30 is used. Due to this reason this combination has been chosen to predict three of the in-cylinder

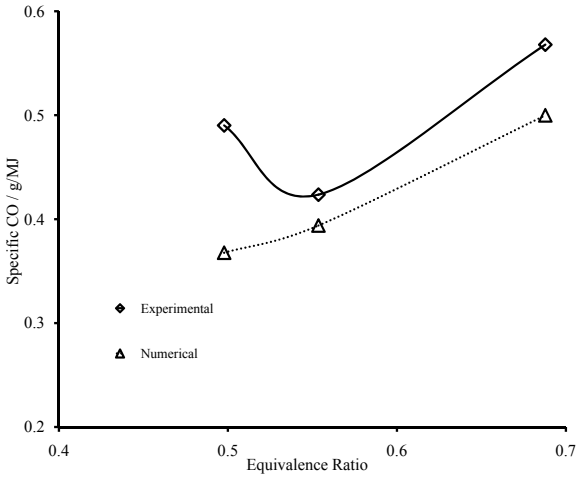


Figure 7.12. Comparison of experimentally and numerically obtained specific CO emissions

emissions. The computational results for three emissions were lower than the levels collected experimentally but the UFM approach has captured the trends. The agreement between the computational and the experimental results improved as the equivalence ratio was increased. The computationally predicted specific $NO_X$ was 20% lower than the experimentally obtained values at an equivalence ratio of 0.5. The agreement between the computationally and experimentally obtained specific $NO_X$ was improved and lie within 10% of each other with an equivalence ratio of 0.68. The agreement between the computationally and experimentally obtained specific $CO_2$ emissions range between 18% at the lowest equivalence ratio to 8% at the highest equivalence ratio. The CO emissions were the least well predicted. The agreement between the computationally and experimentally obtained specific CO is 25%, 7% and 12% at the three equivalence ratios tested.

| Equivalence ratio | Type of emissions | %ge difference in prediction |
|---|---|---|
| 0.50 | $NO_X$ | -20 |
| 0.55 | $NO_X$ | -13 |
| 0.68 | $NO_X$ | -9.5 |
| 0.50 | $CO_2$ | -18 |
| 0.55 | $CO_2$ | -11 |
| 0.68 | $CO_2$ | -8 |
| 0.50 | CO | -25 |
| 0.55 | CO | -7 |
| 0.68 | CO | -12 |

Table 7.3. Percentage variation in the predicted emissions when compared to the experimental data across three different equivalence ratios using KHRT breakup model ( $C_3 = 30$ ) and unsteady flamlet approach

### 7.1.6 Contours of $O_2$ Emissions

Figures 7.13 to 7.19 show the contours of $O_2$ mass fraction from -9° ATDC to 18°ATDC.

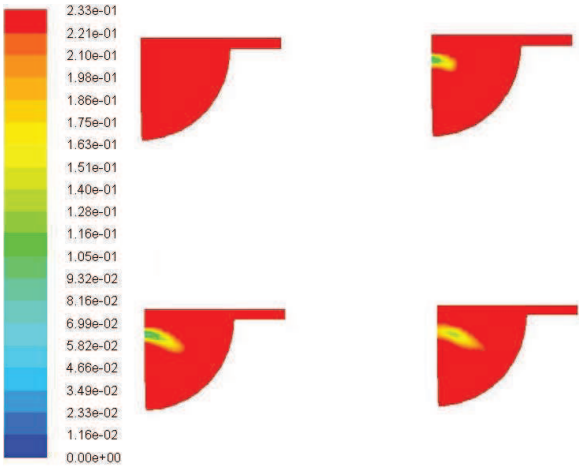


Figure 7.13. Contours of $O_2$ from -9°ATDC to -6°ATDC using KHRT breakup model ( $C_3 = 30$ ) and unsteady flamlet approach

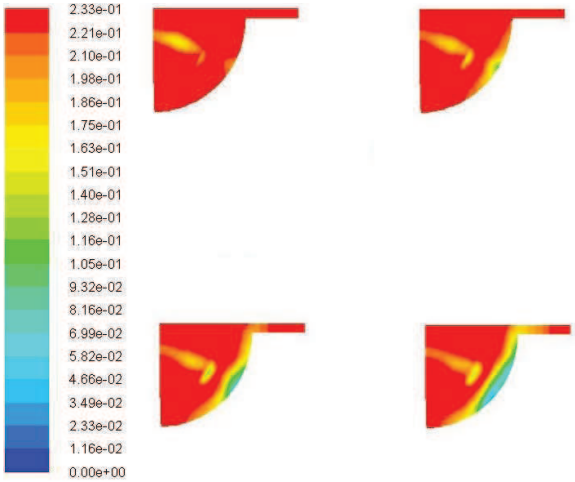


Figure 7.14. Contours of $O_2$ from -5°ATDC to -2°ATDC using KHRT breakup model ( $C_3 = 30$ ) and unsteady flamlet approach

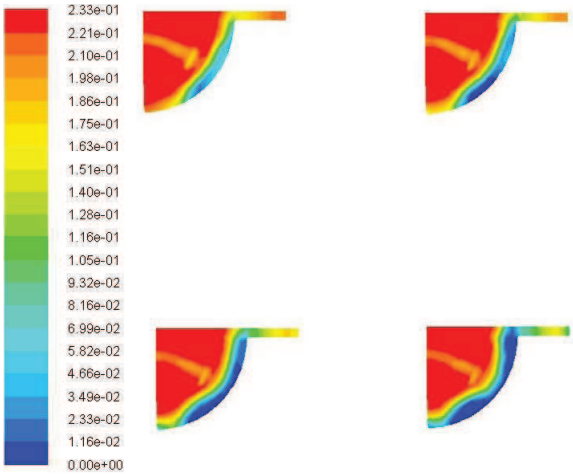


Figure 7.15. Contours of $O_2$ from -1°ATDC to 2°ATDC using KHRT breakup model ( $C_3 = 30$ ) and unsteady flamlet approach

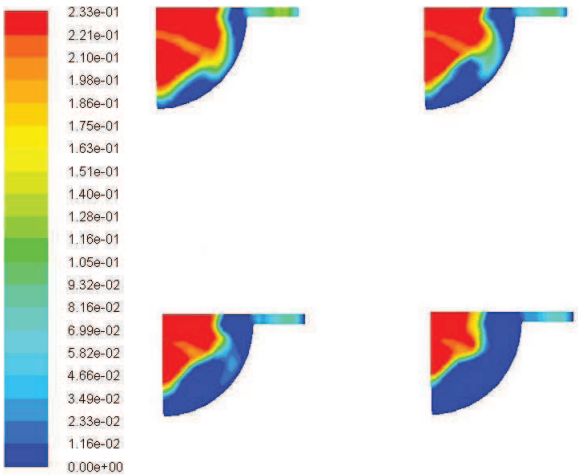


Figure 7.16. Contours of $O_2$ from 3°ATDC to 6°ATDC using KHRT breakup model ( $C_3 = 30$ ) and unsteady flamlet approach

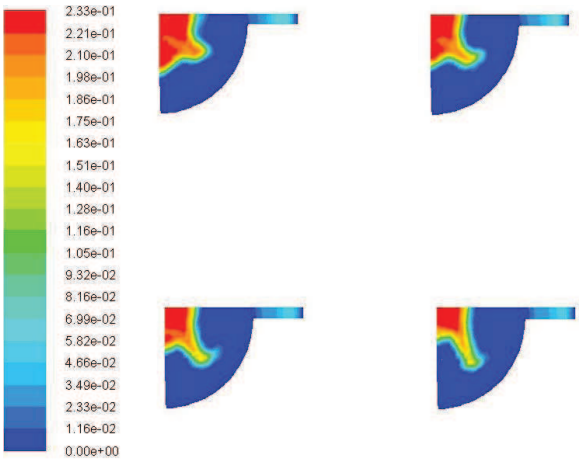


Figure 7.17. Contours of $O_2$ from 7°ATDC to 10°ATDC using KHRT breakup model ( $C_3 = 30$ ) and unsteady flamlet approach

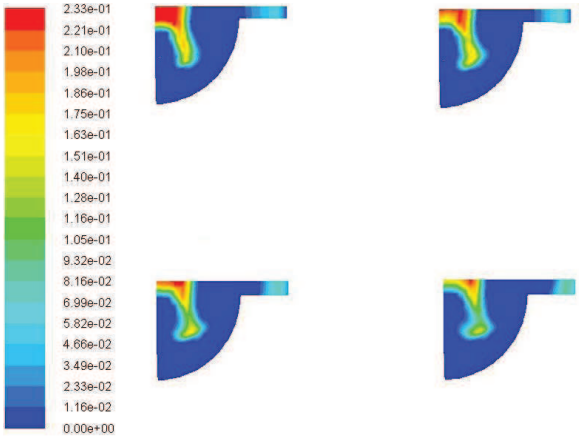


Figure 7.18. Contours of $O_2$ from 11°ATDC to 14°ATDC using KHRT breakup model ( $C_3 = 30$ ) and unsteady flamlet approach

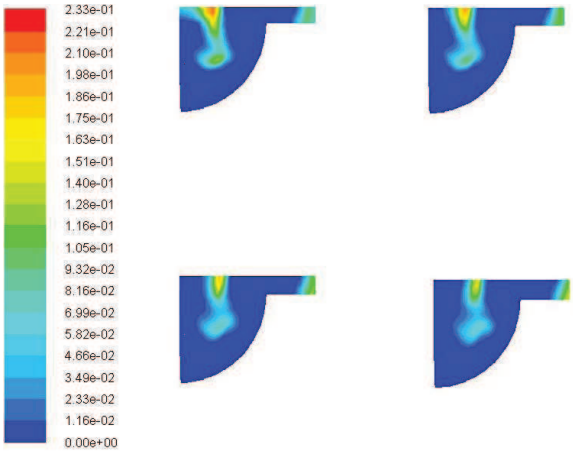


Figure 7.19. Contours of $O_2$ from 15°ATDC to 18°ATDC using KHRT breakup model ( $C_3 = 30$ ) and unsteady flamlet approach

### 7.1.7 Contours of Mass Averaged In-cylinder Temperature

Figures 7.20 to 7.24 show the contours of mass averaged static temperature from -6°ATDC to 10°ATDC. These mass average temperature contours along with the contours of oxygen can help to inerprete the contours of $NO_X$.

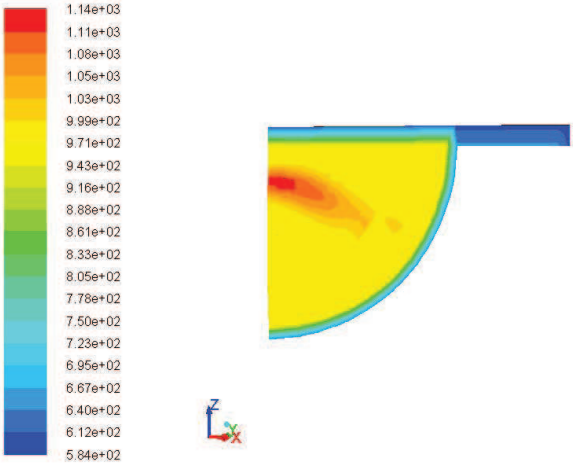


Figure 7.20. Contours of mass averaged static temperature at -6°ATDC using KHRT breakup model ( $C_3 = 30$ ) and unsteady flamlet approach

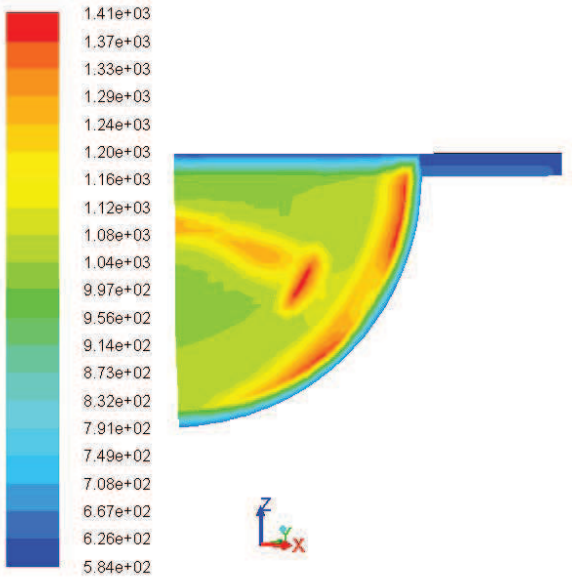


Figure 7.21. Contours of mass averaged static temperature at -2°ATDC using KHRT breakup model ( $C_3 = 30$ ) and unsteady flamlet approach

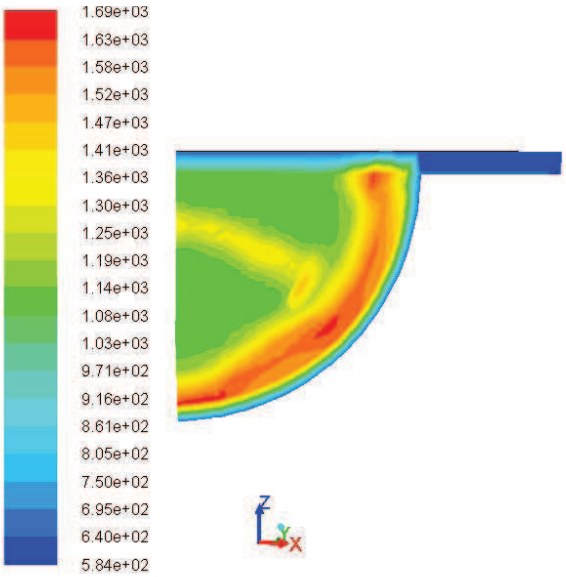


Figure 7.22. Contours of mass averaged static temperature at 2°ATDC using KHRT breakup model ( $C_3 = 30$ ) and unsteady flamlet approach

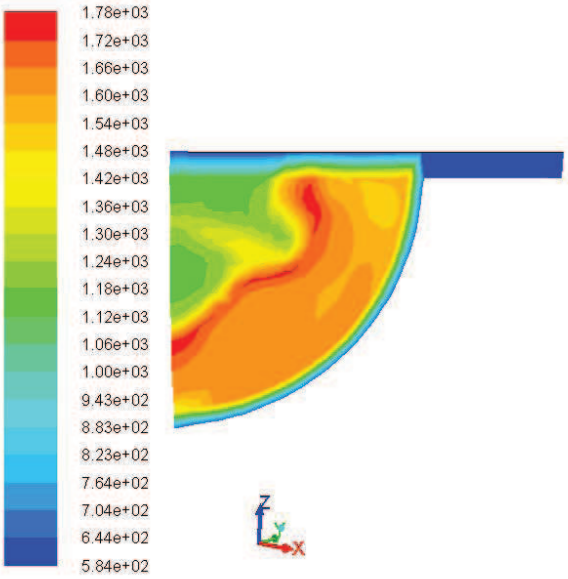


Figure 7.23. Contours of mass averaged static temperature at 6°ATDC using KHRT breakup model ( $C_3 = 30$ ) and unsteady flamlet approach

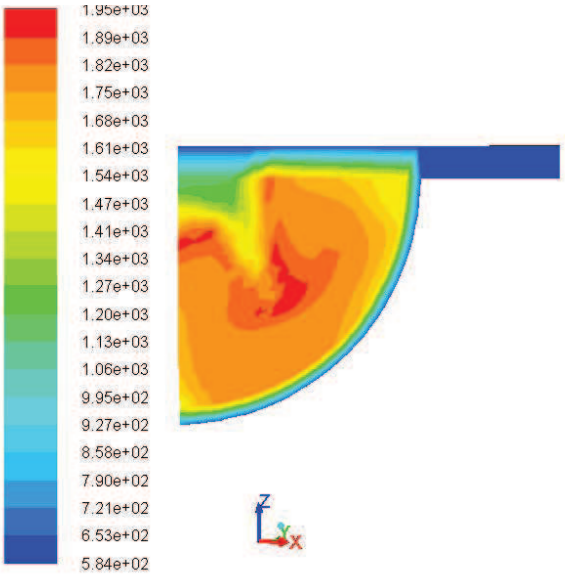


Figure 7.24. Contours of mass averaged static temperature at 10°ATDC using KHRT breakup model ( $C_3 = 30$ ) and unsteady flamlet approach

### 7.1.8 Contours of NO Mass Fraction

Figures 7.25 to 7.29 show the contours of no mass fraction from -6°ATDC to 10°ATDC.

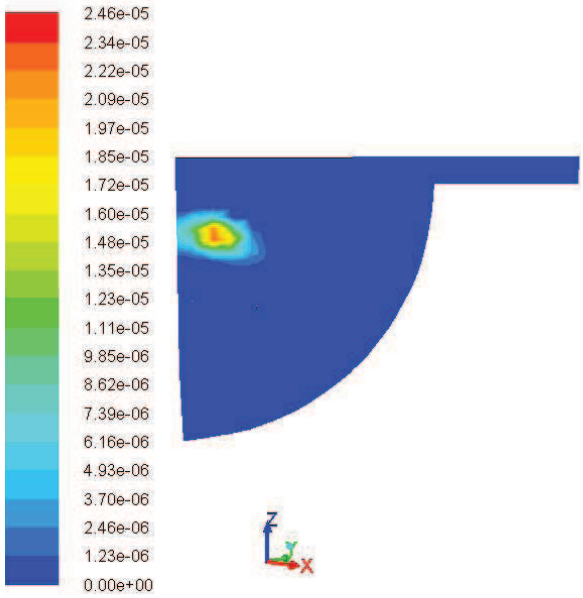


Figure 7.25. Contours of NO at -6°ATDC using KHRT breakup model ( $C_3 = 30$ ) and unsteady flamlet approach

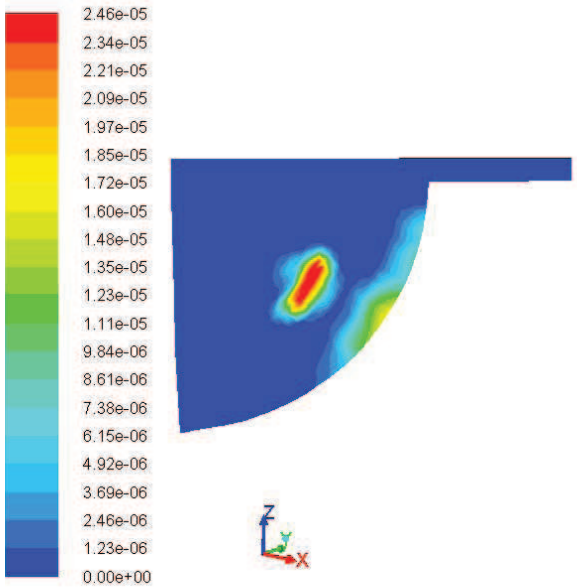


Figure 7.26. Contours of NO at -2°ATDC using KHRT breakup model ( $C_3 = 30$ ) and unsteady flamlet approach

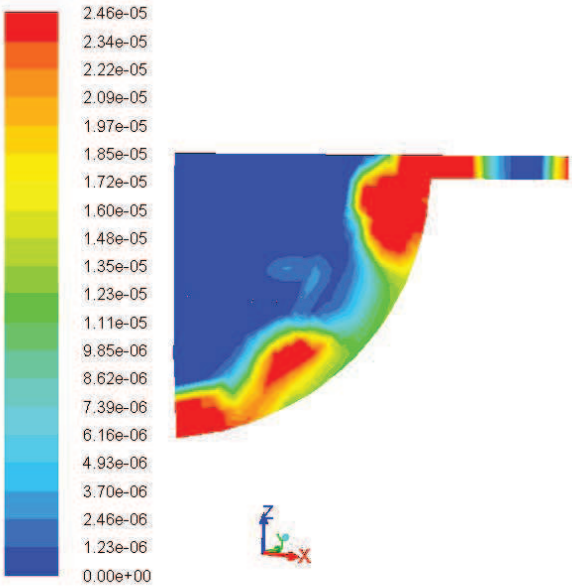


Figure 7.27. Contours of NO at 2°ATDC using KHRT breakup model ( $C_3 = 30$ ) and unsteady flamlet approach

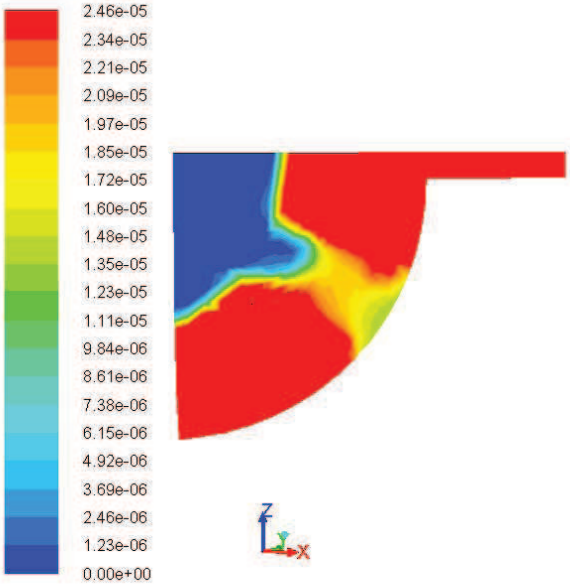


Figure 7.28. Contours of NO at 6°ATDC using KHRT breakup model ( $C_3 = 30$ ) and unsteady flamlet approach

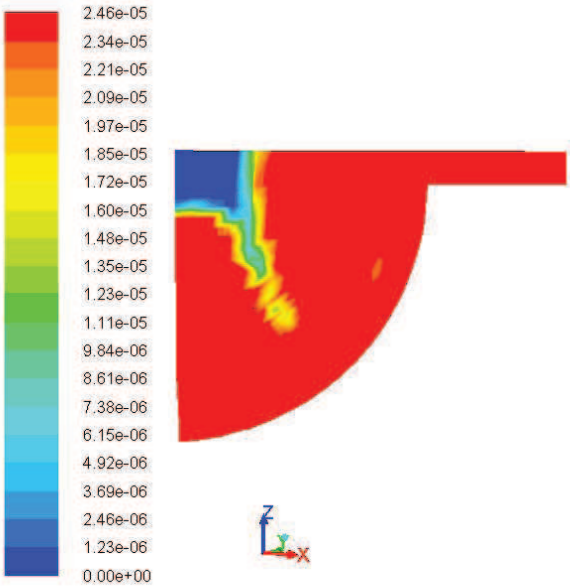


Figure 7.29. Contours of NO at 10°ATDC using KHRT breakup model ( $C_3 = 30$ ) and unsteady flamlet approach

## 7.2 CHAPTER SUMMARY

Computational fluid dynamics (CFD) has recently been extensively employed to study different features of internal combustion engines. Modeling diesel combustion under CI environment remains at the center stage of these CFD studies. This study uses combinations of different spray and combustion models to predict in-cylinder pressure and rate of heat release. The approach employs two combustion models: Unsteady Flamelet Model (UFM) with PDF method and; Finite Rate Chemistry (FRC) with stiff chemistry solver implemented through In-Situ Adaptive Tabulation (ISAT) algorithm. The two spray models used were WAVE and Kelvin Helmohltz Rayleigh Taylor (KHRT) models. $B_1$ and $C_3$ are the adjustable constants for the WAVE and KHRT breakup models respectively. Three different values of each of these two breakup model constants were used in the Unsteady Flamelet approach. $B_1 = 10$ and $C_3 = 30$ gives better agreement with the experimental in-cylinder pressure data and hence these values were chosen to be used in FRC model. The unsteady flamelet model coupled with KHRT spray model have been used to predict $NO_X$, CO and $CO_2$ emissions. The model captures the emissions trends well. In-cylinder contours of $O_2$, NO and mass averaged static temperature have also been presented. A chemical mechanism of n-heptane with 29 species and 52 reactions has been used.

# CHAPTER 8
# CONCLSUIONS AND FUTURE WORK

## 8.1 CONCLUSIONS

Following conclusions can be drawn from the discussion presented above. When the performance and emissions maps of diesel and RME fuels were compared:

- Thermal efficiencies of diesel and RME are comparable for all ranges of speeds and power outputs. At the maximum powers, RME has a larger brake thermal efficiency. For diesel at the maximum power output there is a small drop in brake thermal efficiency which is not present with RME.

- From the location of maximum $NO_X$ in the central region of the maps, the specific $NO_X$ decreases in all directions across the whole map. For lower and medium speeds, the specific $NO_X$ emissions increases initially as the power output is increased, and then starts decreasing after reaching a maximum value. RME produces lower specific $NO_X$ as compared to the diesel fuel.

- The operating speed of the engine affects $NO_X$ formation, and lower specific $NO_X$ are produced at higher speeds. Shorter residence time for $NO_X$ formation can be responsible for this trend.

- Higher HC values are obtained with RME at lower and lower medium values of the power at all speeds. This can be attributed to relatively poor atomization and lower volatility of RME

- RME produced lower $CO_2$ due to lower carbon to hydrogen ratio as compared to diesel.

For the diesel and RME piloted combustion of natural gas in CI engines:

- Apart from the highest power outputs, the natural gas dual fueling case was less efficient as compared to the respective pilot fuel based single fueling. These efficiency losses at lower powers can be attributed to the under-utilization of the pilot fuel. The lower thermal efficiency values at lower power may be attributed to the failure of pilot fuel to ignite and sustain adequate combustion of the natural gas-air mixture. Whilst the local equivalence ratio in the region of the pilot injection may be near unity (stoichiometric), especially during the initial pre-mixed combustion phase, there can exist some areas with in the combustion chamber away from the pilot region where there is a lean homogeneous mixture of natural gas and air. This argument is supported by relatively lower Fuel to air ratio obtained in case of dual fueling. As the power output increases the dual fuel mode recovers the thermal efficiency losses suffered at the lower power outputs with the dual fuel mode exhibiting slightly higher F/A ratios at these conditions.

- The slope of the constant volumetric efficiency is flatter for natural gas dual fueling with diesel than for baseline diesel operation and the values are lower. This is a consequence of the method used to introduce natural gas into the engine. As the natural gas has been introduced via manifold injection, a portion of the intake air is displaced by the natural gas, reducing the measured volume flow rate of air into the engine. This leads to a reduction of the engine's volumetric flow rate. The slope of the constant volumetric efficiency lines differs due to a change in the scaling of volumetric efficiency with engine speed. As the amount of natural gas added is increased to meet the increase in speed demand, larger amounts of air are displaced. As the natural gas is introduced at the manifold and does not flow through the entire intake system but the air does, the scaling law as noted by Heywood [10] does not hold.

- Natural gas based dual fueling has resulted in significant reduction in $NO_X$ when compared to the diesel and RME based single fueling cases. This reduction in $NO_X$

is a direct consequence of difference in the in-cylinder mixture composition prior to ignition and combustion events. Significantly higher specific heat capacity of natural gas raises the overall specific heat capacity of the mixture and results in lower temperatures during compression stroke. With the formation of $NO_X$ highly dependent on thermal mechanism, the lower in-cylinder temperature results in lower specific $NO_X$ as compared to the single fueling.

- Specific $NO_X$ emissions in case of both single fueling cases are centered in the middle of the map and they decrease in all direction from this region of maximum specific $NO_X$. On the other hand, an opposite trend is observed with natural gas dual fueling where minimum specific $NO_X$ are centered at the middle of the map and they increase in all directions from this region of minimum $NO_X$.

- The specific $NO_X$ emissions contours have similar trends, and those with RME are lower than those with diesel.

- At lower power outputs across all speeds, the specific HC emissions were significantly higher in case of dual fueling when compared to the respective pilot fuel based single fueling. This can be attributed to low in-cylinder temperature due to relatively higher specific heat capacity of the mixture. As the power was increased at constant speed, the specific HC emissions were significantly reduced, though still higher than the respective single fueling cases. Also, the equivalence ratio threshold for dual fuel modes is 0.4. Below this threshold value, the HC emissions increase whereas increasing equivalence ratio beyond this value results in a decrease in HC emissions.The equivalence ratio in this case ranges between 0.44 and 0.79 and this is reflected in gradual decrease of HC emissions as the load increase.

- Studying the specific $NO_X$ and specific HC maps together has revealed that the of junction of lower powers and lower speeds is a region in the maps where the engine

shows the worst trade-off between the $NO_X$ and HC emissions as the two emissions are higher in this region.

For the diesel and RME piloted combustion of hydrogen:

- In dual fuel mode the maximum thermal efficiency reached with RME is marginally lower than the maximum thermal efficiency reached with diesel.

- In general, at a given power rating the volumetric efficiency decreases as the engine's speed increases due to increasing friction of the air flow during the induction and exhaust phase of the cycle. At a given engine operating speed higher loads mean more fuel and higher operating temperatures, including higher inlet manifold temperature, thus heating the intake air and reducing volumetric efficiency. The combined effect results in the slope of volumetric efficiency contour lines shown in the figures. The slope of the volumetric efficiency contours is flatter and values are lower for hydrogen dual fueling when compared to diesel and RME based single fueling cases This is a consequence of the method used to introduce hydrogen into the engine. As the hydrogen has been introduced via manifold injection, a portion of the intake air is displaced by the hydrogen, reducing the measured volume flow rate of air into the engine. This leads to a reduction of the engine's volumetric flow rate. The slope of the iso-contours differs due to a change in the scaling of volumetric efficiency with engine speed. As the amount of hydrogen added is increased to meet the increase in speed demand, larger amounts of air are displaced. As the hydrogen is introduced at the manifold and does not flow through the entire intake system but the air does, the scaling law as noted by Heywood [10] does not hold.

- Hydrogen addition has been shown to increase specific $NO_X$ emissions with both of the pilot fuels when compared to the respective single fueling cases. The lower ignition energy and wider operating equivalence ratio of hydrogen result in the specific $NO_X$

trends in the diesel piloted dual fueling to follow the shape of the thermal efficiency contours.

- RME piloted hydrogen shows slightly reduced $NO_X$ emissions compared to diesel piloted hydrogen at higher speeds.

- Lower specific HC emissions were recorded at highest loads attributed to reduction in carbon to hydrogen ratio and improved combustion with increasing hydrogen addition.

- Overall diesel has shown better performance as a pilot fuel for hydrogen.

When the effect of pilot fuel quantity and type on the combustion and emissions of natural gas and hydrogen was investigated:

- Dual fueling of natural gas exhibit an increased ignition delay when compared to the ignition delay exhibited by the pilot fuel when tested in single fueling mode at similar operating conditions. For dual fueling cases, the ignition delay is reduced as the quantity of pilot fuel in increased.

- For a certain operating condition, there exists a pilot fuel quantity threshold beyond which any increment in the pilot fuel quantity shall not result in reduced ignition delay and higher maximum in cylinder pressure.

- Both for diesel as well as RME piloted combustion of natural gas at higher speeds, the specific $NO_X$ have been generally found proportional to the quantity of pilot fuel where as at lower speeds, there exists a pilot fuel quantity threshold where maximum specific $NO_X$ are produced and any pilot fuel setting below or above the threshold shall result in lower specific $NO_X$.

- Like specific $NO_X$, specific HC emissions from diesel and RME piloted combustion of natural gas also exhibit the pilot fuel quantity threshold phenomenon. At lower

speeds, the specific HC emissions decrease as the quantity of pilot fuel is increased. At higher speeds, there exists a pilot fuel quantity threshold below or above which the specific HC emissions increase with any increase in the pilot fuel quantity.

- At relatively lower values of BMEP, the specific HC emissions vary significantly and the trend lines converge as BMEP is increased.

- For RME piloted combustion at 1500 rev/min, the specific $CO_2$ emissions increase as the quantity of pilot fuel is increased across all values of BMEP. The diesel piloted combustion of natural gas exhibit similar trends with an exception at the highest load.

- For diesel as well as RME piloted hydrogen combustion, the ignition delay is shortened as the quantity of pilot fuel increased but the peak cylinder pressure does not seem to be a very strong function of ignition delay. Similar peak pressure is achieved even when the pilot fuel is set at a minimum BMEP for diesel piloted hydrogen combustion at 1000 rev/min.

- When the hydrogen is piloted by diesel at 1000 rev/min, similar first rate of energy release peaks are observed for all pilot fuel settings. The lowest pilot fuel setting (n=1) shows a clearly large second rate of energy release peak when compared with the two higher pilot fuel setting cases(n=2,3).

- Specific $NO_X$ has shown different trends at different speeds when hydrogen dual fueling is piloted by either diesel or RME. At lower speeds, the specific $NO_X$ decrease as the quantity of pilot fuel is increased. At higher speeds, the specific $NO_X$ increase as the quantity of pilot fuels is increased.

- Diesel piloted combustion of hydrogen has shown higher specific HC emissions when compared to the RME piloted combustion of hydrogen at both speeds. Lower BMEP values are an exception to this trend. At 1000 rev/min, smaller variation is observed

in specific HC emissions when diesel pilots the hydrogen combustion. At higher engine speed, lower specific HC emissions were resulted when the quantity of pilot fuel was increased. This trend was held for both pilot fuels.

- For CO and $CO_2$ emissions, a proportional increase in the emissions have been observed when the pilot fuel quantity was increased owing to the fact that the gaseous fuel (hydrogen in this case) does not have any carbon in it. So, any carbon based emissions have to come from the liquid pilot fuel (either diesel or RME in this case).

- Unlike specific HC emissions where diesel and RME piloted combustion of hydrogen occupied different islands at both 1000 and 1500 rev/min, the specific CO and $CO_2$ do not exhibit this trend. At 1000 rev/min, similar specific emissions were obtained for the corresponding pilot fuel setting for both pilot fuels. At 1500 rev/min, diesel piloted combustion of hydrogen resulted in higher specific $CO_2$ as compared to RME piloted combustion of hydrogen at the corresponding conditions.

The numerical part of this thesis applies two different approaches to predict in-cylinder pressure and rate of energy release. Unsteady flamelet approach utilizes two spray breakup models with changing spray breakup constant to assess the effect of breakup length on the in-cylinder pressure and the rate of energy release.

- When unsteady flamlet model (UFM ) uses wave model for the secondary break, the effect of variation in $B_1$ is significant. Ignition, rate of pressure rise as well the maximum in-cylinder pressure are all affected by any change in this breakup constant. The minimum value of $B_1$ produces the best agreement with the experimental data. The peak pressure occurs at the same crank angle position for all three cases with different value of $B_1$. This can explain the higher rate of pressure rise at $B_1$=50. With shorter breakup length, the fuel is disintegrated and ignited quickly but the dispersion of the fuel may not cover the whole volume of high temperature air available at that particular crank angle. With longer breakup length, the fuel disintegration and

ignition is delayed but when it disintegrates and ignites it covers the whole volume of air available. Hence more fuel is burned together and more energy is released leading to a higher rate of pressure rise.

- For KHRT breakup model, no difference was observed in terms of ignition delay, rate of pressure rise and the peak combustion pressure for the two smaller values of $C_3$. When $C_3$ was set a very higher number, smaller rate of pressure rise and lower peak combustion pressure were obtained. A larger value of $C_3$ shall reduce the breakup and result in larger droplet diameter. This can explain the relatively smaller rate of pressure rise for a higher value of $C_3$. Larger diameter droplets shall take longer to evaporate and hence shall result in relatively slower rate of pressure rise. For the largest $C_3$ value, the pressure drops more rapidly in the expansion stroke of the cycle.

- Of all combinations of combustion and spray models tried with different breakup constants, the unsteady flamelet models produces a better estimate of the in-cylinder pressure the rate of energy release when KHRT spray model is utilized with breakup constant $C_3$ set at 30.

- The agreement between the computational and the experimental results got better as the equivalence ratio was increased.

- The computationally predicted specific $NO_X$ were 20% lower than the experimentally obtained values at an equivalence ratio of 0.5. The agreement between the computationally and experimentally obtained specific $NO_X$ was improved for higher equivalence ratios and it was under 10% which is very reasonable.

- The agreement between the experimental and the computational results for specific $CO_2$ emissions range between 18% at the lowest equivalence ratio to 8% at the highest equivalence ratio.

- The CO emissions were the least well predicted among all. The agreement between the experimental and the computation is 25%, 7% and 12% at the three equivalence ratios that were tested.

In the next section recommendations for the future work are discussed which are worthy of further investigations based on the work presented here.

## 8.2 FUTURE WORK

The dual fueling cases involved in this study were restricted to the intake manifold induction of the gaseous fuels. Direct injection of these gaseous fuels is an area that can be explored. Injection timing as well as injection duration were also not changed during this study because of the in-line pump injection system. Applications of the common rail to investigate of the change in injection duration as well as injection timing can be worth investigating. The model applied to study the n-heptane combustion and emissions utilized a sector mesh and simulated the closed-valve events only becasue of the limited knowledge of the intake and exhaust system geometrical details. The model can be used simulate the complete cycle if these geometrical details are available. The same model can be used to simulate the dual fueling cases if kinetic mechanism and the thermo-chemical databases are available. It can also help to simulate biodiesel (RME) combustion and emissions if the kinetic mechanism and the thermo-chemical database for RME are available.

## REFERENCES


[1] R. Stone. *Introduction to Internal Combustion Engines*. The Macmillan Press Ltd, London, 1985.

[2] World population to 2300, 2004.

[3] BP statistical review of world energy. British Petroleum, June 2012. bp.com/statisticalreview.

[4] A. M. Namasivayam. *Combustion, Performance and Emissions Characteristics of Compression-Ignition Engines Fuelled by Sustainable Fuels*. PhD thesis, School of Engineering and Materials Science, Queen mary University London UK, 2011.

[5] EU emission standards for heavy duty trucks and bus engines. DieselNet, 2011. http://www.dieselnet.com/standards/eu/hd.php.

[6] T. Korakianitis, A. M. Namasivayam, and R. J. Crookes. Natural-gas fuelled spark-ignition (SI) and compression-ignition (CI) engine performance and emissions. *Progress in Energy and Combustion Science*, 37(1):89–112, Jan 2011.

[7] T. Korakianitis and D.G. Wilson. Models for predicting the performance of brayton-cycle engines. *Transactions of the ASME, Journal of Engineering for Gas Turbines and Power*, 116(2):381–388, April 1994.

[8] T. Korakianitis, J. Grantstrom, P. Wassingbo, and A. Massardo. Parametric performance of combined-cogeneration power plants with various power and efficiency enhancements. *Transactions of the ASME, Journal of Engineering for Gas Turbines and Power*, 127(1):65–72, Jan 2005.

[9] T. Korakianitis, M. Boruta, J Jerovsek, and P.L. Meitner. Performance of a single nutating disk engine in the 2 to 500 kw power range. *Applied Energy*, 86(11):2213–2221, Oct 2009.

[10] J.-B. Heywood. *Internal Combustion Engine Fundamentals*. McGraw-Hill, New York, 1988.

[11] Transport statistics great britain (TSGB). UK Department for Transport, 2009.

[12] Wark, Kenneth and Richards, Donald E., Thermodynamics, 6th Ed., McGraw-Hill, 1999.

[13] J.M. Marchetti, V.U. Miguel, and A.F. Errazu. Possible methods for biodiesel production. *Renewable and Sustainable Energy Reviews*, 11(6):1300–1311, August 2007.

[14] Md. Nurun. Nabi, Md. Mustafizur. Rahman, and M. Shamim. Akhter. Biodiesel from cotton seed oil and its effect on engine performance and exhaust emissions. *Applied Thermal Engineering*, 29(11-12):2565–2570, AUG 2009.

[15] A. Murugesan, C. Umarani, R. Subramanian, and N. Nedunchezhian. Bio-diesel as an alternative fuel for diesel engines-a review. *Renewable and Sustainable Energy Reviews*, 13(3):653–662, April 2009.

[16] Z. Liu and G. A. Karim. Knock characteristics of dual-fuel engines fuelled with hydrogen fuel. *International Journal for Hydrogen Energy*, 20(11):919–924, FEB 1995.

[17] A.K. Hossain and P.A. Davies. Plant oils as fuels for compression ignition engines: A technical review and life-cycle analysis. *Renewable Energy*, 35(11):1–13, Jan 2010.

[18] J. Sheehan, V. Camobreco, J. Duffield, M. Graboski, and H. Shapouri. An overview of biodiesel and petroleum diesel life cycles. Technical report, National Renewable Energy Laboratory Report, NREL/TP-580-24772, 1998.

[19] F. Pearce. Fuels gold: Big risks of the biofuel revolution. New Scientist online, Sep 2006.

[20] R. J. Crookes and K. D. H. Bob-Manuel. Rme or dme: A preferred alternative fuel option for future diesel engine operation. *Energy Conversion and Management*, 48(11):2971–2977, NOV 2007.

[21] Hanbey Hazar and Hseyin Aydin. Performance and emission evaluation of a ci engine fueled with preheated raw rapeseed oil (rro)diesel blends. *Applied Energy*, 87(3):786 – 790, 2010.

[22] B. F. Lin, J. H. Huang, and D. Y. Huang. Experimental study of the effects of vegetable oil methyl esters on di diesel engine performance characteristics and pollutant emissions. *Fuel*, 88(9):1779–1785, SEP 2009.

[23] A. - N. Ozsezen, M Canakci, A Turkcan, and C. D. - Y. Sayin. Performance and combustion characteristics of a di diesel engine fueled with waste palm oil and canola oil methyl esters. *Fuel*, 88(4):629–636, APR 2009.

[24] E Buyukkaya. Effects of biodiesel on a di diesel engine performance, emission and combustion characteristics. *Fuel*, 89(10):3099–3105, OCT 2010.

[25] G. Labeckas and S. Slavinskas. The effect of rapeseed oil methyl ester on direct injection diesel engine performance and exhaust emissions. *Energy Conversion and Management*, 87(13-14):3161–3169, AUG 2006.

[26] M.I. Al-Widyan, G. Tashtoush, and M. Abu-Qudais. Utilization of ethyl ester of waste vegetable oils as fuel in diesel engines. *Fuel Processing Technology*, 76(2):1628–34, May 2002.

[27] Magn Lapuerta, Jos M. Herreros, Lisbeth L. Lyons, Reyes Garca-Contreras, and Yolanda Briceo. Effect of the alcohol type used in the production of waste cooking oil biodiesel on diesel performance and emissions. *Fuel*, 87(15-16):1954–1967, NOV 2006.

[28] M. Gumus and S. Kasifoglu. Performance and emission evaluation of a compression ignition engine using a biodiesel (apricot seed kernel oil methyl ester) and its blends with diesel fuel. *Biomass Bioenergy*, 34(1):134–139, JAN 2010.

[29] A. K. Agarwal. Biofuels (alcohols and biodiesel) applications as fuels for internal combustion engines. *Progress in Energy and Combustion Science*, 33(3):233–271, June 2007.

[30] D. - H. Qi, L. - M. Geng, H. Chen, Y.-Z.-H. Bian, J. Liu, and X.-C.-H. Ren. Combustion and performance evaluation of a diesel engine fuelled with biodiesel produced from soybeen crude oil. *Renew Energ*, 34(12):2706–13, DEC 2009.

[31] H. Aydin and H. Bayinder. Performance and emission analysis of cotton seed oil methyl ester in a diesel engine. *Renewable Energ*, 34(3):1628–34, - 2010.

[32] Z. Utlu and M. S. kocak. The effect of biodiesel fuel obtained from waste frying oil on direct injection diesel engine performance and exhaust emissions. *Renewable Energ*, 33(8):1936–41, - 2008.

[33] F.K. Xue. Effect of biodiesel on engine performances and emissions. *Renewable and Sustainable Energy Reviews*, 15(2):1098–1116, 2011.

[34] H. - S. Yucesu and I. Cumali. Effect of cotton seed oil methyl ester on the performance and exhaust emission of a diesel engine. *Energ Source Part A*, 89:389–398, 2006.

[35] Md. Nurun. Nabi, S. M. Najmul Haq, and M. S. Akhter. Karanja (pongamia pinnata) biodiesel production in bangladesh, characterizatioin of karanja biodiesel and its effects on diesel emissions. *Fuel Process Technol*, 90(1):1080–1086, FEB 2009.

[36] J. Sun, J. A. Caton, , and T. J. Jacobs. Oxides of nitrogen emissions from biodiesel-fuelled diesel engines. *Progress in Energy and Combustion Science*, 36(6):677–695, DEC 2010.

[37] F. Fujia Wu, J. Wang, W. Chen, and S. Shuai. A study on emission performance of a diesel engine fueled with five typical methyl ester biodiesels. *Physics of Fluids*, 43(7):1481–1485, MAR 2009.

[38] C.Y. Lin and H.A. Lin. Engine performance and emission characteristics of a three-phase emulsion of biodiesel produced by peroxidation. *Fuel Processing Technology*, 88(1):35–41, JAN 2007.

[39] A. L. Boehman, D. Morris, J. Szybist, and E. Esen. The impact of the bulk modulus of diesel fuels on fuel injection timing. *Energy and Fuels*, 18(6):1877–182, DEC 2004.

[40] M. Lapuerta, O. Armas, , and J. Rodriguez-Fernandez. Effect of biodiesel fuels on diesel engine emissions. *Progress in Energy and Combustion Science*, 34(2):198–223, April 2008.

[41] M.E. Tat, J.H. Van Gerpen, and P.S. Wang. Fuel property effects on injection tim-

ing, ignition timing and oxides of nitrogen emissions from biodeisel fuelled engines. volume 50, pages 1123–1128, 2007.

[42] YC Leung, Y. Luo, and T. L. Chan. Experimental study of the effects of vegetable oil methyl esters on di diesel engine performance characteristics and pollutant emissions. *Energy and Fuel*, 20(1):Optimization of exhaust emission of a diesel engine fuelled with biodiesel, APR 2006.

[43] G. Fontaras, G. Karavalakis, M. Kousoulidou, T. Tzamkiozis, L. Ntziachristos, E. Bakeas, S. Stournas, and Z. Samaras. Effects of biodiesel on passenger car fuel consumption, regulated and non-regulated pollutant emissions over legislated and real-world driving cycles. *Fuel*, 88(9):1608–1617, SEP 2009.

[44] M. A. R. Nascimento, E.S. Lora, Paulo. S.P. Corra, R.V. Andrade, M.A. Rendon, O.J. Venturini, and Guido.A.S. Ramirez. Biodiesel fuel in diesel micro-turbine engines: Modelling and experimental evaluation. *Energy*, 33(2):233–240, FEB 2008.

[45] N.R. Banapurmath, P.G. Tewari, and R.S. Hosmath. Performance and emission characteristics of a di compression ignition engine operated on honge, jatropha and sesame oil methyl esters. *Int J Hydrogen Energy*, 33(15):4013–4029, AUG 2008.

[46] J. Huang, , and R. J. Crookes. Assessment of simulated biogas as a fuel for the spark ignition engine. *Fuel*, 77(15):1793, DEC 1998.

[47] H. M. Cho and B. He. Spark ignition natural gas engines-a review. *Energy Conversion and Management*, 48(2):608–618, FEB 2007.

[48] K. Zeng, Z. Huang, B. Liu, L. Liu, D. Jiang, Y. Ren, and J. J. Wang. Combustion characteristics of a direct-injection natural gas engine under various fuel injection timings. *Applied Thermal Engineering*, 26(8-9):806–813, JUN 2006.

[49] Natural gas vehicle statistics. International Association for Natural Gas Vehicles, DEC 2008.

[50] E. Porpatham, A. Ramesh, and B. Nagalingam. Investigation on the effect of concentration of methane in biogas when used as a fuel for a spark ignition engine. *Fuel*,

87(8-9):1651–1659, JUL 2008.

[51] S. O. Bade Shrestha and G. Narayanan. Landfill gas with hydrogen addition-a fuel for si engines. *Fuel*, 87(17-18):3616–3626, DEC 2008.

[52] J. M. Lopez, A. Gomez, F. Aparicio, and F. J. Sanchez. Comparison of ghg emissions from diesel, biodiesel and natural gas refuse trucks of the city of madrid. *Applied Energy*, 86(5):610–615, MAY 2009.

[53] P. Dimopoulos, C. Bach, P. Soltic, and K. Boulouchos. Hydrogen-natural gas blends fuelling passenger car engines: Combustion, emissions and well-to-wheels assessment. *International Journal of Hydrogen Energy*, 33(23):7224–7236, DEC 2008.

[54] M. Dagosto and S. K. Ribeiro. Assessing total and renewable energy in brazilian automotive fuels. a life cycle inventory (LCI) approach. *Renewable and Sustainable Energy Reviews*, 13(6-7):1326–1337, AUG-SEP 2009.

[55] T. Korakianitis, A.M. Namasivayam, R.J. Crookes, S. Imran, B. Ihracska, A. Diez, and N.A. Malik. Compression-ignition engine performance and emissions in single and dual fuelling modes with sustainable fuels. In *Power and Energy Systems and Applications*, pages 322–327, Nov 2011.

[56] A. Malynn, H. Musawi, S. Odetunde, and C. Rodrigues. Alternative automobile engine fuels for the uk market. Master's thesis, Queen Mary and Westfield College, University of London, 2006.

[57] R. J. Crookes, K. D. H. Bob-Manuel, and J. Olsen. Renewable fuelling of a diesel engine in single and dual fuel operation. In *Technische Akademie Esslingen (TAE) 6th International Colloquium fuels*, 10 -11 JAN 2007.

[58] G. A. Karim. Combustion in gas fueled compression: Ignition engines of the dual fuel type. *Journal of Engineering for Gas Turbines and Power*, 125(3):827–836, JUL 2003.

[59] J. Kusaka, T. Okamoto, Y. Daisho, R. Kihara, and T. Saito. Combustion and exhaust gas emission characteristics of a diesel engine dual- fueled with natural gas. *JSAE*

*Review*, 21(4):489–498, OCT 2000.

[60] R. G. Papagiannakis and D. T. Hountalas. Combustion and exhaust emission characteristics of a dual fuel compression ignition engine operated with pilot diesel fuel and natural gas. *Energy Conversion and Management*, 45(18-19):2971–2987, NOV 2004.

[61] A. P. Carlucci, A. Ficarella, and D. Laforgia. Control of the combustion behavior in a diesel engine using early injection and gas addition. *Applied Thermal Engineering*, 26(17-18):2279–2286, DEC 2006.

[62] B.B. Sahoo, N. Sahoo, , and U.K. Saha. Effect of engine parameters and type of gaseous fuel on the performance of dual-fuel gas diesel engines-a critical review. *Renewable and Sustainable Energy Reviews*, 13(6-7):1151–1184, AUG-SEP 2009.

[63] R. G. Papagiannakis and D. T. Hountalas. Experimental investigation concerning the effect of natural gas percentage on performance and emissions of a di dual fuel diesel engine. *Applied Thermal Engineering*, 23(3):353–365, FEB 2003.

[64] M. Y. M. Selim. Pressure-time characteristics in diesel engine fueled with natural gas. *Renewable Energy*, 22(4):473–489, APR 2001.

[65] G. A. Karim. A review of combustion processes in the dual fuel engine-the gas diesel engine. *Progress in Energy and Combustion Science*, 6(3):277–285, 1980.

[66] M. Balat. Potential importance of hydrogen as a future solution to environmental and transportation problems. *Renewable Energy*, 33(9):1982–1988, SEP 2008.

[67] J. A. Karim. Hydrogen as a spark ignition engine fuel. *J Eng Gas Turbines Power*, 28(5):569–577, - 2003.

[68] S. Verhelst and S. Wallner. Hydrogen-fueled internal combustion engines. *Progress in Energy and Combustion Science*, 35(6):490 – 527, 2009.

[69] R. Sierens, S. Verhelst, and S. Verstraeten. An overview of hydrogen fuelled internal combustion engines. In *Proceedings International Hydrogen Energy Congress and Exhibition (IHEC) Istanbul, Turkey*, 13 - 15 JULY 2005.

[70] N. Zamel and X. Li. Life cycle analysis of vehicles powered by a fuel cell and by internal combustion engine for canada. *Journal of Power Sources*, 155(2):1241–1253, NOV 2006.

[71] L. M. Das. Hydrogen engine: Research and development programmes in indian institute of technology (IIT), delhi. *International Journal of Hydrogen Energy*, 27(9):953–965, SEP 2002.

[72] J. D. Naber and D. L. Siebers. Hydrogen combustion under diesel engine conditions. *International Journal of Hydrogen Energy*, 23(5):363–371, MAY 1998.

[73] S. Szwaja and K. K. Grab-Rogalinski. Hydrogen combustion in a compression ignition diesel engine. *International Journal of Hydrogen Energy*, 34(10):4413–4421, MAY 2009.

[74] G. Gopal, P. Srinivasa Rao, K.V. Gopalakrishnan, and B. S. Murthy. Use of hydrogen in dual-fuel engines. *International Journal of Hydrogen Energy*, 7(3):267–272, 1982.

[75] P. N. Patro. Combustion study of hydrogen fueled di diesel engine: Simplified heat release analysis. *International Journal of Hydrogen Energy*, 18(3):231–241, MARCH 1993.

[76] B. Haragopala Rao, K. N. Shrivastava, and H. N. Bhakta. Hydrogen for dual fuel engine operation. *International Journal of Hydrogen Energy*, 8(5):381–384, 1983.

[77] N. Saravanan and G. Nagarajan. Performance and emission study in manifold hydrogen injection with diesel as an ignition source for different start of injection. *Renew Energy*, 34(1):328–334, JAN 2009.

[78] N. Saravanan, G. Nagarajan, K.M Kalaiselvan, and C. Dhanasekaran. An experimental investigation on hydrogen as a dual fuel for diesel engine system with exhaust gas recirculation technique. *Renew Energy*, 33(3):422–427, MARCH 2008.

[79] P. K. Bose and D. Maji. An experimental investigation on engine performance and emissions of a single cylinder diesel engine using hydrogen as inducted fuel and diesel as injected fuel with exhaust gas recirculation. *International Journal for Hydrogen*

*Energy*, 34(11):4847–4854, JUN 2009.

[80] M. Masood, M.M. Ishrat, and A. S. Reddy. Computational combustion and emission analysis of hydrogendiesel blends with experimental verification. *International Journal for Hydrogen Energy*, 32(13):2539–2547, SEP 2007.

[81] N. Saravanan, G. Nagarajan, and S. Narayanasamy. An experimental investigation on di diesel engine with hydrogen fuel. *Renew Energy*, 33:415–421, 2008.

[82] Rao. B. Hargopala, K. N. Shrivatava, and H. N. Bhakta. Hydrogen for dual fuel engine operation. *Int J Hydrogen Energy*, 8(5):381–384, NOV 1983.

[83] C. F. Taylor and E. S. Taylor. *The Internal Combustion Engine.* International Textbook Company, Scranton,Pennsylvania, 1962.

[84] A. M. Namasivayam, T. Korakianitis, R. J. Crookes, K. D. H. Bob-Manuel, and J. Olsen. Biodiesel, emulsified biodiesel and dimethyl ether as pilot fuels for natural gas fuelled engines. *Applied Energy*, 87(3):769–778, Mar 2010.

[85] P. McCarthy, M.G. Rasul, and S. Moazzem. Analysis and comparison of performance and emissions of an internal combustion engine fuelled with petroleum diesel and different bio-diesels. *Fuel*, 90(6):2147 – 2157, 2011.

[86] A. Schonborn, N. Ladommatos, J. Williams, R. Allan, and J. Rogerson. The influence of molecular structure of fatty acid monoalkyl esters on diesel combustion. *Combustion and Flame*, 156(7):1396–1412, 2009.

[87] Avinash Kumar Agarwal and K. Rajamanoharan. Experimental investigations of performance and emissions of karanja oil and its blends in a single cylinder agricultural diesel engine. *Applied Energy*, 86(1):106 – 112, 2009.

[88] T. Ganapathy, R.P. Gakkhar, and K. Murugesan. Influence of injection timing on performance, combustion and emission characteristics of jatropha biodiesel engine. *Applied Energy*, 88(12):4376 – 4386, 2011.

[89] P.K. Devan and N.V. Mahalakshmi. Study of the performance, emission and combustion characteristics of a diesel engine using poon oil-based fuels. *Fuel Processing*

*Technology*, 90(4):513 – 519, 2009.

[90] Breda Kegl. Influence of biodiesel on engine combustion and emission characteristics. *Applied Energy*, 88(5):1803–1812, 2011. Times Cited: 1.

[91] A. Tsolakis, A. Megaritis, M. L. Wyszynski, and K. Theinnoi. Engine performance and emissions of a diesel engine operating on diesel-rme (rapeseed methyl ester) blends with egr (exhaust gas recirculation). *Energy*, 32(11):2072–2080, November 2007.

[92] F. Caresana. Impact of biodiesel bulk modulus on injection pressure and injection timing. the effect of residual pressure. *Fuel*, 90(2):477–485, 2011.

[93] S Cheng, A, A Upatnieks, and J Mueller, C. Investigation of the impact of biodiesel fuelling on nox emissions using an optical direct injection diesel engine. *International Journal of Engine Research*, 7:297–318, 2006.

[94] E. Rajasekar, A. Murugesan, R. Subramanian, and N. Nedunchezhian. Review of no(x) reduction technologies in ci engines fuelled with oxygenated biomass fuels. *Renewable & Sustainable Energy Reviews*, 14:2113–2121, 2010.

[95] Magin Lapuerta, Octavio Armas, and Jose Rodriguez-Fernandez. Effect of biodiesel fuels on diesel engine emissions (vol 34, pg 198, 2008). *Progress in Energy and Combustion Science*, 35(4):383–383, 2009. Times Cited: 0.

[96] A. Tsolakis, A. Megaritis, and D. Yap. Application of exhaust gas fuel reforming in diesel and homogeneous charge compression ignition (hcci) engines fuelled with biofuels. *Energy*, 33(3):462 – 470, 2008.

[97] Jagannath Balasaheb Hirkude and Atul S. Padalkar. Performance and emission analysis of a compression ignition: Engine operated on waste fried oil methyl esters. *Applied Energy*, 90(1):68 – 72, 2012. Energy Solutions for a Sustainable World, Special Issue of International Conference of Applied Energy, ICA2010, April 21-23, 2010, Singapore.

[98] Mustafa Canakci. Combustion characteristics of a turbocharged di compression ignition engine fueled with petroleum diesel fuels and biodiesel. *Bioresource Technology*,

98(6):1167 – 1175, 2007.

[99] Colin R Ferguson and Allan T Kirkpatrick. *Internal Combustion engines, Applied thernal sciences*. John Wiley and Sons, Inc, 2001.

[100] T. Korakianitis, A. M. Namasivayam, and R. J. Crookes. Diesel and rapeseed methyl ester (RME) pilot fuels for hydrogen and natural gas dual-fuel combustion in compression-ignition engines. *Fuel*, 90(7):2384–2395, Jul 2011.

[101] S.Orhan Akansu, Zafer Dulger, Nafiz Kahraman, and T.Nejat Vezirolu. Internal combustion engines fueled by natural gashydrogen mixtures. *International Journal of Hydrogen Energy*, 29(14):1527 – 1539, 2004.

[102] Georgios Karavalakis, Thomas D. Durbin, Mark Villela, and J. Wayne Miller. Air pollutant emissions of light-duty vehicles operating on various natural gas compositions. *Journal of Natural Gas Science and Engineering*, 4(0):8 – 16, 2012.

[103] G.A Richards, M.M McMillian, R.S Gemmen, W.A Rogers, and S.R Cully. Issues for low-emission, fuel-flexible power systems. *Progress in Energy and Combustion Science*, 27(2):141 – 169, 2001.

[104] R. Chandra, V.K. Vijay, P.M.V. Subbarao, and T.K. Khura. Performance evaluation of a constant speed ic engine on CNG, methane enriched biogas and biogas. *Applied Energy*, 88(11):3969 – 3977, 2011.

[105] R.G. Papagiannakis, P.N. Kotsiopoulos, T.C. Zannis, E.A. Yfantis, D.T. Hountalas, and C.D. Rakopoulos. Theoretical study of the effects of engine parameters on performance and emissions of a pilot ignited natural gas diesel engine. *Energy*, 35(2):1129 – 1138, 2010.

[106] T. White and B. Milton. Shock wave calibration of under-expanded natural gas fuel jets. *Shock Waves*, 18:353–364, 2008.

[107] R.G. Papagiannakis, C.D. Rakopoulos, D.T. Hountalas, and D.C. Rakopoulos. Emission characteristics of high speed, dual fuel, compression ignition engine operating in a wide range of natural gas/diesel fuel proportions. *Fuel*, 89(7):1397 – 1406, 2010.

[108] G. P. McTaggart-Cowan, S. N. Rogak, S. R. Munshi, P. G. Hill, and W. K. Bushe. Combustion in a heavy-duty direct-injection engine using hydrogen-methane blend fuels. *International Journal of Engine Research*, 10(1):1–13, February 2009.

[109] J. Stewart, A. Clarke, and R. Chen. An experimental study of the dual-fuel performance of a small compression ignition diesel engine operating with three gaseous fuels rid a-2785-2010. *Proceedings of the Institution of Mechanical Engineers Part D-journal of Automobile Engineering*, 221(D8):943–956, August 2007.

[110] Paul Hellier, Nicos Ladommatos, Robert Allan, and John Rogerson. The influence of fatty acid ester alcohol moiety molecular structure on diesel combustion and emissions. *Energy & Fuels*, 26(3):1912–1927, 2012.

[111] Seung Hyun Yoon and Chang Sik Lee. Experimental investigation on the combustion and exhaust emission characteristics of biogasbiodiesel dual-fuel combustion in a ci engine. *Fuel Processing Technology*, 92(5):992 – 1000, 2011.

[112] C.D. Rakopoulos and C.N. Michos. Generation of combustion irreversibilities in a spark ignition engine under biogas hydrogen mixtures fueling. *International Journal of Hydrogen Energy*, 34(10):4422 – 4437, 2009.

[113] Jim Ohi. Hydrogen energy cycle: An overview. *National Renewable Energy Laboratory, Golden, Colorado 80401*, -(80401):Colorado, Golden, 2005.

[114] T. Korakianitis, A. M. Namasivayam, and R. J. Crookes. Hydrogen dual-fuelling of compression ignition engines with emulsified biodiesel as pilot fuel. *International Journal of Hydrogen Energy*, 35(24):13329–13344, Dec 2010.

[115] Murari Mohon Roy, Eiji Tomita, Nobuyuki Kawahara, Yuji Harada, and Atsushi Sakane. An experimental investigation on engine performance and emissions of a supercharged h2-diesel dual-fuel engine. *International Journal of Hydrogen Energy*, 35(2):844 – 853, 2010.

[116] V. Edwin Geo, G. Nagarajan, and B. Nagalingam. Studies on dual fuel operation of rubber seed oil and its bio-diesel with hydrogen as the inducted fuel. *International*

*Journal of Hydrogen Energy*, 33(21):6357 – 6367, 2008.

[117] C. Liew, H. Li, J. Nuszkowski, S. Liu, T. Gatts, R. Atkinson, and N. Clark. An experimental investigation of the combustion process of a heavy-duty diesel engine enriched with h2. *International Journal of Hydrogen Energy*, 35(20):11357 – 11365, 2010.

[118] Murari Mohon Roy, Eiji Tomita, Nobuyuki Kawahara, Yuji Harada, and Atsushi Sakane. Performance and emission comparison of a supercharged dual-fuel engine fueled by producer gases with varying hydrogen content. *International Journal of Hydrogen Energy*, 34(18):7811 – 7822, 2009.

[119] A. Tsolakis and A. Megaritis. Catalytic exhaust gas fuel reforming for diesel engines: effects of water addition on hydrogen production and fuel conversion efficiency. *International Journal of Hydrogen Energy*, 29(13):1409 – 1419, 2004.

[120] T. Gatts, H. Li, C. Liew, S. Liu, T. Spencer, S. Wayne, and N. Clark. An experimental investigation of h2 emissions of a 2004 heavy-duty diesel engine supplemented with h2. *International Journal of Hydrogen Energy*, 35(20):11349 – 11356, 2010.

[121] P.G. Aleiferis and M.F. Rosati. Flame chemiluminescence and oh lif imaging in a hydrogen-fuelled spark-ignition engine. *International Journal of Hydrogen Energy*, 37(2):1797 – 1812, 2012. 10th International Conference on Clean Energy 2010.

[122] A. Tsolakis and A. Megaritis. Partially premixed charge compression ignition engine with on-board production by exhaust gas fuel reforming of diesel and biodiesel. *International Journal of Hydrogen Energy*, 30(7):731 – 745, 2005.

[123] D. Yap, S.M. Peucheret, A. Megaritis, M.L. Wyszynski, and H. Xu. Natural gas hcci engine operation with exhaust gas fuel reforming. *International Journal of Hydrogen Energy*, 31(5):587 – 595, 2006.

[124] Changwei Ji, Shuofeng Wang, and Bo Zhang. Combustion and emissions characteristics of a hybrid hydrogen gasoline engine under various loads and lean conditions. *International Journal of Hydrogen Energy*, 35(11):5714 – 5722, 2010. 3rd Argentinean

and 2nd Latin American Congress in Hydrogen and Sustainable Energy Sources, 3rd Argentinean and 2nd Latin American Congress in Hydrogen and Sustainable Energy Sources.

[125] Gregory K. Lilik, Hedan Zhang, Jos Martin Herreros, Daniel C. Haworth, and Andr L. Boehman. Hydrogen assisted diesel combustion. *International Journal of Hydrogen Energy*, 35(9):4382 – 4398, 2010.

[126] Fluent Inc., New hamshire,USA. *Fluent 12.0 User guide*, 2006.

[127] S.B. Pope. Pdf methods for turbulent reactive flows. *Progress Energy Combustion Science,*, 11:119–192, 1985.

[128] R.S. Dyer and T. Korakianitis. Pre-integrated response map for inviscid propane-air detonation. *Combustion Science and Technology*, 179(7):1327–1347, July 2007.

[129] R. Korakianitis, T. Dyer and N. Subramanian. Pre-integrated non-equilibrium combustion-response mapping for gas-turbine emissions. *Transactions of the ASME, Journal of Engineering for Gas Turbines and Power*, 126(2):300–305, April 2004.

[130] Nguyen Thai Chung. *Pre-Integrated Non-Equilibrium Combustion Response Mapping for Internal Combustion Engines.* PhD thesis, Department of Mechanical Engineering, University of Glasgow, 2005.

# CHAPTER 9

# APPENDICES

## 9.1 APPENDIX A - PRESSURE AND RATE OF ENERGY RELEASE DATA FOR CHAPTERS 3,4 AND 5

This section pressure and rate of energy release data to support the claims made in chapters 3,4 and 5. Figures 9.1(a) and 9.1(b) represents in-cylinder pressure and rate of

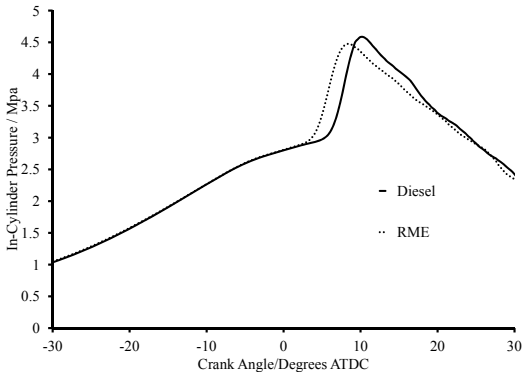


(a) Cylinder pressure for pure diesel and RME at a BMEP of 0.125 MPa and 1000 rev/min

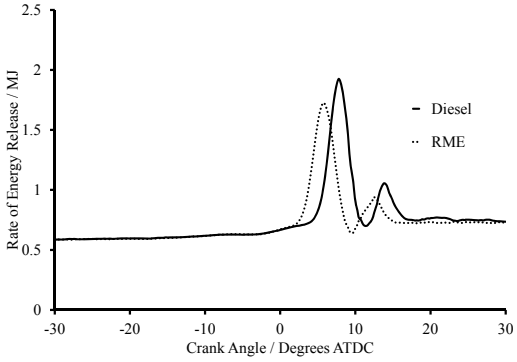


(b) Rate of energy release for pure diesel and RME at a BMEP of 0.125 MPa and 1000 rev/min

Figure 9.1. Experimentally obtained in-cylinder pressure (a) and rate of energy release (b) for for diesel and RME at a BMEP of 0.125 MPa and 1000 rev/min

energy release for diesel and RME fuelling at a BMEP of 0.125 MPa while operating at 1000 rev/min. Whereas Figures 9.2(a) and 9.2(b) represents in-cylinder pressure and rate of energy release for diesel and RME fuelling at a BMEP of 0.503 MPa while operating at 1000 rev/min. While operating at lower load, higher peak in-cylinder pressure has been observed when compared to RME. Shorter ignition in case of RME has caused the peak pressure to occur slightly earlier. When the rate of energy release curves for the two fuels were compared, diesel has shown clearly higher rate of energy release peaks. Both peaks for the rate of energy release were lower and occur earlier when compared to the ones obtained

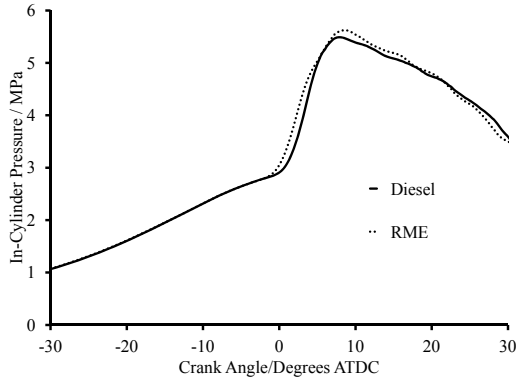


(a) Cylinder pressure for pure diesel and RME at a BMEP of 0.503 MPa and 1000 rev/min

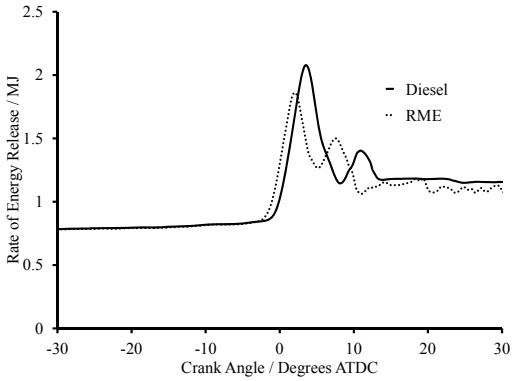


(b) Rate of energy release for pure diesel and RME at a BMEP of 0.503 MPa and 1000 rev/min

Figure 9.2. Experimentally obtained in-cylinder pressure (a) and rate of energy release (b) for for diesel and RME at a BMEP of 0.503 MPa and 1000 rev/min

with diesel. At higher loads, the two fuels have shown similar peak pressures with diesel producing slightly higher peak pressure but the difference in peak pressures for the two fuels is reduced when compared to the lower load case. Similar to the lower load case, the first rate of energy release peak diesel is significantly higher but the second peak for RME is higher when compared to the second peak obtained with diesel at the higher load. Figures 9.3(a) and 9.3(b) show in-cylinder pressure and rate of energy release for pure diesel and diesel piloted natural gas at 0.38 MPa with diesel pilot set at 0.125 MPa for the dual fuelling case 1000 rev/min. Whereas Figures 9.4(a)and 9.4(b) in-cylinder pressure and rate of energy release for pure diesel and diesel piloted natural gas at 0.503 MPa with diesel pilot set at 0.125 MPa for the dual fuelling case 1000 rev/min. At a relatively lower load (0.38 MPa), diesel piloted natural gas has produced lower peak pressure when compared to the pure diesel based single fueling whereas similar peak pressures are observed when the two cases are compared at a higher BMEP (0.503 MPa). The rate of energy release peaks for the dual fueling case are comparable to the ones obtained with diesel based single fueling but these occur slightly later in the cycle. Figures 9.5(a)and 9.5(b) in-cylinder pressure and

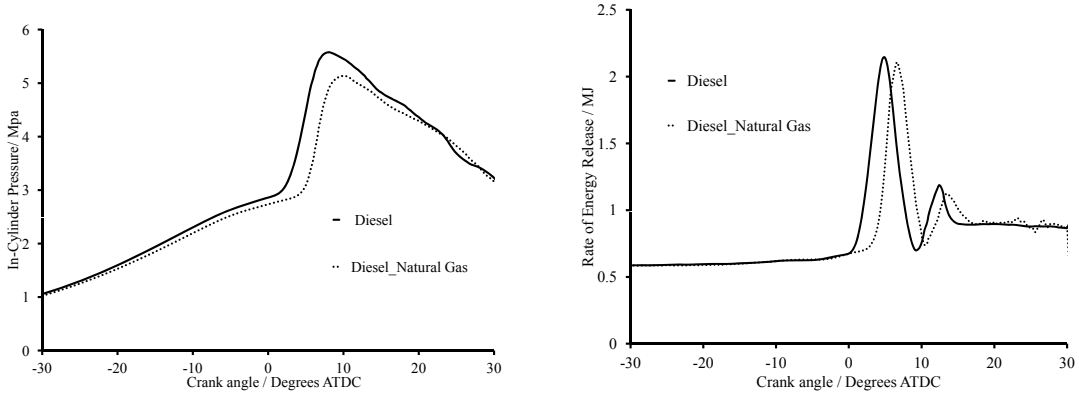


(a) Cylinder pressure for pure diesel and diesel piloted natural at a BMEP of 0.38 MPa and 1000 rev/min

(b) Rate of energy release for pure diesel and diesel piloted natural gas at a BMEP of 0.38 MPa and 1000 rev/min

Figure 9.3. Experimentally obtained in-cylinder pressure (a) and rate of energy release (b) for pure diesel and diesel piloted natural gas at 0.38 MPa with diesel pilot set at 0.125 MPa for the dual fuelling case 1000 rev/min

rate of energy release for pure RME and RME piloted natural gas at 0.503 MPa with diesel pilot set at 0.125 MPa for the dual fueling case 1000 rev/min. RME based dual fueling of natural gas has exhibited similar peak pressure but clearly higher first rate of energy release peak when compared to the RME based single fueling. Figures 9.6(a)and 9.6(b) in-cylinder pressure and rate of energy release for pure diesel and diesel piloted hydrogen at 0.503 MPa with diesel pilot set at 0.315 MPa for the dual fueling case 1000 rev/min. Figures 9.7(a)and 9.7(b) in-cylinder pressure and rate of energy release for pure RME and RME piloted hydrogen at 0.503 MPa with RME pilot set at 0.315 MPa for the dual fueling case 1000 rev/min. When hydrogen is piloted by either diesel RME, it produces higher peak cylinder pressure when compared to the single fueling cases based on the respective pilot fuels. Also, the rate of energy release peak are higher in case of hydrogen based dual fueling when compared to the respective fueling cases.

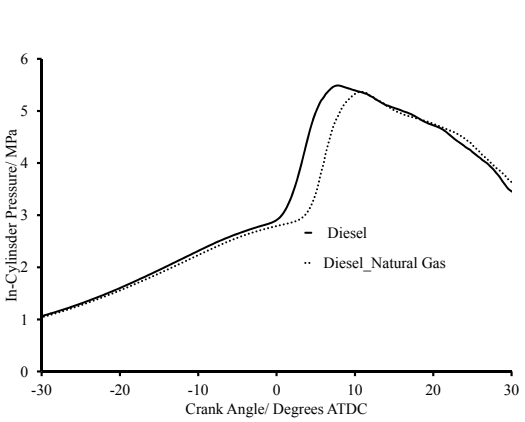


(a) Cylinder pressure for pure diesel and diesel piloted natural at a BMEP of 0.503 MPa and 1000 rev/min

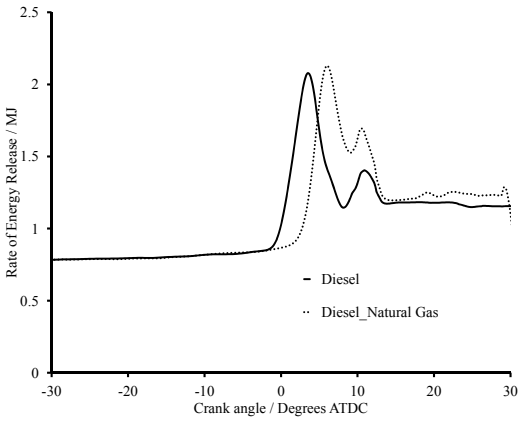


(b) Rate of energy release for pure diesel and diesel piloted natural gas at a BMEP of 0.503 MPa and 1000 rev/min

Figure 9.4. Experimentally obtained in-cylinder pressure (a) and rate of energy release (b) for pure diesel and diesel piloted natural gas at 0.503 MPa with diesel pilot set at 0.125 MPa for the dual fuelling case 1000 rev/min

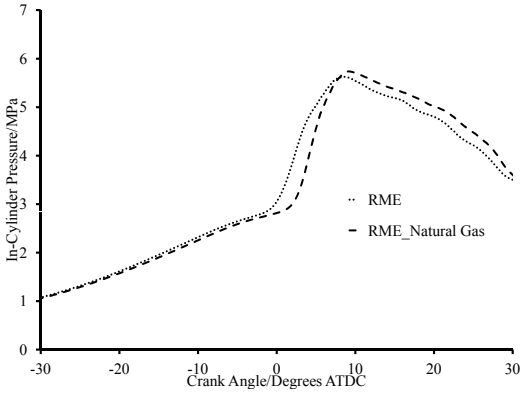


(a) Cylinder pressure for pure RME and RME piloted natural at a BMEP of 0.503 MPa and 1000 rev/min

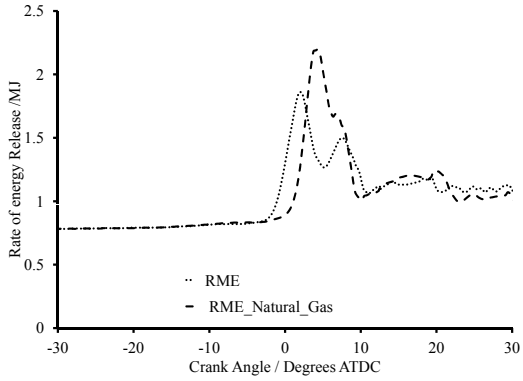


(b) Rate of energy release for pure RME and RME piloted natural at a BMEP of 0.503 MPa and 1000 rev/min

Figure 9.5. Experimentally obtained in-cylinder pressure (a) and rate of energy release (b) for pure RME and RME piloted natural gas at 0.503 MPa with diesel pilot set at 0.125 MPa for the dual fuelling case 1000 rev/min

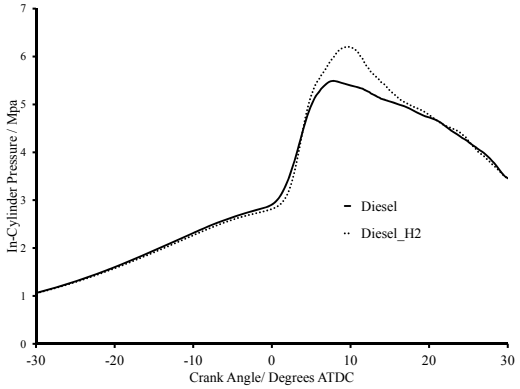


(a) Cylinder pressure for pure diesel and diesel piloted hydrogen at a BMEP of 0.503 MPa and 1000 rev/min

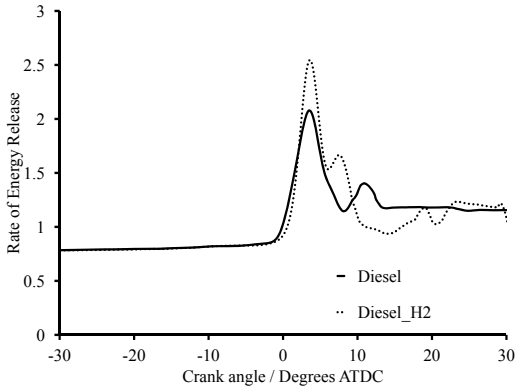


(b) Rate of energy release for pure diesel and diesel piloted hydrogen at a BMEP of 0.503 MPa and 1000 rev/min

Figure 9.6. Experimentally obtained in-cylinder pressure (a) and rate of energy release (b) for pure diesel and diesel piloted hydrogen at 0.503 MPa with diesel pilot set at 0.315 MPa for the dual fuelling case 1000 rev/min

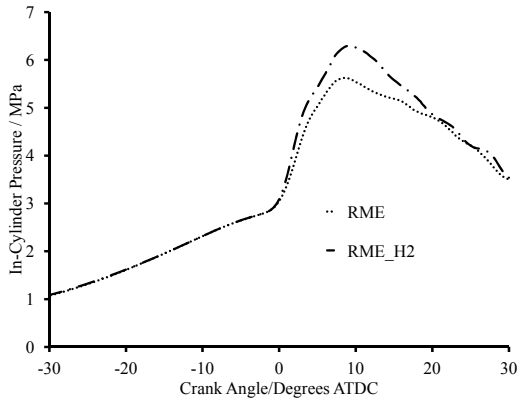


(a) Cylinder pressure for pure RME and RME piloted hydrogen at a BMEP of 0.503 MPa and 1000 rev/min

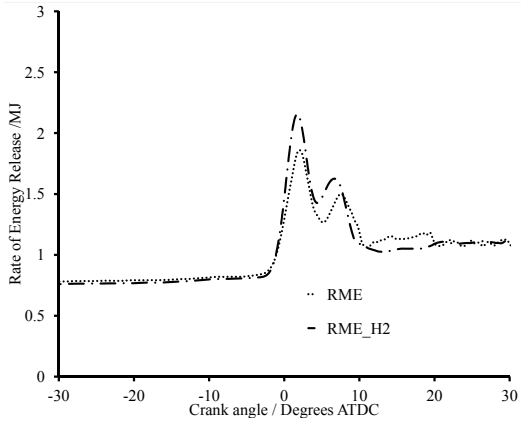


(b) Rate of energy release for pure RME and RME piloted hydrogen at a BMEP of 0.503 MPa and 1000 rev/min

Figure 9.7. Experimentally obtained in-cylinder pressure (a) and rate of energy release (b) for pure RME and RME piloted hydrogen at 0.503 MPa with diesel pilot set at 0.315 MPa for the dual fuelling case 1000 rev/min

## 9.2 APPENDIX B - SAMPLE CALCULATION

This section shows a list of all experimental parameters and a sample of complete calculation.

The sample calculations were done for diesel fuel when the test rig was run at 1000 rev/min. All sample calculations throughout this appendix are shown using this operating condition.

Brake power ($\dot{W}_b$)/W:

$$W_b = \frac{LN}{0.447} = 7315.436 \tag{9.1}$$

where L is the dynamometer load (196.2 N), N is engine speed (16.667 r/s), and 0.447 $m^{-1}$ is equal to $1/2\pi$x, where x is the length of the Gardner dynamometer torque arm (0.356 m).

Brake mean effective pressure (BMEP) / MPa

$$W_b = \frac{\dot{W}_b n_1}{V_s N \sigma} = 0.63 \tag{9.2}$$

where $n_1$ is the number of revolutions per cycle (2), $V_s$ is the swept volume of the cylinder (0.00139 $m^3$) and $\sigma$ is the number of cylinders (1).

Mass flow rate of fuel ($\dot{m}_f$)/kg/s

$$\dot{m}_f = \frac{m_f}{t} \tag{9.3}$$

where $m_f$ is mass of the fuel sprayed into the combustion chamber in t seconds. For dual-fueling cases, the $m_f$ term in equation 9.3 becomes the sum of two flow raes: the pilot fuel mass flow rate ($m_{pf}$) and the gaseous fuel mass flow rate ($m_{gf}$). The gaseous fuel mass flow rates were converted from volume flow rates read from their respective volume flow meters.

Mass flow rate of intake air ($\dot{m}_a$) / kg/s

$$\dot{m}_a = C_d A \sqrt{2\rho_a \Delta P} = 0.0105 \tag{9.4}$$

where $C_d$ is the coefficient of discharge (0.65), A is the area of the orifice (0.000642 $m^2$) and $\Delta$P and $\rho_a$ are the pressure difference across (309.015 Pa) and the density of air (1.209 $kg/m^3$) respectively.

Volumetric efficiency

$$\eta_v = \frac{\dot{m}_a n}{V_s \rho_a N} = 0.75 \tag{9.5}$$

Specific fuel consumption/ kg/MJ

$$SFC = \frac{\dot{m}_f}{\dot{W}_b} = 0.0696 \tag{9.6}$$

Thermal efficiency:

$$\eta_{th} = \frac{\dot{W}}{\dot{m}_f LHV_f} = 0.33 \tag{9.7}$$

The lower heating value of the diesel fuel was taken as 42.5 MJ/kg.

Equivalence ratio ($\phi$):

$$\phi = \frac{F/A}{(F/A)_{st}} \tag{9.8}$$

The mass flow rates of fuel ($\dot{m}_f$) and air ($\dot{m}_a$) are used to calculate the actual fuel to air ratio (F/A) whereas the stoichiometric fuel to air ratio ($(F/A)_{st}$) is calculated from the stoichiometric combustion equation.

Pilot fuel enthalpy fraction (PEF):

$$PEF = \frac{\dot{m}_{pf} LHV_{pf}}{\dot{m}_{pf} LHV_{pf} + \dot{m}_{gf} LHV_{gf}} = 1 \tag{9.9}$$

For dual fueling cases, the enthalpy fraction of the gaseous fuel can be calculated by subtracting the enthalpy fraction of the pilot fuel from 1.

Specific emission readings show the mass of a particular exhaust gas species that is emitted during the production of 1 MJ of brake engine energy. The mass flow rate of each individual measured exhaust gas species is found using combustion chemical equations as well as a mass balance drawn between the total mass flow of reactants into the engine

and the mass flow rate of combustion products in the exhaust gas. The process of specific emissions calculations (g/MJ) is lengthy and custom made Excel sheets showing these calculations in detail are available for reference. A sample calculation detailing how to obtain specific oxygen levels from the Gardner engine during normal CI engine operation at 1000 r/min and 0.63 MPa BMEP is shown here as an example. At first the term $\beta$ is calculated so that it can be used in the relevant combustion equation.

$$\beta = \frac{\dot{n}_a^*}{\dot{n}_a} = 1.43 \tag{9.10}$$

where $\dot{n}_a^*$ and $\dot{n}_a$ are measured and computed air flow rates respectively. The net step is to calculate the mole fraction of water ($\mathrm{MF}_{H_2O}$) in the exhaust gas products. This is done by dividing the moles of water in the exhaust by the total number of moles of the exhaust products.

$$MF_{H_2O} = \frac{0.5y}{x + 0.5y + 3.76\beta(x + 0.25y - 0.5z) + (\beta - 1)(x + 0.25y - 0.5z)} = 0.0883$$

The mole fraction of all of the exhaust species are computed in the similar manner. For example, the mole fraction of $O_2$ can be calculated as follows

$$MF_{O_2} = \frac{(\beta - 1)(x + 0.25y - 0.5z}{x + 0.5y + 3.76\beta(x + 0.25y - 0.5z) + (\beta - 1)(x + 0.25y - 0.5z)} = 0.0604$$

The computed mole fraction of the non water products can be found by subtracting the mole fraction of water products from unity.

$$MF_{non-H_2O} = 1 - MF_{H_2O} = 0.912 \tag{9.11}$$

The molecular weight of a certain species in the exhaust can be found by multiplying the mole fraction of that species by its molecular weight. For $O_2$,

$$MW_{O_2} = MF_{O_2} * 32 = 1.933 \tag{9.12}$$

The same pattern is used to calculate the molecular weight of all other species.

$$MW_{total} = MW_{O_2} + MW_{N_2} + MW_{H_2O} + MW_{CO_2} = 28.908 \tag{9.13}$$

The total mass flow rate of all reactants ($\dot{m}_{total}$) is required to obtain the computed molar flow rate of all the exhaust gas products. This is derived by holding a mass balance between the reactants and exhaust products:

$$\dot{m}_{total} = \dot{m}_f + \dot{m}_a = 0.0111 \ kg/s \tag{9.14}$$

Following equation can be used to calculate the molar flow rate ($\dot{n}_{total}$)

$$\dot{n}_{total} = \frac{\dot{m}_{total}}{MW_{total}} = 0.000382 \ kmol/s \tag{9.15}$$

The molar flow rate of water in the exhaust products is then calculated through the following equation

$$\dot{n}_{H_2O} = (\dot{n}_{total})(MF_{H_2O}) = 0.000037 \ kmol/s \tag{9.16}$$

The result of this equation can be used to calculate the mass flow rate of water in the exhaust products

$$\dot{m}_{H_2O} = (\dot{n}_{H_2O})(18) = 0.000607 \ kg/s \tag{9.17}$$

The mass flow rate of the non water products in the exhaust can be calculated as follows

$$\dot{m}_{non-H_2O} = \dot{m_{total}} - \dot{m}_{H_2O} = 0.0104 \ kg/s \tag{9.18}$$

The mass flow rate of the non water products in the exhaust as calculated above can be used obtain a molar flow rate of the dry measured exhaust gas species. In experimental measurements, $O_2$, $CO_2$ and CO are measured dry whereas $NO_X$ and HC are measured wet. The measured volumetric concentration of the exhaust gas species (either %ge or ppm) are converted to their mole fraction. At the condition under consideration, the measured %ge of $O_2$ was 7.445%. It can be converted into the mole fraction of $O_2$ as follows

$$MF^*_{O_2} = (\frac{7.445}{100})(MF_{non-H_2O}) = 0.0679 \tag{9.19}$$

The total measured mole fraction can be calculated by adding the mole fraction of all the species

$$MF^*total = MF^*_{O_2} + MF^*CO + MF^*_{CO_2} + MF^*_{NO_X} + MF^*_{HC} = 0.157 \tag{9.20}$$

Measured mole fraction of nitrogen in the exhaust is required to the total molecular weight of the measured products. Assuming that $N_2$ is the only remaining species in the exhaust, the mole fraction $N_2$ can be calculated as

$$MF^*_{N_2} = 1 - MF^*total = 0.843 \tag{9.21}$$

The measured mole fraction of each species can be used to obtain the respective molecular weight. For example, the molecular weight of $O_2$ can be calculated as

$$MW^*_{O_2} = (MF^*_{O_2})(32) = 2.172 \tag{9.22}$$

The total molecular weight of the exhaust product can be calculated as follows

$$MW^*_{total} = MW^*_{O_2} + MW^*_{CO} + MW^*_{CO_2} + MW^*_{NO_X} + MW^*HC + MW^*_{N_2} = 29.676$$

The mass flow rate of the non water products in the exhasut products and the total molecular weight of the exhaust products can be used to calculate the molar flow rate of the non water products in the exhaust.

$$\dot{n}_{non-H_2O} = \frac{\dot{m}_{non-H_2O}}{MW^*_{total}} = 0.000352 \ kmol/s \tag{9.23}$$

For the measured molar flow rate of oxygen ($\dot{n}^*_{O_2}$), following equation is used be

$$\dot{n}^*_{O_2} = (\dot{n}_{non-H_2O})(MF^*_{O_2}) = 0.0000239 \ kmol/s \tag{9.24}$$

The measured mass flow rate of oxygen ($\dot{m}^*_{O_2}$) can be

$$\dot{m}^*_{O_2} = (\dot{n}^*_{O_2})(32) = 0.000764 \ kg/s \tag{9.25}$$

The measured mass flow rate of oxygen $\dot{m}^*_{O_2}$ is divided by the brake power $\dot{W}_b$ to obtain the specific emissions of $O_2$.

$$Specific \ O_2 = \frac{\dot{m}^*_{O_2}}{\dot{W}_b} = 104.455 \ g/MJ \tag{9.26}$$

## 9.3 APPENDIX C - QUANTIFICATION OF ERROR IN MEASURING EQUIPMENT

Table 9.1 shows the stated accuracies of all measuring instruments used. Table 9.2 presents errors present in specific emissions (in g/MJ) resulting from instrument accuracies

| Instrument | Measurement Range | Accuracy |
|---|---|---|
| Digital stop watch | - | +/- 0.1 s % |
| Inclined Manometer | 0-100 mm of Hg | +/- 0.50 % |
| $NO_X$ Analyzer | 0 - 4000 ppm | +/- 1.00% |
| HC Analyzer | 0-10000 | +/- 1.00 % |
| $O_2$ Analyzer | 0-100% | +/- 1.00% |
| CO, $CO_2$ | 0-10% | +/- 1.00 % |
| Water Break | 0-25 kg | +/- 0.40 % |
| Tachometer | 0-2500 r/min | +/- ¡ 1.00 |
| Natural gas flowmeter | 0-100 litre/min | +/- 1.25% |
| Hydrogen gas flowmeter | 0-44 litre/min | +/- 1.25% |
| Piezoelectric transducer | 0-20 MPa | +/- 1.00% |
| Charge amplifier | - | +/- 1.00% |
| Type K thermocouples | -40 to $1200^0$C | +/- $2.50^0$C |

Table 9.1. Quantification of error in measuring equipment

## 9.4 APPENDIX D - PUBLICATIONS

- T. Korakianitis, A. M. Namasivayam, R. J. Crookes, S.Imran, B. Ihracska, A.Diez and N. A. Malik. Compression-ignition engine performance and emissions in single and dual fuelling modes with sustainable fuels. *Power and Energy Systems and Applications,* Nov 2011, pp.322-327. DOI:10.2316/P.2011.714-130.

| Instrument | Specific $NO_X$ | Specific HC | Specific CO | Specific $CO_2$ |
|---|---|---|---|---|
| Stopwatch | +/- 0.001 | +/- 0.000 | +/- 0.001 | +/- 0.141 |
| Manometer | +/- 0.015 | +/- 0.001 | +/- 0.007 | +/- 1.606 |
| NOx analyser | +/- 0.124 | +/- 0.000 | +/- 0.000 | +/- 0.000 |
| HC analyser | +/- 0.000 | +/- 0.169 | +/- 0.000 | +/- 0.000 |
| CO analyser | +/- 0.000 | +/- 0.000 | +/- 2.086 | +/- 0.000 |
| CO2 analyser | +/- 0.000 | +/- 0.000 | +/- 0.000 | +/- 3.621 |
| Water-brake | +/- 0.002 | +/- 0.001 | +/- 0.009 | +/- 1.844 |
| Tachometer | +/- 0.082 | +/- 0.007 | +/- 0.034 | +/- 7.381 |
| Total error | +/- 0.224 | +/- 0.178 | +/- 2.137 | +/- 14.593 |

Table 9.2. Errors present in specific emissions (in g/MJ) resulting from instrument accuracies

- Theodosios Korakianitis, N Chung, S. Imran, D. R Emberson, B. Ihracska, R. J. Crookes and A. Diez. Combustion-response Mapping Procedure for Internal-Combustion Engine Emissions. *Applied Energy,* Manuscript (under revision) No. APEN-D-12-00844.

- S. Imran, D.R. Emberson, D. Wen, A. Diez, R.J Crookes and T. Korakianitis. Performance and specific emissions contours of diesel and RME fueled compression-ignition engine, *Applied Energy,* Manuscript (under revision) No. APEN-D-12-01821.

- S. Imran, D.R. Emberson, A. Diez, D. Wen, R.J Crookes and T. Korakianitis. Natural gas fueled compression ignition engine performance and emissions maps with diesel and RME pilot fuels, *Applied Energy,* Manuscript (under review) No. APEN-D-13-00451.

- T. Korakianitis, S. Imran, D.R. Emberson, A.M.Namasivayam, B. Ihracska, D. Wen and R.J Crookes. Natural gas fueled compression ignition engine performance and

emissions maps with diesel and RME pilot fuels, *International Journal of Hydrogen Energy,* Manuscript (under review) No. HE-D-13-00486.

- S. Imran, D.R. Emberson, A.M.Namasivayam, D. Wen, R.J Crookes and T. Korakianitis. Effect of pilot fuel quantity and type on performance and emissions from natural gas and hydrogen based combustion in a compression ignition engine, *International Journal of Hydrogen Energy,* Manuscript (under review) No. HE-D-13-00490.

- S. Imran, D.R. Emberson, D. Wen, A. Diez, R.J Crookes and T. Korakianitis. Computational prediction of in-cylinder pressure, rate of energy release and engine emissions. To be submitted to *Fuel*

### 9.4.1 Planned Publications

The following is a list of future publications

- S. Imran, D.R. Emberson, D. Wen, A. Diez, R.J Crookes and T. Korakianitis. Use of hydrogen as an assistant fuel to improve natural gas performance in a compression ignition engine.

- S. Imran, D.R. Emberson, D. Wen, A. Diez, R.J Crookes and T. Korakianitis. Computational prediction of performance and emission characteristics of diesel piloted hydrogen dual fueling .

- S. Imran, D.R. Emberson, D. Wen, A. Diez, R.J Crookes and T. Korakianitis. Computational prediction of performance and emission characteristics of diesel piloted natural gas dual fueling .

- S. Imran, D.R. Emberson, D. Wen, A. Diez, R.J Crookes and T. Korakianitis. Evaluation of two different numerical schemes to integrate chemistry into turbulent engine flows.